

APPLIED COMPUTATIONAL ELECTROMAGNETICS SOCIETY JOURNAL

August 2023
Vol. 38 No. 8
ISSN 1054-4887

The ACES Journal is abstracted in INSPEC, in Engineering Index, DTIC, Science Citation Index Expanded, the Research Alert, and to Current Contents/Engineering, Computing & Technology.

The illustrations on the front cover have been obtained from the ARC research group at the Department of Electrical Engineering, Colorado School of Mines

Published, sold and distributed by: River Publishers, Alsbjergvej 10, 9260 Gistrup, Denmark

THE APPLIED COMPUTATIONAL ELECTROMAGNETICS SOCIETY

<http://aces-society.org>

EDITORS-IN-CHIEF

Atef Elsherbeni
Colorado School of Mines, EE Dept.
Golden, CO 80401, USA

Sami Barmada
University of Pisa, ESE Dept.
56122 Pisa, Italy

ASSOCIATE EDITORS

Maokun Li
Tsinghua University
Beijing 100084, China

Wei-Chung Weng
National Chi Nan University, EE Dept.
Puli, Nantou 54561, Taiwan

Paolo Mezzanotte
University of Perugia
I-06125 Perugia, Italy

Mauro Parise
University Campus Bio-Medico of Rome
00128 Rome, Italy

Alessandro Formisano
Seconda Università di Napoli
81031 CE, Italy

Luca Di Rienzo
Politecnico di Milano
20133 Milano, Italy

Yingsong Li
Harbin Engineering University
Harbin 150001, China

Piotr Gas
AGH University of Science and Technology
30-059 Krakow, Poland

Lei Zhao
Jiangsu Normal University
Jiangsu 221116, China

Riyadh Mansoor
Al-Muthanna University
Samawa, Al-Muthanna, Iraq

Long Li
Xidian University
Shaanxi, 710071, China

Sima Noghianian
Commscope
Sunnyvale, CA 94089, USA

Lijun Jiang
University of Hong Kong, EEE Dept.
Hong Kong

Steve J. Weiss
US Army Research Laboratory
Adelphi Laboratory Center (RDRL-SER-M)
Adelphi, MD 20783, USA

Nunzia Fontana
University of Pisa
56122 Pisa, Italy

Shinishihiro Ohnuki
Nihon University
Tokyo, Japan

Jiming Song
Iowa State University, ECE Dept.
Ames, IA 50011, USA

Stefano Selleri
DINFO - University of Florence
50139 Florence, Italy

Kubilay Sertel
The Ohio State University
Columbus, OH 43210, USA

Toni Bjorninen
Tampere University
Tampere, 33100, Finland

Yu Mao Wu
Fudan University
Shanghai 200433, China

Giulio Antonini
University of L'Aquila
67040 L'Aquila, Italy

Santanu Kumar Behera
National Institute of Technology
Rourkela-769008, India

Fatih Kaburcuk
Sivas Cumhuriyet University
Sivas 58140, Turkey

Antonio Musolino
University of Pisa
56126 Pisa, Italy

Daniele Romano
University of L'Aquila
67100 L'Aquila, Italy

Huseyin Savci
Istanbul Medipol University
34810 Beykoz, Istanbul

Abdul A. Arkadan
Colorado School of Mines, EE Dept.
Golden, CO 80401, USA

Alireza Baghai-Wadji
University of Cape Town
Cape Town, 7701, South Africa

Zhixiang Huang
Anhui University
China

Salvatore Campione
Sandia National Laboratories
Albuquerque, NM 87185, USA

Marco Arjona López
La Laguna Institute of Technology
Torreon, Coahuila 27266, Mexico

Amin Kargar Behbahani
Florida International University
Miami, FL 33174, USA

Ibrahim Mahariq
American University of the Middle East
Kuwait and University of
Turkish Aeronautical Association
Turkey

Kaikai Xu
University of Electronic Science
and Technology of China
China

Laila Marzall
University of Colorado, Boulder
Boulder, CO 80309, USA

EDITORIAL ASSISTANTS

Matthew J. Inman
University of Mississippi, EE Dept.
University, MS 38677, USA

Shanell Lopez
Colorado School of Mines, EE Dept.
Golden, CO 80401, USA

EMERITUS EDITORS-IN-CHIEF

Duncan C. Baker
EE Dept. U. of Pretoria
0002 Pretoria, South Africa

Allen Glisson
University of Mississippi, EE Dept.
University, MS 38677, USA

Ahmed Kishk
Concordia University, ECS Dept.
Montreal, QC H3G 1M8, Canada

Robert M. Bevensee
Box 812
Alamo, CA 94507-0516

Ozlem Kilic
Catholic University of America
Washington, DC 20064, USA

David E. Stein
USAF Scientific Advisory Board
Washington, DC 20330, USA

EMERITUS ASSOCIATE EDITORS

Yasushi Kanai
Niigata Inst. of Technology
Kashiwazaki, Japan

Mohamed Abouzahra
MIT Lincoln Laboratory
Lexington, MA, USA

Alexander Yakovlev
University of Mississippi, EE Dept.
University, MS 38677, USA

Levent Gurel
Bilkent University
Ankara, Turkey

Sami Barmada
University of Pisa, ESE Dept.
56122 Pisa, Italy

Ozlem Kilic
Catholic University of America
Washington, DC 20064, USA

Erdem Topsakal
Mississippi State University, EE Dept.
Mississippi State, MS 39762, USA

Alistair Duffy
De Montfort University
Leicester, UK

Fan Yang
Tsinghua University, EE Dept.
Beijing 100084, China

Rocco Rizzo
University of Pisa
56123 Pisa, Italy

Atif Shamim
King Abdullah University of Science and
Technology (KAUST)
Thuwal 23955, Saudi Arabia

William O'Keefe Coburn
US Army Research Laboratory
Adelphi, MD 20783, USA

Mohammed Hadi
Kuwait University, EE Dept.
Safat, Kuwait

Amedeo Capozzoli
Univerita di Naoli Federico II, DIETI
I-80125 Napoli, Italy

Wenxing Li
Harbin Engineering University
Harbin 150001, China

Qiang Ren
Beihang University
Beijing 100191, China

EMERITUS EDITORIAL ASSISTANTS

Khaleb ElMaghoub
Trimble Navigation/MIT
Boston, MA 02125, USA

Kyle Patel
Colorado School of Mines, EE Dept.
Golden, CO 80401, USA

Christina Bonnington
University of Mississippi, EE Dept.
University, MS 38677, USA

Anne Graham
University of Mississippi, EE Dept.
University, MS 38677, USA

Madison Lee
Colorado School of Mines, EE Dept.
Golen, CO 80401, USA

Allison Tanner
Colorado School of Mines, EE Dept.
Golden, CO 80401, USA

Mohamed Al Sharkawy
Arab Academy for Science and Technology, ECE Dept.
Alexandria, Egypt

AUGUST 2023 REVIEWERS

**Allam M. Ameen
Giovanni Angiulli
Alireza Baghai-Wadji
Behrokh Beiranvand
Mahendran C.
Matteo Cicuttin
Dileepan Dhanasekaran
Biswajit Dwivedy
Kuikui Fan
Piotr Gas
Zi He
Ming Jin
Lida Kouhalvandi**

**Koushick
Andrzej A. Kucharski
Fabrizio Loreto
Durga Prasad Mishra
Michel M. Ney
Mahdi Oliaei
Sivaprakash S. C.
M. Mohammadi Shirkolaei
Varun Singh
Marsellas Waller
Wentao Yuan
Theodoros Zygiridis**

TABLE OF CONTENTS

An Implicit Adaptive FDTD Mesh Generation Technique based on Tetrahedrons
Weiran Zhang, Zikun Xu, Huaiyun Peng, Juan Chen, and Chunhui Mou 548

A Novel 3-D DGTD-FDTD Hybrid Method with One Overlapping Virtual Layer
Qingkai Wu, Kunyi Wang, Zhongchao Lin, Yu Zhang, and Xunwang Zhao 558

Research on a Two-stage Plane Adaptive Sampling Algorithm for Near-field Scanning
Acceleration
Xiaoyong Liu, Peng Zhang, and Dan Shi 566

Fast Coupling Iterative Algorithm for Media Rough Surface with Multiple Targets Below
Lilan Lei 575

Efficient Improved Local Time Stepping with the Leapfrog Scheme for Transient 3-D
Electromagnetic Analyses
Minxuan Li, Qingkai Wu, Zhongchao Lin, Yu Zhang, and Xunwang Zhao 587

Novel Characteristic Mode Basis Functions Accelerating Iteration Convergence of CMM
for Analyzing Electromagnetic Scattering Problems
Fei Guo, Zhonggen Wang, Yufa Sun, Wenyan Nie, Pan Wang, and Juan Wu 594

Gain-enhanced and Mechanical Reconfigurable Slot Antenna with Metasurface
Xueyan Song, Ang Dong, Xuping Li, Yunqi Zhang, Haoyuan Lin, Yapeng Li, and
Hailong Yang 602

Wideband Monostatic RCS Prediction of Complex Objects using Support Vector
Regression and Grey-wolf Optimizer
Zhourui Zhang, Pengyuan Wang, and Mang He 609

High-precision Solution of Monostatic Radar Cross Section based on Compressive
Sensing and QR Decomposition Techniques
Chaofan Shi, Yufa Sun, Mingrui Ou, Pan Wang, and Zhonggen Wang 616

Analytical Solution of Eddy Current in Parallel Conducting Strips for Low-frequency
Shielding Purposes
Hamzeh M. Jaradat, Qasem M. Qananwah, Ahmad M. Dagamseh, and
Qasem M. Al-Zoubi 625

An Implicit Adaptive FDTD Mesh Generation Technique based on Tetrahedrons

Weiran Zhang¹, Zikun Xu¹, Huaiyun Peng², Juan Chen^{1*}, and Chunhui Mou¹

¹School of Information and Communication Engineering
Xi'an Jiaotong University, Xi'an, 710049, China
1538162321@qq.com, *chen.juan.0201@mail.xjtu.edu.cn

²National Key Laboratory of Electromagnetic Environment
Qingdao, 266107, China

Abstract – A novel implicit adaptive FDTD mesh generation method based on tetrahedrons is proposed in this paper. According to the vertex coordinates of tetrahedrons which make up an object, non-uniform grid lines are generated first. These grid lines are constrained by the structure of the object and follow three rules mentioned in the paper. The first rule is to find demarcation points of the object and drop grid lines on these points. The second rule is to make sure all mesh sizes are less than one-tenth of the wavelength by adding more grid lines. The last rule is to densify mesh at the fine structure of the object. Then by comparing the positional relationship between center points of Yee cells and tetrahedrons, the object can be discretized by Yee cells. Finally, numerical examples are given to verify the validity and accuracy of this novel method.

Index Terms – Adaptive mesh generation, FDTD, tetrahedron.

I. INTRODUCTION

Maxwell's equations reveal the universal law of electromagnetic phenomena in nature. All electromagnetic problems can be attributed to the solution of Maxwell's equations when given boundary conditions. The finite-difference time-domain (FDTD) method, as one of the three common electromagnetic field numerical calculation methods, starts from Maxwell's curl equations in differential form and uses Yee cells to get results [1]. Electric field and magnetic field are distributed alternately in space and time, and they are solved gradually in time. The FDTD algorithm is widely used in time domain analysis of electromagnetic scattering and antenna design because it is easy to comprehend and implement [2].

When using the FDTD method to study the electromagnetic characteristics of a target, the discrete object model consisting of Yee cells is needed. For a simple

model, Yee cells can be obtained by dividing the model manually. However, for a complex model, it is very complicated to generate Yee cells artificially and easy to produce errors. Therefore, using the theory of computer graphics and computer-aided computation to generate Yee cells is necessary [3].

Currently, there are not so many types of commercial software on the market that generate Yee cells. Some famous graphics software such as AutoCAD, SolidWorks, or Gmsh are used to construct three-dimensional (3D) models of targets and to provide triangular or tetrahedral meshes in different file formats [4]. Thus, some scholars have already proposed a part of theory and approaches to convert other mesh formats into Yee cells. In 1993, W. Sun proposed a ray tracing method of 3D FDTD surface mesh generation based on triangular mesh [5]. In 1996, W. Heinrich proposed an optimal FDTD mesh generation method, which laid the foundation for the emergence of adaptive mesh, but this method could only solve the simple shape model with relatively regular shape [6].

In recent years, the number of generation methods for Yee cells based on tetrahedral mesh has also increased. Y. Gong proposed a scheme using the theory of convex geometry to judge the position relationship between Yee cell and each tetrahedral element of the object [7]. However, each judgment needs to compare eight vertices of Yee cell and discuss six circumstances, which is time consuming and complex. Liang Hui proposed an improved method which only needs to judge the position relationship between the center point of Yee cells and the tetrahedron [8]. The target model was reconstructed by Yee cells effectively without multiple calculation, but only a sphere example was verified. Besides, this method was only suitable for convex bodies and cannot be used to handle more complicated structures. Z. Yu also adopted an algorithm to judge the positional relationship between points and tetrahedrons,

and verified an aircraft model by Yee cells [9]. Nonetheless, only uniform mesh is used in the paper, while how to divide the object with non-uniform mesh is not mentioned. But non-uniform mesh is also needed in practice because it can save total calculation time while ensuring the accuracy of subdivision.

Therefore, a novel and effective method which can convert the tetrahedral data into Yee cells is proposed in this paper. According to the tetrahedral mesh data, we find the coordinates of demarcation points and drop grid lines on them. In addition, we guarantee all mesh sizes are less than one-tenth of the wavelength, and we densify mesh only at the precise structure of the object. Finally, the non-uniform Yee cells meshes are generated. Three examples are given to prove the accuracy of the subdivision method.

II. ADAPTIVE MESH GENERATION

There are two steps for the adaptive mesh generation based on tetrahedral data. The first step is to divide the target object with non-uniform grid lines. The second step is to discretize the target object by Yee cells.

A. Generate non-uniform grid lines

In this section, the method of how to place grid lines reasonably is presented. At present, many sorts of computer aided design (CAD) software can provide tetrahedral meshes, which can be used as front-end data for non-uniform grid lines placement. Gmsh is a commercial finite element mesh generator, which supports reading of various file formats and can generate tetrahedral meshes automatically. The tetrahedral data exported from Gmsh includes the coordinates of all vertex and vertex index numbers of each tetrahedron.

First, the 3D boundary of the target should be found to determine the setting range of non-uniform grid lines. According to the vertex coordinates, we can easily find the maximum and the minimum values of the object along x -, y -, z -axes. Depending on these values, an optimal bounding box can be constructed as shown in Fig. 1.

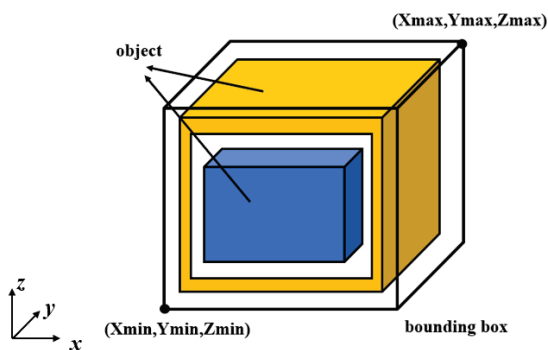


Fig. 1. The optimal bounding box.

All grid lines should be limited in this box to reduce the dividing time and internal storage.

The next step is to place adaptive grid lines in the box. There are three rules for the subdivision.

The first rule is to make sure grid lines fall on demarcation points. We find a novel way to seek out the demarcation points depending on the data of tetrahedrons. The coordinates of these points are all the places where objects have right-angle structures. Bringing in these points can make the partition more accurate, and this method is suitable for many different shapes of objects. For an object having slit structure, we can accurately locate the position of the gap, and get the width and length of the gap. For the object similar to the structure of a rectangular patch antenna, the position of the patch, as well as the width and length of the lines, can also be found precisely. Take a model for example. Two cuboid boxes are nested together. The outer cuboid box has a hollow structure in the middle, while the inner cuboid box is solid. Figure 2 shows the cross section of this model on the x - z plane. The yellow part represents the outer entity box, the blue part represents the inner one, and the orange dots represent the demarcation points.

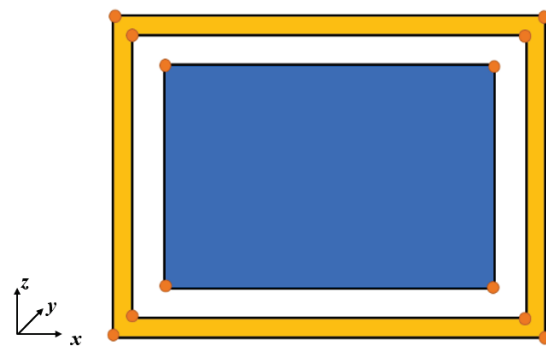


Fig. 2. The cross section to illustrate demarcation points.

It can be easily seen that these orange dots are the key points that distinguish the physical object from the air, where the structural changes happen. If the coordinates of these points can be obtained and the grid lines are guaranteed to fall in these points, the accuracy of subdivision can be improved. Although these points can be clearly seen from Fig. 2, we can only use the front-end data of tetrahedrons without seeing the model, so an algorithm is needed to implement it.

Take the x direction for example. A tetrahedron has four points and four surfaces. Three points in different positions can determine a plane. If three points of a tetrahedron have the same coordinates on the x -axis, the surface formed by these three points of this tetrahedron must be perpendicular to the x -axis. At this time, record the

coordinate value of this surface in the x direction and store it in an array. As is shown in Fig. 3, record the x coordinate value of surface ABC.

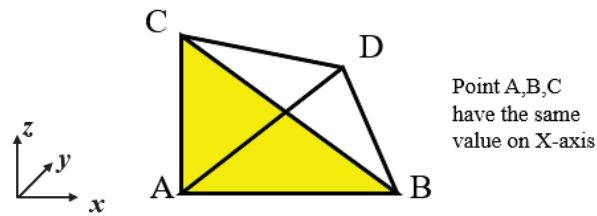


Fig. 3. The algorithm to find demarcation points.

After traversing all tetrahedrons and getting all qualified x coordinate values in the array, we sort this array and eliminate the duplicate values. Then we get the final demarcation points in the x direction. The demarcation points in the y and z directions can be obtained in the same way as those in the x direction. After finding the demarcation points and putting grid lines on these points, a sketch map is shown in Fig. 4.

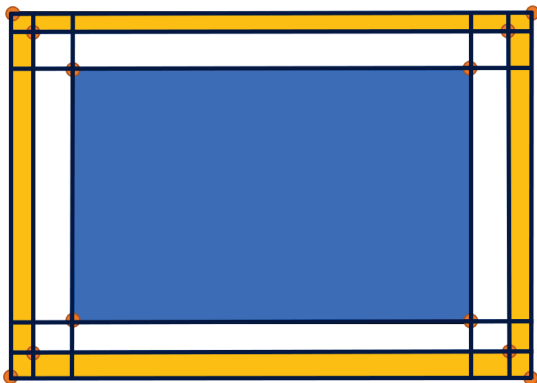
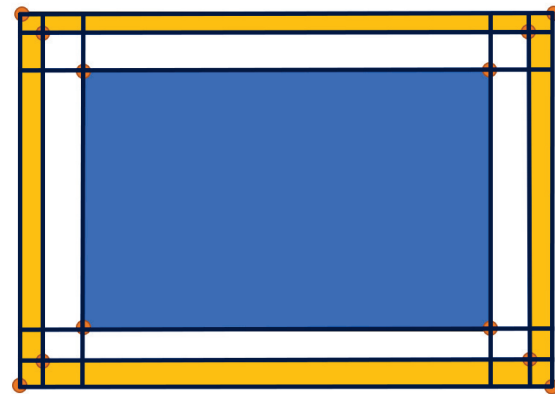


Fig. 4. The grid lines after the first rule.

The second rule is to find the upper limit for the size of the maximum mesh. Taking wavelength as the benchmark, it is to find the minimum number of grids in each coordinate direction per wavelength, while the wavelength refers to the highest frequency of simulation. According to the FDTD algorithm, this number means the spatial sampling rate for the input signal, so it has a strong influence on the quality of the results and on the calculation time. Increasing it leads to a higher accuracy, but unfortunately it also increases the total calculation time. A good compromise between calculation time and the achievable accuracy is the default value of ten. Therefore, the size of the maximum mesh should be less than one-tenth of the wavelength.

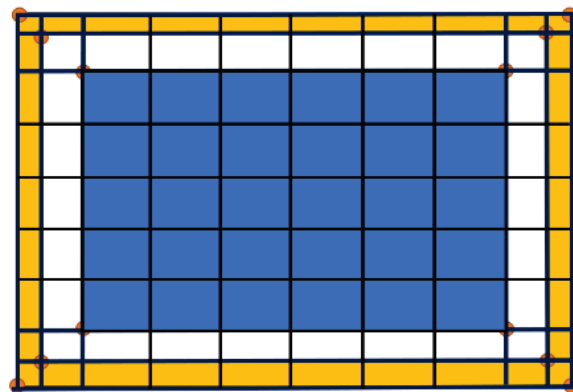
In order to satisfy the second rule, we have to add new grid lines. Because the intervals of the grid lines

obtained based on the first rule may be greater or less than one-tenth of wavelength. For the grids less than one-tenth of wavelength, no processing is required. For the grids larger than one-tenth of wavelength, new grid lines have to be added evenly until all of them are less than one-tenth of wavelength. The process can be described from Figs. 5 (a) and 5 (b).



Larger than 1/10 wavelength

(a)



(b)

Fig. 5. The grid lines after processing the second rule: (a) Original schematic diagram and (b) grid lines added.

The third rule is to adjust the mesh size depending on the tetrahedrons because the density of tetrahedrons corresponds to the fineness of the object structure. In addition, we believe that the tetrahedral mesh obtained by Gmsh is reasonable and accurate. It is wise to use small grids where the tetrahedrons are dense and large grids where the tetrahedrons are sparse. Therefore, we come up with a new algorithm.

Take the x direction for example. As shown in Fig. 6, if a tetrahedron ABCD falls completely between two adjacent grid lines in the x direction, it indicates that this

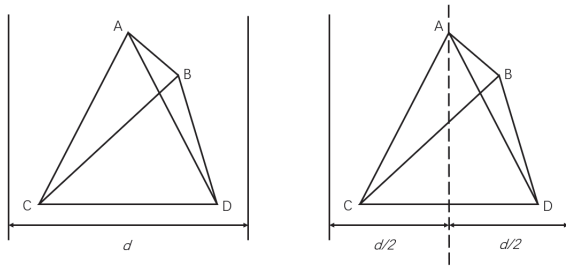


Fig. 6. The algorithm description of the third rule.

grid is imprecise. A new grid line should be added in the middle of this grid which splits it into two new grids, and both are half of the original grid.

Continue judging whether the tetrahedron still falls completely in the new grid. If so, do that step again, and this time the grid size becomes a quarter of the original one. Until the tetrahedron does not fall completely into only one grid, the work is done.

The previous model is still used to illustrate this process. In Fig. 7 (a), supposing a tetrahedron ABCD (only

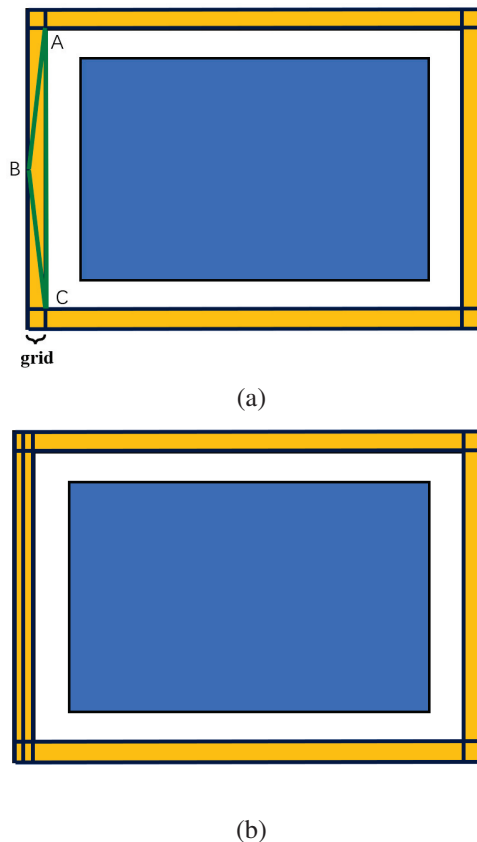


Fig. 7. The process for the third rule: (a) Original schematic diagram and (b) grid line added.

three points A, B, C are shown in the cross section) falls completely in a grid, it means that this grid is imprecise. A new grid line should be added as shown in Fig. 7 (b).

In addition, we also consider an extreme case so as to make the algorithm more general and robust. If a tetrahedron falls in a grid and the size of the tetrahedron is too small compared with the size of the grid, the work of adding new grid lines will be repeated, resulting in excessive density. For example, in a microstrip antenna, the thinnest layer of material needs to be divided into two grids along the thickness direction, while a smaller mesh is unnecessary. Therefore, we add a new step that allows operators themselves to input the expected minimum grid size into the program to avoid too small a mesh. When the mesh size calculated by the algorithm is smaller than the expected value, the program will retain the previous grid lines without further processing.

To summarize, the adaptive mesh generation of the object needs to generate grid lines in the bounding box, and these lines should follow the three rules as mentioned above. The whole process can be described as: Find the demarcation points of the object according to the first rule, and drop the grid lines on these points. Then add grid lines evenly to ensure that all grids are less than one-tenth of the wavelength, satisfying the second rule. Finally, the sizes of tetrahedral meshes are compared with the sizes of grids, and more grid lines are added only at the fine structure of the object. All grid lines for the subdivision are shown in Fig. 8.

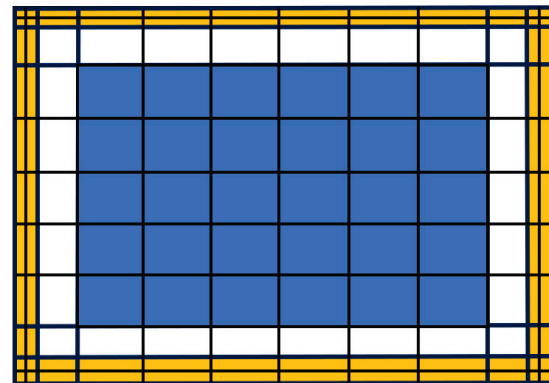


Fig. 8. The final subdivision result.

B. Use Yee cells to reconstruct the target object

From part A, grid lines are generated. Supposing the shadow part represents the entity object in Fig. 9, the key for the object discretization by Yee cells is to determine which Yee cells are located in the object. That is, to compare the position of every center point of Yee cells with the actual location of the object.

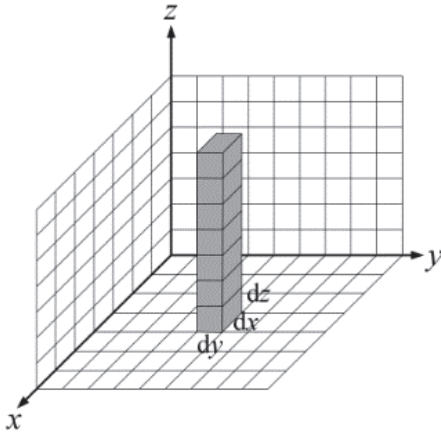


Fig. 9. The grid lines and Yee cells.

Before we import the algorithm of determining whether a point is inside an object in three dimensions, we first introduce a special situation judging whether a point is on a plane in two dimensions in order to make it easier to understand. And in this situation, it also has a practical use because in some structures the metal layer of the object can be seen as non-thickness, which can reduce the amount of mesh. We just need to mark the index numbers of grids where the metal is and set the tangential electric fields to zero on these locations.

According to the front-end data, the surface of the object is formed by several triangles. The key to judge the positional relationship between a point and a plane is to judge it between a point and a triangle. If a point is in one of the triangles forming the plane, the point must be in that plane.

Suppose the three vertices of a triangle are A , B , C , and the vertices are in anticlockwise direction. P is the point to be tested. According to the mathematical formula, if the results of three cross-product expressions have the same sign, the point P is in the triangle ABC .

$$\begin{cases} CP \times CA \\ AP \times AB \\ BP \times BC \end{cases}. \quad (1)$$

After we have finished the case in two dimensions, now let's look at the circumstance in three dimensions. Based on the front-end data, the object is formed by several tetrahedrons. The key to judge the positional relationship between a point and an object is to judge it between a point and a tetrahedron. We use directed volume to finish the judgment in three dimensions, and this is an analogy to the two dimensions.

Suppose there are four vertices of a tetrahedron A , B , C , D , and the vertices are in anticlockwise direction. P is the point to be tested.

Assuming the coordinates of the five points A , B , C , D , P are, respectively,

$$\begin{aligned} A &= (x_1, y_1, z_1), \\ B &= (x_2, y_2, z_2), \\ C &= (x_3, y_3, z_3), \\ D &= (x_4, y_4, z_4), \\ P &= (x, y, z), \end{aligned}$$

and according to the cross products algorithm, the formula for calculating the directed volume of tetrahedron can be regarded as the calculation of determinant. For example, the formula for calculating the volume of tetrahedron $ABCD$ is

$$V_{abcd} = \begin{vmatrix} x_1 & y_1 & z_1 & 1 \\ x_2 & y_2 & z_2 & 1 \\ x_3 & y_3 & z_3 & 1 \\ x_4 & y_4 & z_4 & 1 \end{vmatrix}. \quad (2)$$

We can use the coordinates of point P to replace points A , B , C , and D , respectively and get the results of the other directed volume of tetrahedrons $BCDP$, $ACDP$, $ABDP$, $ABCP$ in sequence. Judge and compare whether these five values have the same sign. If they have the same sign, it is proved that the point P is located in the tetrahedron $ABCD$, and vice versa [10].

Using the algorithm mentioned above, we can mark the Yee cells that are located inside the tetrahedron, and these Yee cells must also be located inside the object. By traversing all tetrahedrons, we can find all Yee cells which are inside the object, and according to the positions of them we can restore the object.

III. EXAMPLES AND RESULTS

In this section, we illustrate the efficiency and the robustness of the adaptive mesh generation method for FDTD simulation. The first model is an electrically large aircraft model, which is chosen to verify the stability of the method in processing a large number of meshes. The second model is a rectangular microstrip patch array, which is used to show the accuracy of the non-uniform grid generation technique. A schematic of a human skull serves as the third model, demonstrating the ability of our algorithm to handle complicated models. In all examples, we use CPML as absorbing conditions. For the meshes in absorbing boundary, we use uniform meshes, and the sizes are one-tenth of the wavelength in air. The meshes between object and absorbing boundary are also one-tenth of the wavelength in air. These meshes are all added directly in our FDTD computation process. In order to present partition results more clearly, we don't add these meshes in subdivision pictures. The total number of meshes is only calculated in the object area.

A. The aircraft model

We use an aircraft model to verify the performance of the program based on the meshing algorithm mentioned before. The fuselage of the plane is about 20 m. The height is 3.78 m, and the wingspan is 13.20 m. The

simulation frequency range is from 0.1 GHz to 0.5 GHz. According to the second rule in the last part, the maximum size of the mesh should be less than one-tenth of the wavelength, we finally choose it as 0.05 m. The minimum size of the mesh is 0.015 m. For all meshes, 0.05 m refers to the largest side length, while 0.015 m refers to the smallest side length. The smallest side and the largest side, however, may not exist in one single mesh. On the basis of adaptive mesh generation algorithm, the number of grids in the modeling area is $643 \times 393 \times 79 = 19,963,221$. The original model is shown in Fig. 10 (a), while the model discretized by Yee cells is shown in Fig. 10 (b). An enlarged image of the discretized rear side of the aircraft is shown in Fig. 10 (c).

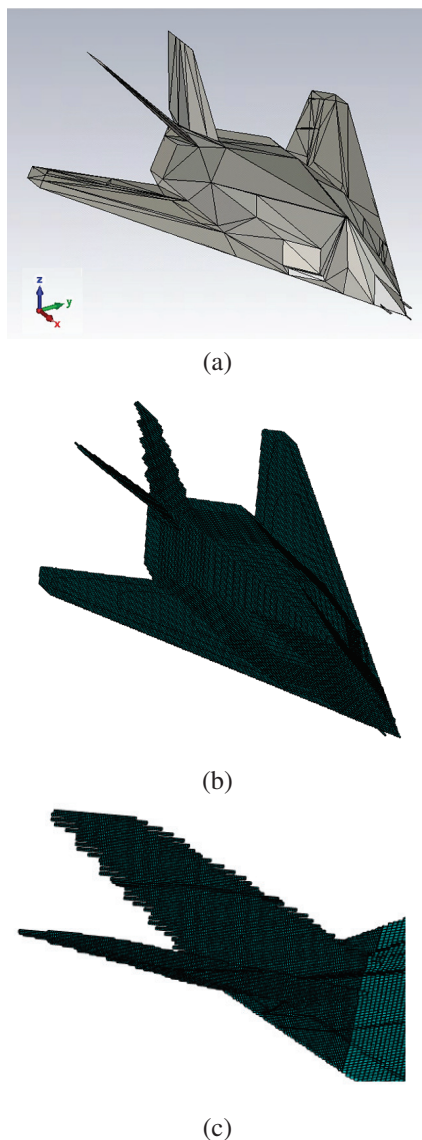


Fig. 10. Aircraft model and subdivision results: (a) Original model, (b) subdivision results and (c) a part of discretized rear side of the aircraft.

The radar cross section (RCS) of this model is calculated by using the electromagnetic simulation software CST. We use the FIT engine in CST with hexahedral meshes. Meanwhile, the FDTD method is also used to calculate the RCS based on the subdivision mesh in Fig. 10. We also employ the message passing interface (MPI) method to save time. This method of parallel processing may distribute the entire computation work among several processor nodes, increasing calculation speed. After setting the incident plane wave from the belly of the aircraft, the RCS results over frequency are shown in Fig. 11. The RCS results on $\phi = 0$ and $\phi = 90$ plane at 250 MHz are shown in Fig. 12.

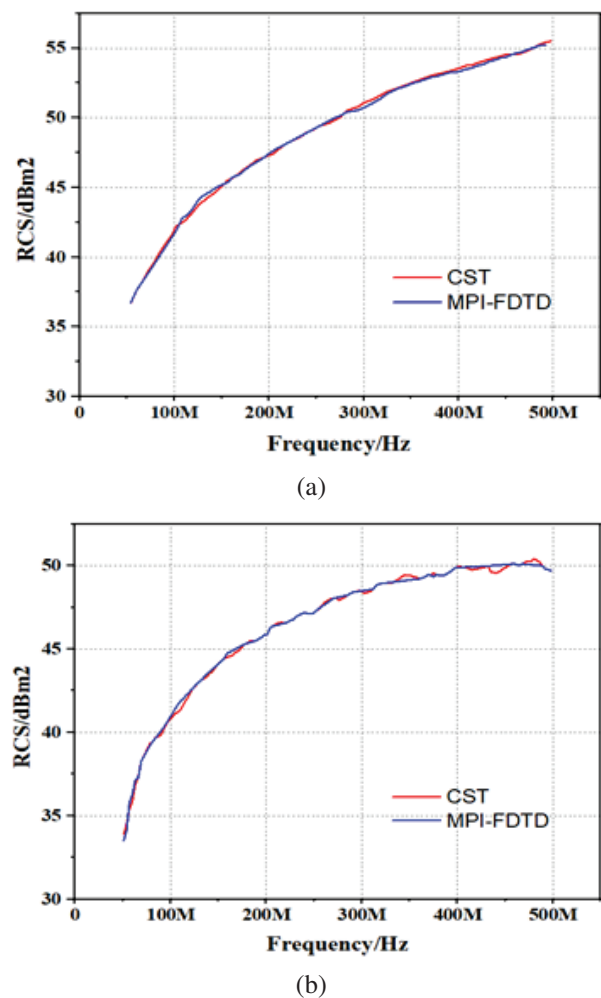


Fig. 11. Radar cross section results over frequency: (a) Forward RCS and (b) backward RCS.

We can see from Figs. 11 and 12 that the simulation results obtained by CST software and the FDTD method are consistent with each other, which verifies the stability of the adaptive mesh generation method proposed in this paper.

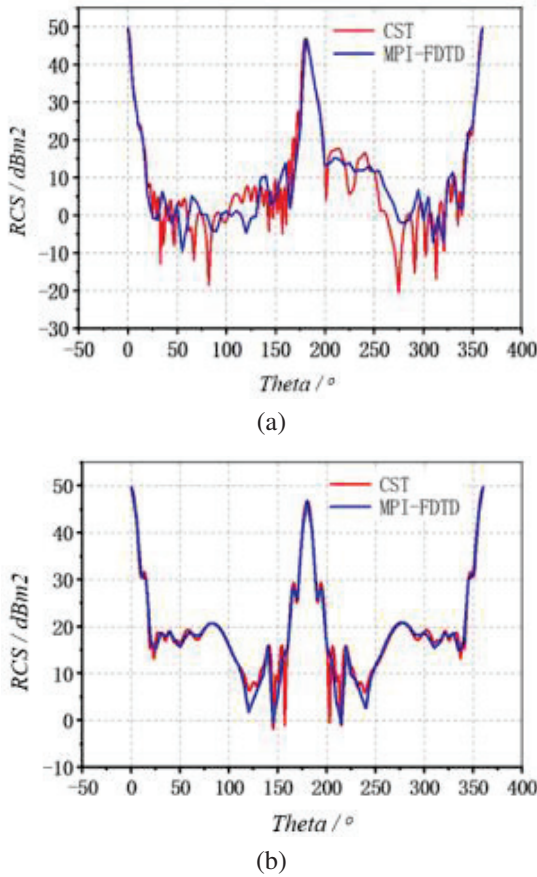


Fig. 12. Radar cross section results at 250 MHz: (a) $\phi = 0$ and (b) $\phi = 90$.

B. 2x2 rectangular microstrip patch antenna array

The second model is a patch antenna array. The antenna contains three parts: patch, dielectric substrate, and ground floor. The relative permittivity of the substrate is 2.2, and the thickness is 6 mm. The structure of the antenna is shown in Fig. 13, and the values of the parameters are given in Table 1.

The simulation frequency range is from 2.2 GHz to 2.7 GHz, and the operating frequency is 2.4 GHz.

Table 1: Parameters of the patch antenna array

Parameter	Length (mm)	Parameter	Length (mm)
Metal thickness	0.12	L_p	36.8
W_m	8	W_p	48
W_l	1.7	S_y	101
L_m	23	S_x	88
L_l	45.3		

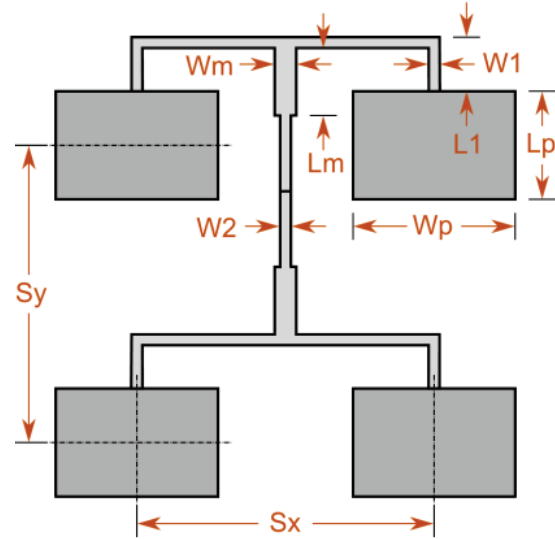


Fig. 13. Top view of the patch antenna array.

The minimum mesh size is 0.12 mm. According to the adaptive mesh generation algorithm, the number of grids in modeling area is $44 \times 62 \times 5 = 13,640$. The original model is shown in Fig. 14 (a). The tetrahedral

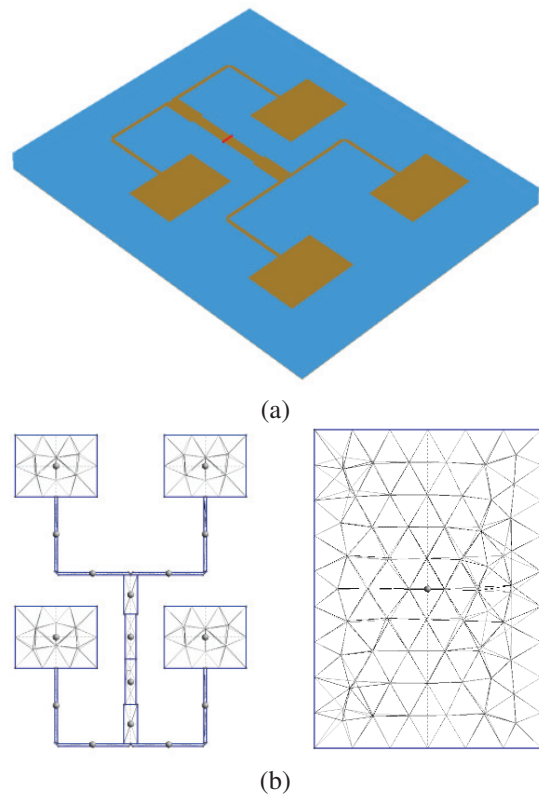


Fig. 14. Patch antenna array model and subdivision results: (a) Original model, (b) tetrahedral meshes, (c) subdivision results and (d) feed lines partially enlarged.

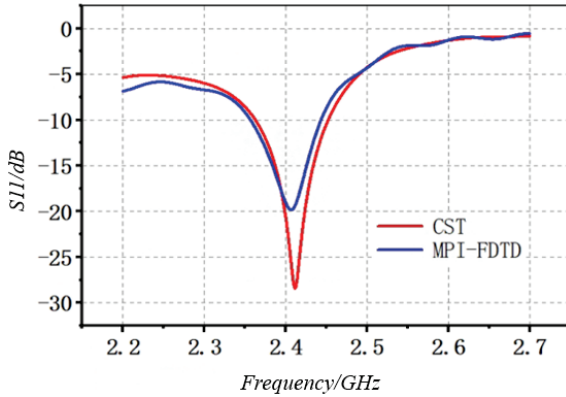


Fig. 15. S_{11} parameter over frequency.

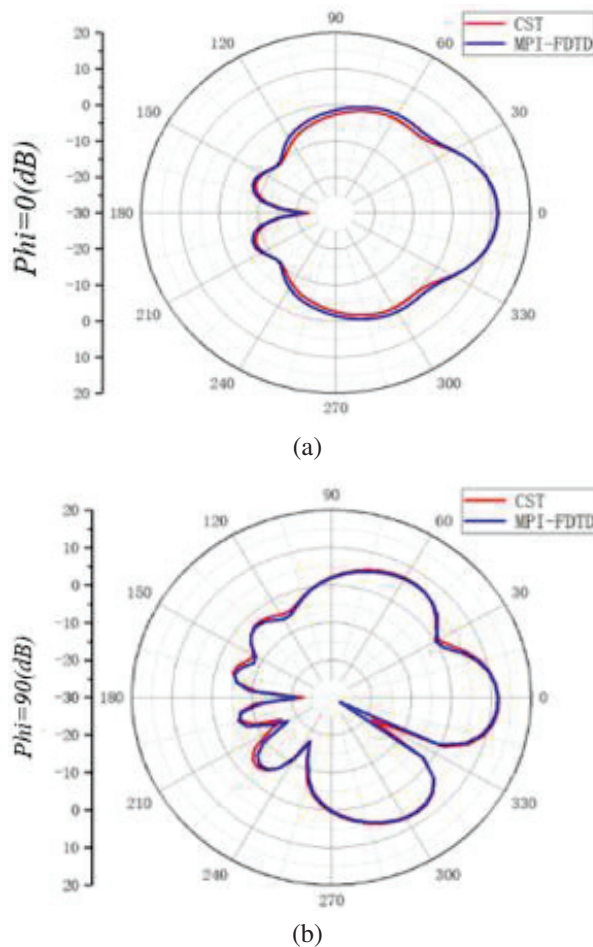


Fig. 16. Radiation patterns at 2.4 GHz: (a) $\phi = 0$ and (b) $\phi = 90$.

meshes for the patch and substrate are separately shown in Fig. 14 (b). The model discretized by Yee cells is shown in Fig. 14 (c), and the thin feed lines partial of the model is enlarged in Fig. 14 (d).

We also use two ways to obtain results. One is by using the CST software, the other is by using FDTD method based on the subdivision cells in Fig. 14. The comparison results of S_{11} and radiation patterns are shown in Figs. 15 and 16.

It can be seen from Figs. 15 and 16 that two groups of results are consistent with each other. Because the feed lines in the network are very narrow, a little change in the width of lines can lead to the electromagnetic performance variation of the antenna. Therefore, the high precision of the mesh generation algorithm proposed in this paper can be verified through this example.

C. The human skull model

We use this example to illustrate the performance of our method in dealing with complicated models. The whole model consists of many organs and skin tissues: skull, trachea, brain, eyes, tongue, teeth, jaw, etc. [11]. The simulation frequency range is from 1 GHz to 5 GHz. The maximum size of the mesh should be less than one-tenth of the wavelength; we finally chose 2 mm. The minimum size of the mesh is 0.5 mm. The total number of grids in the modeling area is approximately 7,400,000. The original model is shown in Fig. 17, while the model discretized by Yee cells is shown in Fig. 18.

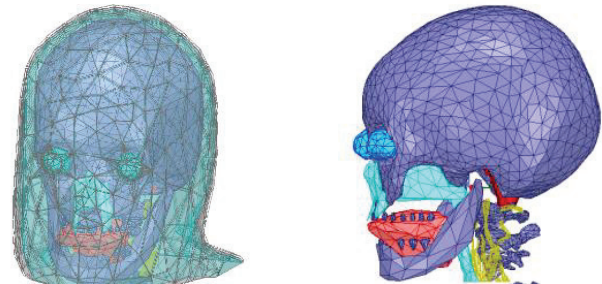


Fig. 17. Human skull model: (a) Whole model and (b) inside model without skin and fat.

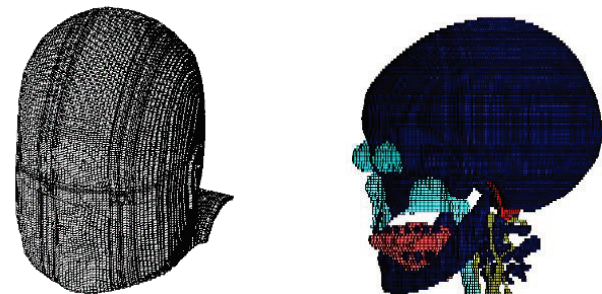


Fig. 18. Subdivision results: (a) Whole model subdivision and (b) inside model subdivision.

Using our approach, the discretized skull model of Yee cells is in good agreement with the original one, as

shown in Figs. 17 and 18. The findings can demonstrate that our technique is capable of handling intricate models, since the skull model is made up of a variety of organ forms with different shapes.

IV. CONCLUSION

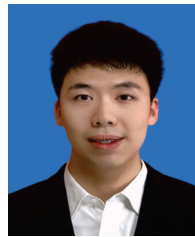
In this paper, a novel method for adaptive FDTD mesh generation based on front-end tetrahedral data is presented. The first step is to divide a target object with grid lines. These grid lines are constrained in the bounding box and are placed in a non-uniform way based on the structure of the object. The second step is to compare the positional relationship between center points of Yee cells and the object, which can realize the object discretization by Yee cells. Relevant principles are explained, and two simulation examples are verified. The first example shows the stability and reliability of this method in processing a large-scale example. The second one shows the accuracy of the non-uniform mesh technique. The correctness of the research content is proved.

ACKNOWLEDGMENT

This work was supported by National Natural Science Foundations of China (No. 61971340 and 62122061) and by National Key Research and Development Program of China (No. 2020YFA0709800).

REFERENCES

- [1] K. S. Yee, "Numerical solution of initial boundary value problems involving Maxwell's equation in isotropic media," *IEEE Trans*, vol. 14, 1966.
- [2] A. Taflov and S. C. Hagness, *Computational Electrodynamics: The Finite-Difference Time-Domain Method*, 3rd edition, 2005.
- [3] Y. Srisukh, J. Nehrbass, F. L. Teixeira, J.-F. Lee, and R. Lee, "An approach for automatic grid generation in three-dimensional FDTD simulations of complex geometries," *IEEE Antennas and Propagation Magazine*, vol. 44, no. 4, pp. 75-80, Aug. 2002, doi: 10.1109/MAP.2002.1043151.
- [4] H. Zhu, C. Gao, H.-L. Chen, Z.-H. Shi, and X.-H. Xu, "The research on FDTD mesh generation and visualization technology," *2012 6th Asia-Pacific Conference on Environmental Electromagnetics (CEEM)*, Shanghai, China, pp. 282-284, 2012, doi: 10.1109/CEEM.2012.6410622.
- [5] W. Sun, C. A. Balanis, M. P. Purchase, and G. Barber, "Three-dimensional automatic FDTD mesh generation on a PC," *Proceedings of IEEE Antennas and Propagation Society International Symposium*, vol. 1, pp. 30-33, 1993, doi: 10.1109/APS.1993.385409.
- [6] W. Heinrich, K. Beilenhoff, P. Mezzanotte, and L. Roselli, "Optimum mesh grading for finite-difference method," *IEEE Transactions on Microwave Theory and Techniques*, vol. 44, no. 9, pp. 1569-1574, Sep. 1996, doi: 10.1109/22.536606.
- [7] Y. Gong, Z. Wu, and Z. Dai, "Convex object Yee cell model building based on convex geometries," *Journal of Tsinghua University*, vol. 47, no. 9, pp. 1521-1525, 2007.
- [8] L. Hui and S. Zuxun, "FDTD mesh-generating and visual realization based on triangle-patch," *Computer Simulation*, vol. 26, no. 11, pp. 106-109 (in Chinese), 2009.
- [9] Z. Yu, W. Zhao, L. Xu, and X. Shi, "A novel mesh generation method for FDTD without ray-tracing," *2017 Sixth Asia-Pacific Conference on Antennas and Propagation (APCAP)*, Xi'an, China, pp. 1-3, 2017, doi: 10.1109/APCAP.2017.8420508.
- [10] J. W. Boardman, "Analysis, understanding, and visualization of hyperspectral data as convex sets in n space," *Proceedings of SPIE - The International Society for Optical Engineering*, vol. 2480, pp. 14-22, 1995.
- [11] S. N. Makarov, G. M. Noetscher, J. Yanamadala, M. W. Piazza, and S. Louie, "Virtual human models for electromagnetic studies and their applications," *IEEE Reviews in Biomedical Engineering*, vol. 10, pp. 95-121 [Online], 2017. Available: <https://www.nevaelectromagnetics.com/vhp-female-2-2>.



Weiran Zhang was born in Shanxi, China. He received the B.S. degree from Xi'an Jiaotong University, Xi'an, China, in 2017, in information engineering. He is currently working in Xi'an Jiaotong University as a postgraduate. His research interests include mesh generation and computational electromagnetics.



Zikun Xu was born in Jiujiang, China. He received the B.S. and M.S. degrees from Xi'an Jiaotong University, Xi'an, China, in 2023, all in electromagnetic field and microwave technology. His research interests are parallel FDTD methods based on MPI.



Huaiyun Peng was born in Hubei, China. He received the Ph.D. degree from Xidian University, Xi'an, China, in 2017, in radio physics.

He is currently working in National Key Laboratory of Electromagnetic Environment, China Research Institute of Radiowave Propagation, Qingdao, China, as a researcher. Her research interests include radio wave propagation, numerical method for electromagnetic field, and electromagnetic scattering.



Juan Chen was born in Chongqing, China. She received the Ph.D. degree from Xi'an Jiaotong University, Xi'an, China, in 2008, in electromagnetic field and microwave technology. She is currently working in Xi'an Jiaotong University, Xi'an, China, as a professor. Her research

interests include the computational electromagnetics, microwave device design, etc.



Chunhui Mou was born in Yantai, China. She received the B.S. and M.S. degrees from Xidian University, Xi'an, China, in 2012 and 2015, and the Ph.D. degree from Xi'an Jiaotong University, Xi'an, China, in 2023, all in electromagnetic field and microwave technology. She is

currently working in Xi'an Jiaotong University, Xi'an, China, as a postdoctoral researcher. Her research interests include the fast FDTD method, FDTD mesh generation method, and multi-physical field calculation.

A Novel 3-D DGTD-FDTD Hybrid Method with One Overlapping Virtual Layer

Qingkai Wu, Kunyi Wang, Zhongchao Lin, Yu Zhang, and Xunwang Zhao

School of Electronic Engineering
Xidian University, Xi'an, 710071, China
wuqingkai@stu.xidian.edu.cn, zclin@xidian.edu.com

Abstract – Compared with the traditional finite difference time-domain (FDTD) method, the discontinuous Galerkin time-domain (DGTD) method may face the issue of intense computation. In this paper, a novel 3-D DGTD-FDTD hybrid method is proposed to dramatically reduce the unknowns of the DGTD method. Instead of the common mass-lumped elements, this virtual layer of the Yee grid is implemented on the intersecting boundary, which simplifies the mesh generation and reduces the number of unknowns. To validate the proposed method, two examples of sphere scattering and horn antenna are considered. The simulation results demonstrate the effectiveness of the proposed method.

Index Terms – Discontinuous Galerkin time-domain method, finite-difference time-domain method, hybrid method, transient analysis.

I. INTRODUCTION

The discontinuous Galerkin time-domain (DGTD) method is a transient numerical method with high accuracy and has been reported extensively in recent years [1–3]. The DGTD method is capable of using unstructured meshes resembling the finite-element time-domain (FETD) method [4], which enables it to solve models with complex structures and maintain high accuracy at the same time. Numerical fluxes are employed in the DGTD method to separate unknowns shared among adjacent elements, allowing them to be independent. Therefore, explicit time integration schemes such as leapfrog scheme can be used in the DGTD method [5] as in the FDTD method [6, 20]. However, with an increase in the number of computing elements, the unknowns of the DGTD method will inevitably rise, and consequently the computational efficiency will decrease.

The traditional way to reduce the unknowns of DGTD method is to use the hybrid mesh instead of the unstructured mesh in single form [7]. An alternative approach is using different forms of basis functions for different types of meshes to reduce the total number of unknowns [8]. However, in most cases, the resulting computational efficiency is still limited. A more recent

novel idea is to use the FDTD method to deal with hexahedral elements in hybrid mesh [9]. This idea makes use of the fast and simple characteristics of the FDTD method, and avoids the staircasing error of the FDTD method, which is more direct and effective than the traditional method of reducing unknowns. This scheme has been verified by comparing the results with those obtained by FETD [9–13]. The standard procedure requires the grids in the common area should be divided into tetrahedral elements for the FETD method. A similar operation was introduced into the solution of the DGTD method [14] in recent years. It achieves good results by one common buffer. However, the existence of instance buffer [14–16] hinders the generation of hybrid meshes and efficiency.

In this paper, a novel three-dimension explicit DGTD-FDTD hybrid method is proposed. There is only one overlapping virtual layer of the FDTD zone between the DGTD and the FDTD zone to replace the buffer zone. Thereby the calculation of electromagnetic fields towards FDTD zone shares similarities with the domain decomposition FDTD (DD-FDTD) method detailed in [17, 18]. The electromagnetic fields from the FDTD zone are converted to numerical fluxes and added into DGTD's formulations. Moreover, the tetrahedral elements used in the DGTD zone can be generated more freely, and it is not required to generate additional elements [13] to meet the mass-lumped element's standard. Such a procedure saves considerable computation time compared with traditional hybrid strategy. To validate the proposed strategy, two examples are presented in this paper. The comparison of different methods' results validates this method's accuracy and high performance.

II. THE FORMULATION OF DGTD

After testing by the discontinuous Galerkin method, the weighted integral form of source free Maxwell equations are

$$\begin{cases} \int v \left[\epsilon \frac{\partial E}{\partial t} - \nabla \times H \right] d\Omega = 0, \\ \int v \left[\mu \frac{\partial H}{\partial t} + \nabla \times E \right] d\Omega = 0. \end{cases} \quad (1)$$

Here, v is the weight function, ε represents the permittivity, μ is permeability, and Ω denotes the space of the tetrahedral element.

The numerical fluxes with respect to element i is defined at the element boundary. j represents the adjacent element of element i .

$$\begin{aligned}\hat{n} \times H^* &= \hat{n} \times H_i + \frac{Z^j}{Z^i + Z^j} \hat{n} \times (H_j - H_i) \\ &\quad - \frac{1}{Z^i + Z^j} \hat{n} \times (\hat{n} \times (E_j - E_i)), \\ \hat{n} \times E^* &= \hat{n} \times E_i + \frac{Y^j}{Y^i + Y^j} \hat{n} \times (E_j - E_i) \\ &\quad + \frac{1}{Y^i + Y^j} \hat{n} \times (\hat{n} \times (H_j - H_i)).\end{aligned}\quad (2)$$

Here, \hat{n} is the unit outward normal vector of face of the element i . E^* and H^* represent the numerical fluxes, Z is the impedance and Y is the admittance.

The integral procedure results in

$$\left\{ \begin{array}{l} \int v(\nabla \times E^*) d\Omega = \int v(\nabla \times E_i) d\Omega \\ \quad + \int v \left[\frac{Y^j}{Y^i + Y^j} \hat{n} \times (E_j - E_i) \right] d\Omega \\ \quad + \int v \left[\frac{1}{Y^i + Y^j} \hat{n} \times (\hat{n} \times (H_j - H_i)) \right] d\Omega, \\ \int v(\nabla \times H^*) d\Omega = \int v(\nabla \times H_i) d\Omega \\ \quad + \int v \left[\frac{Z^j}{Z^i + Z^j} \hat{n} \times (H_j - H_i) \right] d\Omega \\ \quad - \int v \left[\frac{1}{Z^i + Z^j} \hat{n} \times (\hat{n} \times (E_j - E_i)) \right] d\Omega. \end{array} \right. \quad (3)$$

By substituting equation (3) into equation (1) we obtain the Maxwell-DGTD equation in matrix form

$$\left\{ \begin{array}{l} \varepsilon M \frac{\partial E_i}{\partial t} = S H_i + \sum_{p=1}^4 (F_{eh}(H_j - H_i) - F_{ee}(E_j - E_i)), \\ \mu M \frac{\partial H_i}{\partial t} = -S E_i - \sum_{p=1}^4 (F_{he}(E_j - E_i) + F_{hh}(H_j - H_i)). \end{array} \right. \quad (4)$$

Here, E and H are expanded by the 2nd-order hierarchical basis function, defined in [19], M denotes the mass matrix, S denotes the stiffness matrix, F_{ee} , F_{eh} , F_{hh} and F_{he} are the numerical flux matrices, ε represents the permittivity, μ is permeability, j represents the adjacent element of element i , and p is the number of the surface of the tetrahedral elements.

The leapfrog scheme has been adopted in the iteration process. Furthermore, Equation (1) can be converted into the explicit scheme as follows:

$$\left\{ \begin{array}{l} \frac{E_i^{n+1} - E_i^n}{\Delta t} \\ = S H_i^{n+\frac{1}{2}} + \varepsilon^{-1} M^{-1} \sum_{p=1}^4 \left(F_{eh}(H_j^{n+\frac{1}{2}} - H_i^{n+\frac{1}{2}}) - F_{ee}(E_j^n - E_i^n) \right), \\ \frac{H_i^{n+\frac{1}{2}} - H_i^{n-\frac{1}{2}}}{\Delta t} \\ = -S E_i^n - \mu^{-1} M^{-1} \sum_{p=1}^4 \left(F_{he}(E_j^n - E_i^n) + F_{hh}(H_j^{n-\frac{1}{2}} - H_i^{n-\frac{1}{2}}) \right). \end{array} \right. \quad (5)$$

M^{-1} represents the inverse of the mass matrix. ε^{-1} and μ^{-1} denote the reciprocals of permittivity and permeability.

III. VIRTUAL LAYER STRATEGY FOR DGTD-FDTD HYBRID METHOD

A. DGTD-FDTD hybrid strategy

As shown in Fig. 1 (a), a hybrid strategy is proposed. One layer of FDTD Yee grids will be set as the virtual layer, and the virtual layer overlaps the tetrahedral DGTD elements. Since the generation of tetrahedral mesh in the DGTD zone will not be affected by the virtual layer, the tetrahedron elements can be directly connected. While the conventional needs one extra hybrid region, the grid needs to be split into six tetrahedral elements. As a result, the split elements will add obvious unknowns.

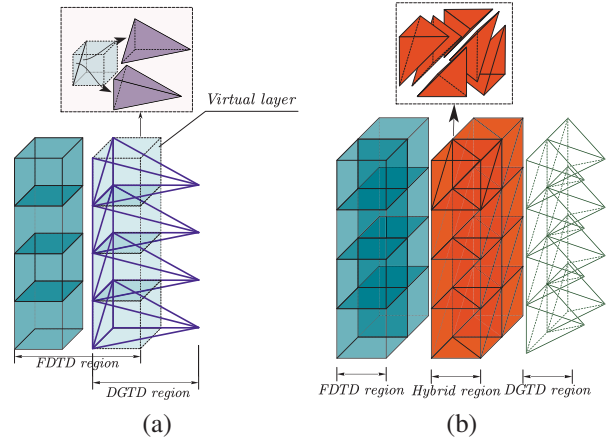


Fig. 1. Two types of hybrid mesh: (a) The virtual layer hybrid mesh and (b) the conventional hybrid mesh.

In the conventional hybrid method, the hybrid region is calculated by a new algorithm merged from DGTD and FDTD method. A new mass matrix is built by both basis functions in DGTD and the field-components in FDTD.

$$\begin{bmatrix} M_{DGTD} & M_{hybrid} \\ M_{hybrid} & M_{FDTD} \end{bmatrix} \begin{bmatrix} N_{DGTD} \\ l_{FDTD} \end{bmatrix}. \quad (6)$$

In Equation (6), M_{DGTD} and M_{FDTD} represent the respective mass matrix. And the M_{hybrid} is calculated by the projection of the overlapped basis functions and field-components. The FDTD method is simple and fast. So we convert the 3-D hybrid problem into two 2-D problems and keep the characteristics of FDTD at the same time.

In our proposed method, we apply a concise strategy to communicate DGTD and FDTD zones. The fields from the FDTD zone will be transmitted through the boundary of two types of meshes to the DGTD zone. The fields from the DGTD zone will be transmitted on the red face of the virtual layer to the FDTD zone. Consequently, there will be no mutual interference during the communication of the two methods based on the virtual layer hybrid strategy.

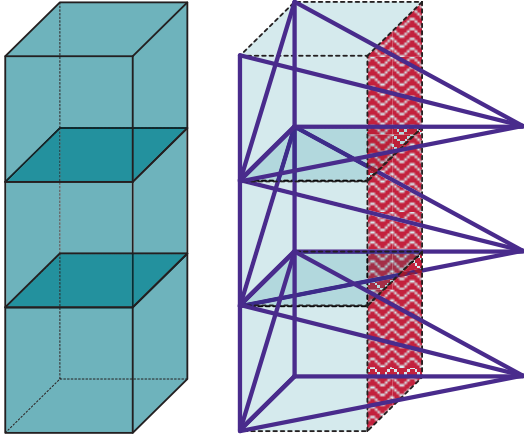


Fig. 2. The locations of the electric field denoted by red arrows in virtual layer.

In Fig. 2, when the FDTD zone needs to update the fields, it will use the electric field (E-field) from the face (indicated with red). The E-field for FDTD method on the face of the virtual layer, meanwhile inside the overlapping DGTD zone, can be directly calculated by the DGTD method in explicit scheme, using $E = \sum_{i=1}^n e_i N_i$. E represents the vector field in the DGTD zone, N_i stands for the basis functions, and e_i is the expansion coefficients [19].

The electromagnetic fields from the FDTD zone to the DGTD zone must be converted to the form of numerical fluxes. Specifically, the fields from the FDTD zone will be approximated by fields value averaged spatially. The edge basis function will directly use the field value of FDTD zone due to the application of hierarchical basis functions. Correspondingly, the field value of the hypotenuse edge inside the square is the average value of the surrounding electric fields (E-field) following [8]. Besides, the magnetic field (H-field) should be averaged from the real and virtual zone of FDTD in order to maintain time consistency to avoid the error accumulation from the inconsistency in time. The entire calculation process is exhibited in Fig. 3.

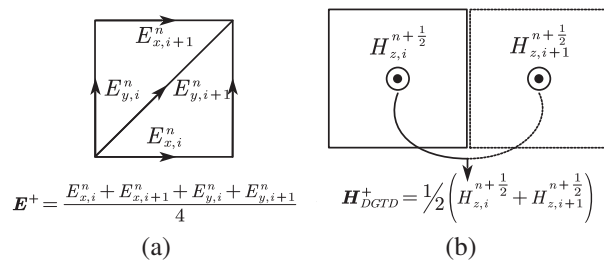


Fig. 3. The assembly of FDTD EH-fields for DGTD zone: (a) The constituent components of E^+ and (b) the constituent components of H^+ .

The E^+ or H^+ (see Fig. 3) will be treated as the E_j or H_j to introduce into the numerical fluxes in Eq. (2) to update fields.

B. Generation of hybrid mesh

To generate the hybrid mesh with one virtual layer, we follow the procedure in Fig. 4. Firstly, in the whole computation domain, the structured grids used for the FDTD method will be divided, and then the grids intersecting with the object should be dug out based on the geometric contour of the object (surrounded by the blue line). After that, the innermost layer of structured grids is set as the virtual layer (between blue and red lines). Finally, the region inside the red lines is set as the DGTD region, and tetrahedral elements will be generated there.

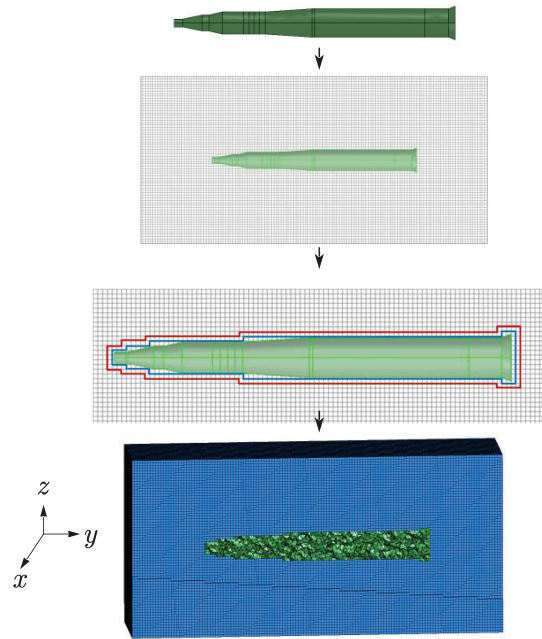


Fig. 4. The mesh of DGTD-FDTD hybrid zone. The operation of dividing grids. The comparison of hybrid mesh in 2-D.

C. The marching-on-in-time algorithm

To ensure that the combination of the two methods is self-consistent, the following process of explicit iteration has been implemented:

FDTD and DGTD method will iterate normally when they are not in the overlapping zone.

In the overlapping zone, updating of the E-field for two methods is as follows:

- 1) DGTD should update the E-field on the inner face of the virtual layer.
- 2) FDTD method updates the E-fields.

- 3) Fields from the FDTD zone should be combined and converted to the form of numerical fluxes for the updated H-field in the DGTD zone.

Updating of the H-field for two methods:

- 1) DGTD should update the H-field on the inner face of the virtual layer.
- 2) FDTD method updates the H-fields.
- 3) Fields from the FDTD zone should be combined and converted to the form of numerical fluxes for the next iteration's updated E-field in the DGTD zone.

Since the explicit iteration scheme is employed here, the Δt in the presented work is chosen based on the following rule:

$$\Delta t = \min\{\Delta t_{DGTD}, \Delta t_{FDTD}\}. \quad (7)$$

The choice of Δt_{FDTD} follows the rule in [6], The selection of Δt_{DGTD} satisfies the Lemma 2.9 in [21]:

$$\frac{1}{\sqrt{\mu_i \epsilon_i}} \Delta t_{DGTD} \left[2\alpha_i + \beta_i \max\left(\sqrt{\frac{\epsilon_i}{\epsilon^+}}, \sqrt{\frac{\mu_i}{\mu^+}}\right) \right] < \frac{4V_i}{P_i}. \quad (8)$$

In Eq. (8), α_i and β_i are coefficients obtained by [21], V_i and P_i are the volume and the total area of the element i , respectively, ϵ_i is the permittivity of the element i , μ_i is the permeability of the element i , the superscript "+" indicates the adjacent elements of the element i .

Because the calculation of hybrid region doesn't involve new algorithms, the selection of Δt just needs to satisfy the CFL (Courant-Friedrichs-Lewy) conditions [6].

IV. NUMERICAL RESULTS

All of the numerical simulations were carried out on the Intel Xeon Gold 6140 CPU @ 2.30 GHz with 64 GB of RAM. And the programming language is implemented in Fortran 95.

A. Sphere scattering

In this example, a perfect electric conductor (PEC) sphere's bistatic scattering is computed by different methods. This sphere's radius is 0.5 m, and the planewave's propagation direction is $-z$. Figure 5 represents the grids and tetrahedrons of the sphere model. The outermost five layers of the FDTD zone are set as the uniaxial perfectly matched layer (UPML) boundary. Correspondingly, the comparison model of the DGTD method is truncated by five UMPL layers, too, as illustrated in Fig. 5. The mesh size of both models' tetrahedral elements is $\lambda/10$; the Yee grids in all models are generated with mesh size $\lambda/15$. In addition, the FDTD method used a conformal algorithm [22] to improve accuracy.

The comparison of bistatic scattering of different methods at the frequency of 400 MHz is highlighted in

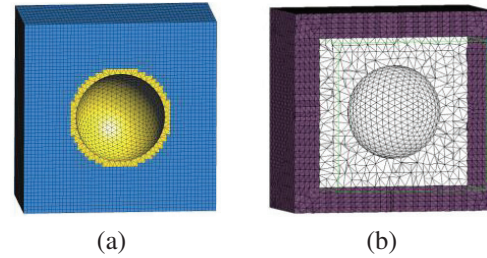


Fig. 5. Mesh of different methods: (a) The mesh of hybrid method and (b) the mesh of conventional DGTD method.

Fig. 6. Based on the results of this comparison, it can be inferred that the results of the hybrid method and method of moment (MoM) are in good agreement, and it has prominently better results than the FDTD method. It can be found that the hybrid method has an obvious improvement on accuracy when compared with the FDTD method. Results of the comparison between the conventional DGTD method and the proposed method are listed in Table 1. It is evident that the proposed method has a tremendous advantage compared with the conventional

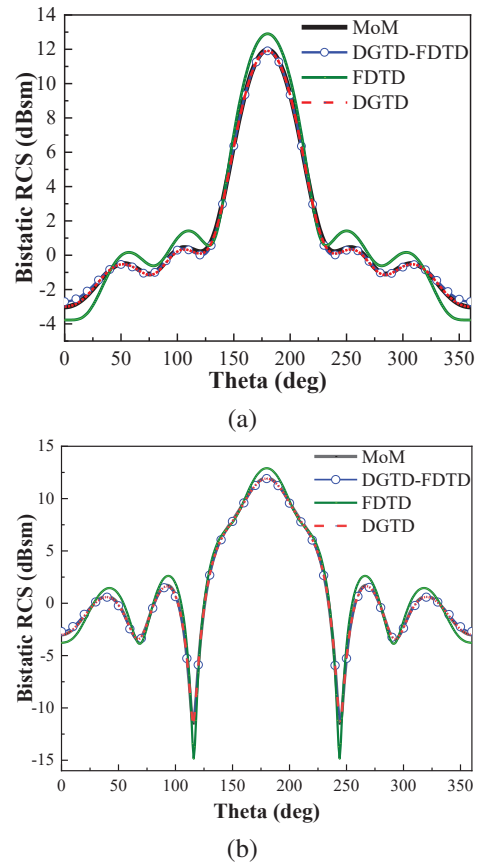


Fig. 6. Comparison of bistatic RCS computed by different methods: (a) xoz plane and (b) yoz plane.

Table 1: Performance of Different Methods

Method	Memory (MB)	Unknowns	Solution Time (s)
DGTD	9283	11,435,600	10,901
Conventional method (with buffer zone)	1504	1,190,454	757
Proposed method	1037	861,134	522

DGTD method. The proposed method is 20 times faster than the DGTD method, which significantly reduces the computation memory and improves the efficiency. On the other hand, due to the virtual layer, the proposed method can save calculation time significantly compared with the conventional strategy.

B. Horn antenna

The second example is a horn antenna. It is one kind of broadband antenna. Because of its opening structure, it is quite suitable for computation with the proposed hybrid method. Figure 7 represents the hybrid mesh of

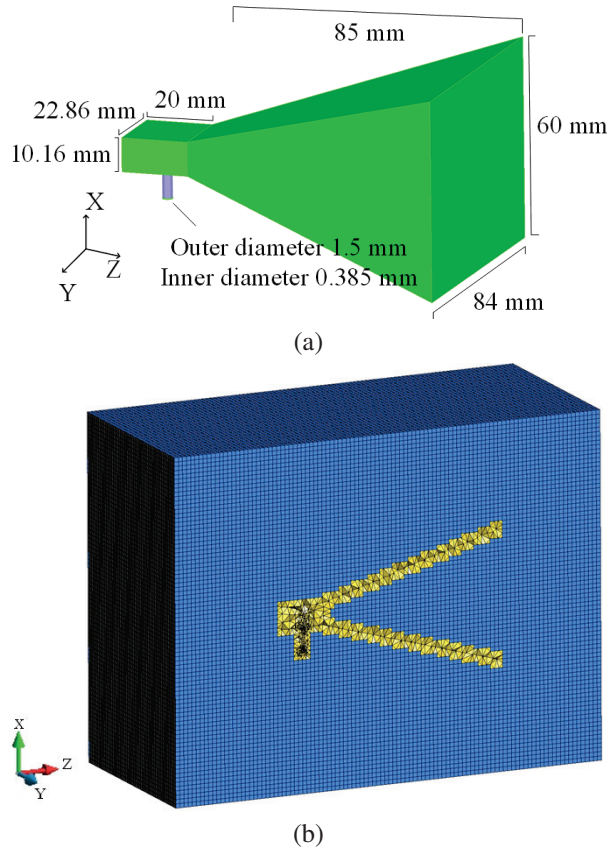


Fig. 7. The horn antenna model: (a) The model with the geometric size of the horn antenna and (b) the hybrid mesh for DGTD-FDTD method.

the horn antenna model. The mesh size of both models' tetrahedral elements is $\lambda/10$; the mesh size of the Yee grids for FDTD method in both models is $\lambda/15$.

A coaxial wave port is used to excite the antenna, which is inside the DGTD zone. The exciting signal is chosen as a modulated Gaussian pulse with bandwidth of 5~15 GHz. From Figs. 8 (a)-(c), we can find that the gain pattern and S-parameter of the proposed DGTD-FDTD hybrid method is in good agreement with the finite element method (FEM) and DGTD method. In Fig. 8 (d), the comparison of port's voltage of DGTD and DGTD-FDTD method is given to prove the stability of hybrid method. From Table 2, the results demonstrate that the hybrid method still has a significant advantage in the unknowns compared with the DGTD method. From the comparison, the proposed method exhibits a 15.28 times improvement in overall computing efficiency and nearly 13 times improvement in memory usage.

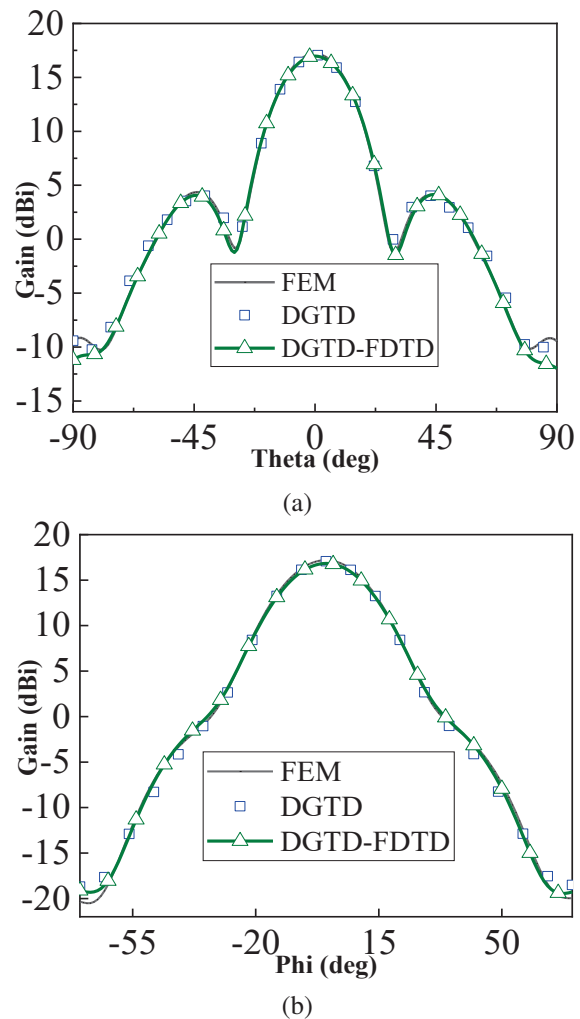


Fig. 8. Continued.

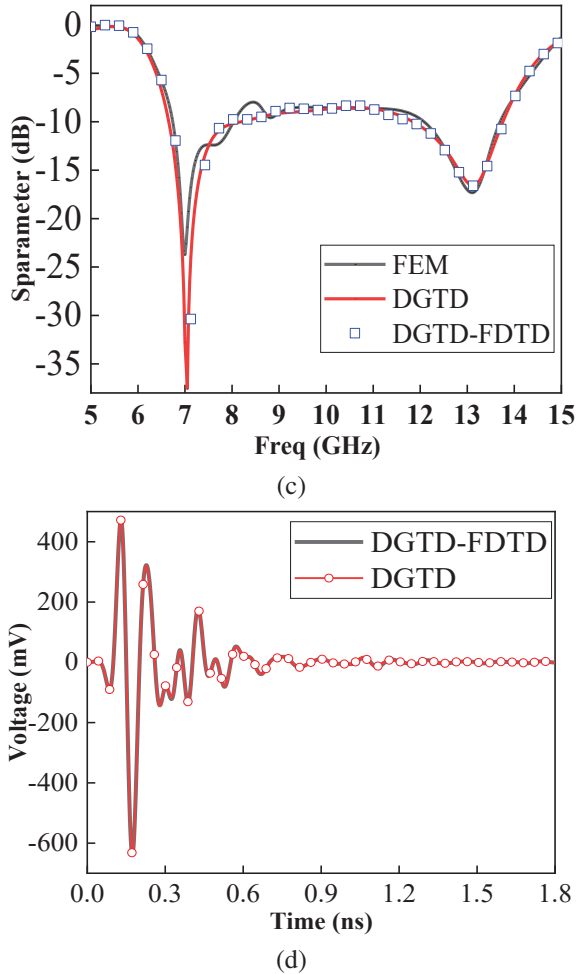


Fig. 8. The comparison of different methods: (a) The gain pattern of xoz-plane, (b) the gain pattern of yoz-plane, (c) the result of S-parameter and (d) the time-domain result of port's voltage.

Table 2: Performance of different methods

Method	Memory (MB)	Unknowns	Solution Time (s)
FEM	5431	1,359,660	1523
DGTD	26,150	8,377,240	14,732
The conventional method	2340	751,330	1315
The proposed method	2132	626,944	964

V. CONCLUSION

In this paper, a novel 3-D hybrid method of the DGTD and FDTD method is introduced. One virtual layer of FDTD has been adapted to maintain the independence of the communication between the two meth-

ods. On this premise, it is not necessary to add additional elements for the actual common buffer as it is the conventional hybrid method. Consequently the unknowns will obviously be reduced. As a result, there will be a significant improvement in memory usage and computational efficiency compared with the conventional DGTD method and hybrid method.

ACKNOWLEDGMENT

This work was supported in part by Key Research and Development Program of Shaanxi (2022ZDLGY02-01, 2021GXLH-02, 2023-ZDLGY-09,) and the Fundamental Research Funds for the Central Universities (QTZX23018).

REFERENCES

- [1] J. S. Hesthaven and T. Warburton, *Nodal Discontinuous Galerkin Methods: Algorithms, Analysis, and Applications*. New York, NY, USA: Springer, pp. 1-39, 2008.
- [2] S. Dosopoulos and J.-F. Lee, "Interior penalty discontinuous Galerkin finite element method for the time-dependent first-order Maxwell's equations," *IEEE Trans. Antennas Propag.*, vol. 58, no. 12, pp. 4085-4090, Dec. 2010.
- [3] M. Li, Q. Wu, Z. Lin, Y. Zhang, and X. Zhao, "A minimal round-trip strategy based on graph matching for parallel DGTD method with local time-stepping," *IEEE Antennas Wirel Propag Lett.*, vol. 2, pp. 243-247, Feb. 2023.
- [4] J.-M. Jin, *The Finite Element Method in Electrodynamics*. Hoboken, NJ, USA: Wiley, pp. 514-523, 2015.
- [5] J. Chen and Q. Liu, "Discontinuous Galerkin time-domain methods for multiscale electromagnetic simulations: A review," *Proc. IEEE*, vol. 101, no. 2, pp. 242-254, Feb. 2013.
- [6] A. Taflov and S. C. Hagness, *Computational Electrodynamics: The Finite-difference Time-Domain Method*. Norwood, MA, USA: Artech House, pp. 638-649, 2005.
- [7] F. Hassan, "High-order discontinuous Galerkin method for time-domain electromagnetics on non-conforming hybrid meshes," *Math Comput Simul.*, no. 107, pp. 134-156, Jan. 2015.
- [8] Z. Xiao, B. Wei, and D. Ge, "A hybrid mesh DGTD algorithm based on virtual element for tetrahedron and hexahedron," *IEEE Trans. Antennas Propag.*, vol. 69, no. 4, pp. 2242-2248, Apr. 2021.
- [9] D. S. Balsara and J. J. Simpson, "Making a synthesis of FDTD and DGTD schemes for computational electromagnetics," in *IEEE J Multiscale Multiphys Comput Tech.*, vol. 5, pp. 99-118, June 2020.

- [10] T. Rylander and A. Bondeson, "Stable FEM-FDTD hybrid method for Maxwell's equations," in *Comput. Phys. Commun.*, vol. 125, no. 1-3, pp. 75-82, Mar. 2000.
- [11] J. Wang, Q. Ren, and F. Dai, "3-D hybrid finite-difference time-domain (FDTD)/wave equation finite element time-domain (WE-FETD) method," *Int. Symp. on Antennas, Propag and EM Theory (ISAPE)*, pp. 1-2, 2021.
- [12] N. V. Venkatarayalu, G. Y. Beng, and L.-W. Li, "On the numerical errors in the 2-D FE/FDTD algorithm for different hybridization schemes," *IEEE Microw. Wireless Compon. Lett.*, vol. 14, no. 4, pp. 168-170, Apr. 2004.
- [13] A. Sharbaf and R. Sarraf-Shirazi, "An unconditionally stable hybrid FETD-FDTD formulation based on the alternating-direction implicit algorithm," *IEEE Antennas Wirel Propag Lett.*, vol. 9, pp. 1174-1177, Dec. 2010.
- [14] S. G. Garcia, M. F. Pantoja, C. M. de Jong van Coevorden, A. R. Bretones, and R. G. Martin, "A new hybrid DGTD/FDTD method in 2-D," in *IEEE Microw. Wireless Compon. Lett.*, vol. 18, no. 12, pp. 764-766, Dec. 2008.
- [15] Q. Sun, Q. Ren, Q. Zhan, and Q. H. Liu, "3-D domain decomposition based hybrid finite-difference time-domain/finite-element time-domain method with nonconformal meshes," *IEEE Trans. Microw. Theory Techn.*, vol. 65, no. 10, pp. 3682-3688, Apr. 2017.
- [16] B. Zhu, J. Chen, W. Zhong, and Q. Liu, "A hybrid FETD-FDTD method with nonconforming meshes," *Commun Comput Phys.*, vol. 9, no. 3, pp. 828-842, Mar. 2011.
- [17] K. S. Yee, J. S. Chen, and A. H. Chang, "Conformal finite-different time-domain (FDTD) with overlapping grids," *IEEE Trans. Antennas Propag.*, vol. 40, no. 9, pp. 1068-1075, Sep. 1992.
- [18] F. Xu and W. Hong, "Domain decomposition FDTD algorithm for the analysis of a new type of E-plane sectorial horn with aperture field distribution optimization," *IEEE Trans. Antennas Propag.*, vol. 52, no. 2, pp. 426-434, Feb. 2004.
- [19] Y. Zhou, R. Huang, S. Wang, Q. Ren, W. Zhang, G. Yang, and Q. H. Liu, "An adaptive DGTD algorithm based on hierarchical vector basis function," in *IEEE Trans. Antennas Propag.*, vol. 69, no. 12, pp. 9038-9042, Dec. 2021.
- [20] J. Alvarez, L. D. Angulo, M. F. Pantoja, A. R. Bretones, and S. G. Garcia, "Source and boundary implementation in vector and scalar DGTD," in *IEEE Trans. Antennas Propag.*, vol. 58, no. 6, pp. 1997-2003, June 2010.
- [21] L. Fezoui, S. Lanteri, S. Lohrengel, and S. Piperno, "Convergence and stability of a discontinuous Galerkin time-domain method for the 3D heterogeneous Maxwell equations on unstructured meshes," *ESAIM, Math. Model Numer. Anal.*, vol. 39, no. 6, pp. 1149-1176, Nov. 2005.
- [22] S. Dey and R. Mittra, "A modified locally conformal finite-difference time-domain algorithm for modeling three-dimensional perfectly conducting objects," in *IEEE Microwave Opt. Tech. Lett.*, vol. 7, no. 9, pp. 273-275, June 1997.



Qingkai Wu was born in Yangzhou, Jiangsu, China, in 1997. He received the B.S. degree in electronic science and technology from Xidian University, Xi'an, China, in 2020. He is currently pursuing the Ph.D. degree with Xidian University, Xi'an, China. His current research interests

include transient electromagnetic analysis.



Kunyi Wang was born in Anqing, Anhui, China, in 1996. He received the B.S. degree in electronic information engineering from Tianjin University of Technology, Tianjin, China, in 2019. He is currently pursuing the Ph.D. degree with Xidian University, Xi'an, China. His current

research interests include transient electromagnetic analysis.



Zhongchao Lin was born in Hubei, China, in 1988. He received the B.S. and Ph.D. degrees from Xidian University, Xi'an, China, in 2011 and 2016, respectively. He joined Xidian University, in 2016, as a post doctoral fellow, where he was lately promoted as an associate professor. His

research interests include large-scale computational electromagnetics, scattering, and radiation electromagnetic analysis.



Yu Zhang received the B.S., M.S., and Ph.D. degrees from Xidian University, Xi'an, China, in 1999, 2002, and 2004, respectively. In 2004, he joined Xidian University as a faculty member. He was a visiting scholar and an adjunct professor with Syracuse University from 2006 to 2009.

As a principal investigator, he works on projects, including the Project of NSFC. He has authored four books: *Parallel Computation in Electromagnetics* (Xidian University Press, 2006), *Parallel Solution of Integral Equation-Based EM Problems in the Frequency Domain* (Wiley IEEE, 2009), *Time and Frequency Domain Solutions of EM Problems Using Integral Equations and a Hybrid Methodology* (Wiley, 2010), and *Higher Order Basis Based Integral Equation Solver* (Wiley, 2012), as well as more than 100 journal articles and 40 conference papers.



Xunwang Zhao was born in Shanxi, China, in 1983. He received the B.S. and Ph.D. degrees from Xidian University, Xi'an, China, in 2004 and 2008, respectively. He joined Xidian University, in 2008, as a faculty member, where he was lately promoted as a full professor. He was a

visiting scholar with Syracuse University, Syracuse, NY, USA, from December 2008 to April 2009. As a principal investigator, he works on several projects, including the project of NSFC. His research interests include computational electromagnetics and electromagnetic scattering analysis.

Research on a Two-stage Plane Adaptive Sampling Algorithm for Near-field Scanning Acceleration

Xiaoyong Liu^{1,2}, Peng Zhang¹, and Dan Shi¹

¹School of Electronic Engineering
Beijing University of Posts and Telecommunications, Beijing, 100876, China
liuxiaoyong@src.org.cn, shidan@bupt.edu.cn

²State Radio Monitoring Center Testing Center
Beijing, 100041, China

Abstract – As one of the most useful methods in electromagnetic interference (EMI) diagnosis, near-field (NF) scanning is widely used in electromagnetic compatibility (EMC) evaluation of complex devices under test (DUTs). In this paper, a two-stage plane adaptive sampling algorithm is proposed to reduce the acquisition time in the process of NF scanning and to make reconstruction of the radiation source more efficient. The sampling method is based on the region self-growth algorithm and the Voronoi subdivision principle, significantly reducing the number of NF samples in the stage of solving the radiation source model through uniform and non-uniform two-stage sampling. Two experiments were conducted to verify the correctness and effectiveness by comparing with the traditional uniform sampling method.

Index Terms – adaptive sampling, LOLA-Voronoi, near-field (NF) scanning, region self-growth, source reconstruction.

I. INTRODUCTION

With the increasing integration of modern electronic systems, more electronic components with higher frequency are integrated in smaller areas. The indenting of the distance between components makes the entire integrated circuit in a complex electromagnetic environment, and the electromagnetic interference (EMI) problems within and between systems are increasing. To solve the problem of EMI, it is necessary to locate the source of EMI. The continuous development of EMI source localization benefits from the uninterrupted improvement of electromagnetic radiation source reconstruction theory. From the original Huygens principle to the present, various radiation source reconstruction methods such as equivalent Huygens source [1–4] and equivalent dipole moment model [5–9] have been derived. The realization

of these methods requires the collection of radiation field information on the plane close to the real radiation source. Therefore, the electromagnetic near-field (NF) scanning system is also generated. In the past decade, the electromagnetic NF scanning system has played an increasingly important role in evaluating the electromagnetic compatibility (EMC) characteristics of integrated circuits, locating EMI sources, and efficiently reconstructing radiation sources. However, with the rapid developing of the integrated circuit industry and demand for compressing measurement time, the issue of NF scanning time is to be improved. Meanwhile, the NF sampling efficiency is seriously affected as the NF scanning probe itself will interfere with the NF distribution [10, 11] and cannot measure a single field component directly, and it requires various calibration and compensation techniques [12, 13].

To improve NF sampling efficiency, researchers are dedicated to accelerating the scanning process [14–27]. [19] proposes an adaptive sampling strategy based on a region growing algorithm, which identified regions with drastic changes in the NF on the basis of roughly uniform sampling, and then densely and uniformly sampled these regions. [20] proposes a sequential spatial adaptive sampling algorithm to achieve fast and accurate NF measurement based on the NF distribution characteristics of the scan plane.

During the author's work and research for constructing typical chip packages based on high-frequency electromagnetic theory of chip packaging, as well as EMC analysis using near-field scan technology, based on the region self-growth algorithm [19] and Voronoi subdivision principle [28, 29], this paper proposes a two-stage planar adaptive NF scanning algorithm, which solves the problem that the NF data acquisition time is too long in the process of NF scanning, and can efficiently image radiation sources in high-speed integrated circuit boards. In order to verify the proposed sampling

Supported by Beijing Natural Science Foundation.

algorithm, two practical cases were conducted using this method. The results show that the method can identify multiple radiation sources effectively and determine the area with intense radiation field transformation. Furthermore, It can accurately predict the near-field distribution of radiation sources at the scanning plane, and has good sampling and modeling performance.

II. TWO-STAGE PLANE ADAPTIVE SAMPLING ALGORITHM

With the increasing integration and power consumption of high-speed digital/analog chips, the current density inside the chip doubles and the number of the radiation sources is on the rise. Usually, more intensive sampling is required to restore the actual NF distribution, which consumes the massive sampling cost by collecting massive sampling point information. If we only focus the areas with significant NF variations, under-sampling may occur. Therefore, we propose a two-stage planar adaptive sampling algorithm, illustrated in Fig. 1, to deal with the trade-off between these two conflicting issues.

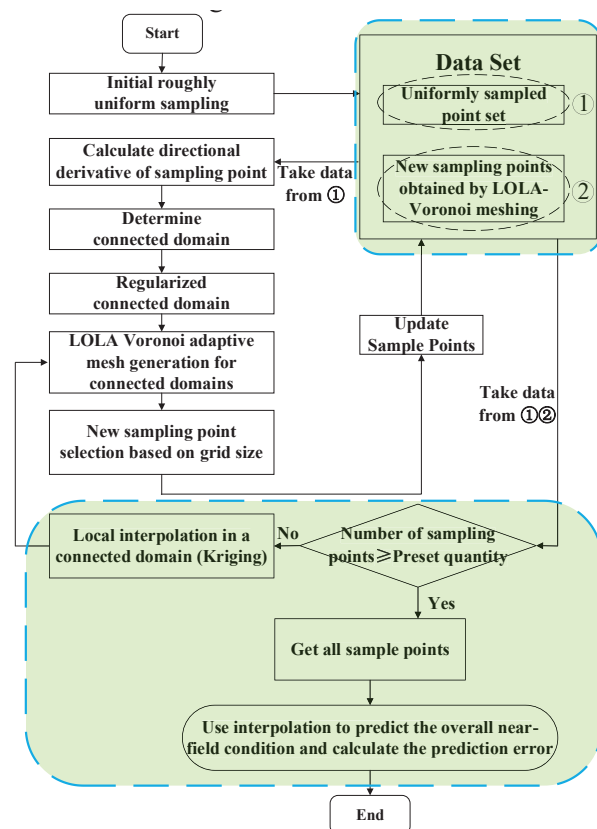


Fig. 1. Process of the two-stage plane adaptive sampling algorithm.

The connected domain in Fig. 1 refers to the initial region that needs to be carefully sampled according to the gradient calculation. As can be seen from Fig. 1, the

proposed sampling method mainly includes the following four steps

1) Determine the sampling surface and sampling interval according to the operating frequency and size of the device under test (DUT), and perform an initial rough uniform sampling with a larger sampling interval. Specifically determined according to the following rules [19]:

a) Sampling surface size: Make sure that the amplitude of the tangential electric field component at the edge of the sampling surface is less than 40 dB of the maximum electric field component amplitude on the entire sampling surface. In fact, this criterion is not fixed and can be adjusted appropriately according to the sampling accuracy. However, a higher threshold means larger sampling surfaces and more sampling points. Therefore, we choose 40 dB as the threshold to determine the size of the sampling surface.

b) Sampling interval: Generally speaking, there is no uniform standard to determining the sampling interval, which is often set according to the size of the sampling surface and the number of required sampling points, and is often set according to test experience. However, it should be noted that the sampling interval needs to satisfy the Nyquist spatial sampling criterion.

2) The data obtained from the initial uniform sampling is used in the optimized region self-growth algorithm to identify the central source point with drastic changes in the near field. From this source point, determine the area used for non-uniform sampling (referred to as the refinement area) and carry out reasonable regional expansion and regularization.

3) Sample the refinement area non-uniformly with the LOLA-Voronoi adaptive division method, and the sampling points are increased according to the preset number. In order to know NF information of all the sample points during the new sampling process using the LOLA-Voronoi method, the Kriging interpolation method should be used.

4) Gather the sampling point information obtained in the two stages, and use the Kriging interpolation method to restore the electromagnetic field distribution of the NF plane. Meanwhile, compare and analyze the advantages and disadvantages of the traditional dense uniform sampling method and the two-stage plane adaptive sampling algorithm in restoring the NF. Finally, calculate the relative error.

The two-stage plane adaptive sampling algorithm can densely sample in the area where the NF changes sharply, and it can roughly sample in the area where the field changes smoothly.

III. AUXILIARY SAMPLING ALGORITHM

From Section II, the core of high-efficiency and high-precision NF scanning is the two-stage plane adaptive sampling algorithm, which is mainly composed of the region self-growth optimization algorithm and the LOLA-Voronoi adaptive division algorithm. This section focuses on the two proposed algorithms, and calculates the relative error.

A. Region self-growth optimization algorithm

The proposed region self-growth algorithm for NF scanning sampling is evolved from the region growing method, which is used to segment infrared images, and its basic principle is to perform data segmentation based on the similarity of current amplitude values. In the process of determining the growing point, it is prone to getting stuck in a local optimal solution due to an unreasonable threshold setting during algorithm iteration. The innovation point of this algorithm is the optimization of the region self-growth algorithm and the way to determine the connected domain. The specific steps are as follows:

- 1) Determination of seed points: Solve the directional derivative of the discretized NF data obtained in the initial uniform sampling stage. The direction is from the point to be calculated to the adjacent point. For edge sampling points without adjacent points in some directions, the adjacent points in these directions are defaulted to 0. If all directional derivatives of the point to be solved are negative, the point is regarded as a seed point.
- 2) Region merging and regularization: First, assuming that the data obtained by NF sampling is the tangential electric field value E , the adjacent points of the seed point in the φ direction are denoted as E_φ , and the ratio is calculated:

$$R(f) = \left| \frac{E - E_f}{E} \right|. \quad (1)$$

If the absolute value of the minimum value among all the ratios of the seed points is less than the parameter d ($0 < d < 1$, d directly determines the number of growing points), the adjacent points in the direction of the corresponding minimum value are taken as growing points. Second, the growing point is incorporated into the seed point set as a new seed point, and the above process is repeated until all the initial rough sampling points are traversed. Then, the connected domain will be determined according to the obtained set of seed points, that is, a new sampling area will be determined with the seed point as the center and the surrounding adjacent points as the boundary. If the determined area overlaps to form an irregular shape area, the boundary point is appropriately expanded outward to form a regular rectangular

area. Its purpose is to prevent the problem of repeated sampling when using the LOLA-Voronoi adaptive division method for non-uniform sampling, and at the same time, the appropriate expansion of the area based on the seed point is conducive to restoring the area with sharp changes in the NF with higher accuracy and improving the accuracy of NF restoration.

The value of the above-mentioned parameter d is usually set to 0.1 initially, and is increased in steps of 0.05 until the identified growing point no longer increases.

B. LOLA-Voronoi adaptive division method

The algorithm mainly includes two parts. One part is Voronoi tessellation, which is an intuitive method to describe the grid density. By dividing polygons, the key areas to be studied are covered as evenly as possible. The other part is LOLA, which is mainly used to evaluate the intensity of nonlinearity at each node in the key area, and then serves as the criterion for dividing the polygon density.

Voronoi tessellation method is essentially a space-filling algorithm. A group of continuous polygons is determined according to the way that one node corresponds to one Voronoi cell, and then the area size of each Voronoi cell is estimated according to the Monte Carlo method. New grid points are selected according to the area size; that is, the area size of the Voronoi cell determines the division density of the area around the node. The edge of the continuous polygon is the vertical bisector of the line segment connected by adjacent nodes. The method is shown in Fig. 2.

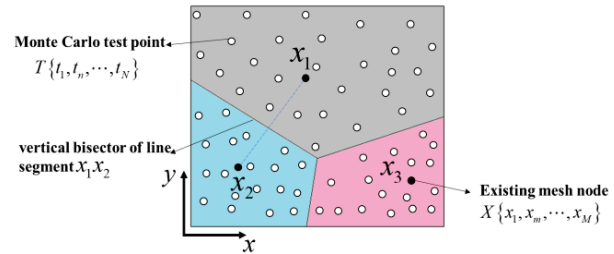


Fig. 2. Voronoi schematic.

In Fig. 2, t_n ($n = 1, 2, \dots, N$) represents the Monte Carlo test point, and x_m ($m = 1, 2, \dots, M$) represents the existing grid node. The area of the polygon where the node x_1 is located is the largest. According to the principle of space filling of the Voronoi tessellation method, a new grid node needs to be determined in the Voronoi cell where x_1 is located.

In Fig. 2, $T = \{t_1, t_n, \dots, t_N\}$ is a random, uniformly distributed Monte Carlo test point set. By filling enough test points in each Voronoi unit, the area of each irregular

polygon can be estimated. For each test point, (2) needs to be satisfied:

$$\|t_n - x_m\| \leq \|t_n - x_{m'}\|, m \neq m'. \quad (2)$$

That is, to determine the Monte Carlo test point set in each Voronoi unit, it is necessary to calculate the distance between the test point t_n and each node x_m , and then assign the test point to the nearest node x_m .

The Voronoi tessellation method completes the evaluation of the density of the global region, and in order to select data points according to the local characteristics of the model, the LOLA method needs to be used. The key point of LOLA is to complete the evaluation of local linear features by means of gradient estimation. The gradient g at node x_m needs to be estimated by fitting the hyperplane of x_m and its adjacent nodes. The determination of the hyperplane requires the use of the least squares method to ensure that the fitted hyperplane can pass through the node x_m :

$$\begin{pmatrix} x_{m_1}^{(1)} - x_m^{(1)} & x_{m_1}^{(2)} - x_m^{(2)} & \cdots & x_{m_1}^{(d)} - x_m^{(d)} \\ x_{m_2}^{(1)} - x_m^{(1)} & x_{m_2}^{(2)} - x_m^{(2)} & \cdots & x_{m_2}^{(d)} - x_m^{(d)} \\ \vdots & \vdots & \vdots & \vdots \\ x_{m_{2d}}^{(1)} - x_m^{(1)} & x_{m_{2d}}^{(2)} - x_m^{(2)} & \cdots & x_{m_{2d}}^{(d)} - x_m^{(d)} \end{pmatrix} \cdot \begin{pmatrix} g_m^{(1)} \\ g_m^{(2)} \\ \vdots \\ g_m^{(d)} \end{pmatrix} = \begin{pmatrix} f(x_{m_1}) \\ f(x_{m_2}) \\ \vdots \\ f(x_{m_{2d}}) \end{pmatrix}. \quad (3)$$

Among them, $x_{m_i} = (x_{m_i}^{(1)}, x_{m_i}^{(2)}, \dots, x_{m_i}^{(d)})$ ($i = 1, 2, \dots, 2d$) is the neighboring data point of x_m , $f(x_{m_i})$ is the model output response value corresponding to the neighboring data point x_{m_i} , d is the number of dimensions, and $g = (g_m^{(1)}, g_m^{(2)}, \dots, g_m^{(d)})$ is the gradient matrix of each dimension.

After solving the gradient matrix g , the nonlinearity near node x_m can be obtained by using

$$O(x_m) = \sum_{i=1}^{2d} |f(x_{m_i}) - (f(x_m) + g \cdot (x_{m_i} - x_m))|. \quad (4)$$

In this way, the global region division density evaluation and the local nonlinear feature evaluation are completed, and then the two metric parameters can be comprehensively evaluated by

$$S(x_m) = V(x_m) + \frac{O(x_m)}{\sum_{m=1}^M O(x_m)}. \quad (5)$$

$V(x_m)$ represents the size of the Voronoi cell area. Bring all existing data points into (5), calculate the value of $S(x_m)$, and sort it. The larger the value of $S(x_m)$, the less dense the grid in the field. It is necessary to add new sampling points to increase the division density. Repeat the above operations to meet the preset accuracy requirements.

C. Relative error

In order to better analyze the correctness and effectiveness of the two-stage plane adaptive sampling algorithm, the relative error should be calculated as follows: First, the traditional uniform sampling and the two-stage plane adaptive sampling method are used to obtain the NF samples; then the Kriging interpolation method is used to restore the electromagnetic field distribution of the entire NF plane, and the corresponding NF value at the same position is predicted; finally, compare the predicted value with the simulated data, solve the MAPE (Mean Absolute Percentage Error) obtained by these two sampling methods respectively, and compare the relative error produced between the two methods.

$$MAPE = \frac{1}{n} \sum_{i=1}^n \left| \frac{E_o - E_p}{E_o} \right| \times 100\%. \quad (6)$$

In this paper, the NF data studied are all electric field strength. Therefore, in (6), E_o represents the actual electric field strength value obtained by electromagnetic simulation, E_p represents the electric field strength value predicted by Kriging interpolation method, and n represents the number of prediction points.

IV. EXPERIMENTS AND ANALYSIS

In order to verify the correctness and effectiveness of the proposed method, we have studied two practical cases to verify the performance of the two-stage plane adaptive sampling algorithm. Both cases are modeled and simulated by ANSYS HFSS, and the simulation results are used as the actual NF values for comparison.

A. Dipole antenna model

The first case is dipole equivalent source model, the equivalent source model commonly used in engineering, which is a simplification of the current/magnetic current source model and widely used in the field of NF analysis. The half-wave dipole is an ideal conductor material with operating wavelength λ 100 mm, a total length 0.48λ , and a radius $\lambda/200$. The half-wave dipole antenna is fed by a lumped port excitation method, the port size is set to $0.24 \times (\lambda/100) \text{ mm}^2$, and the distance from the radiation boundary to the antenna is $\lambda/4$, as shown in Fig. 3.

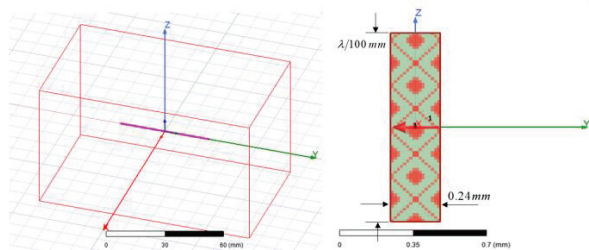


Fig. 3. (a) HFSS model of half-wave dipole antenna and (b) integrated port setting method.

According to the implementation principle of the proposed two-stage plane adaptive sampling algorithm, in the initial rough uniform sampling of the first stage, the size of the NF sampling surface is set to $66 \times 114 \text{ mm}^2$, the sampling interval is 2 mm, and the sampling height is 1 mm. Figure 4 shows the distribution of the transient electric field amplitude E of the half-wave dipole at the NF sampling plane, obtained by simulation.

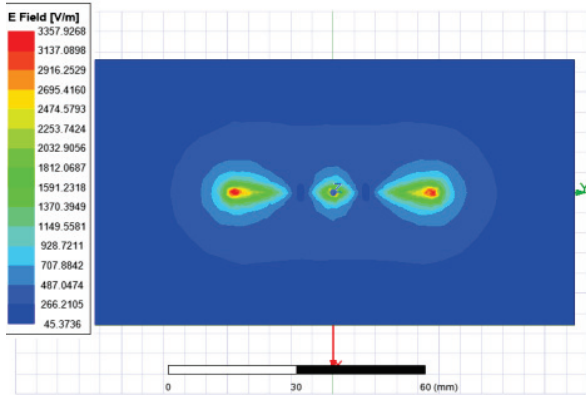


Fig. 4. Distribution diagram of the transient electric field amplitude E of the half-wave dipole antenna at the sampling plane.

It can be seen from Section II that the two-stage plane adaptive sampling algorithm is mainly divided into four steps. Figure 5 shows the effect diagram of the work in the four steps.

The two-stage planar adaptive sampling algorithm first performs an initial rough uniform sampling with a

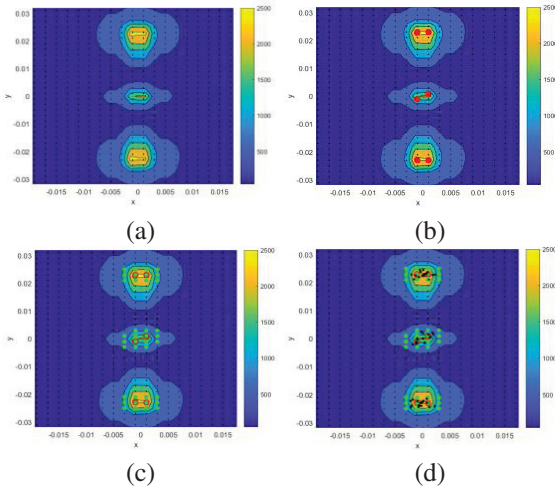


Fig. 5. Dipole antenna model: (a) Step 1: Initial rough uniform sampling, (b) Step 2: Determination of the central source point, (c) Step 3: Expansion and regularization of the refinement area, and (d) Step 4: Non-uniform sampling of the refinement area.

sampling interval of 2 mm, and these sampling points are uniformly distributed on the entire NF sampling plane, as shown in Fig. 5 (a); secondly, the region self-growth optimization algorithm is used to identify the central source point with sharp changes in the NF, as shown in the red point in Fig. 5 (b); thirdly, the refinement area is determined based on this source point, and the reasonable area expansion and regularization are carried out, as shown in Fig. 5 (c), where the green sampling points are the boundaries; then, the LOLA-Voronoi adaptive division method is used to conduct non-uniform sampling for the refinement area, and eight sampling points are preset for each refinement area to achieve the purpose of thinning, as shown in Fig. 5 (d); finally, the information of the sampling points obtained in the two stages is summarized, and the electromagnetic distribution of the NF plane is restored using Kriging interpolation method, and the relative errors of the traditional dense uniform sampling method and the two-stage plane adaptive sampling algorithm in restoring the NF situation are calculated. Figure 6 shows a comparison of the reconstructed electric field between the two methods.

It can be seen from Fig. 6 that the restored electric field distributions are well matched. After calculation, it can be seen that when the traditional dense uniform sampling method and the two-stage plane adaptive sampling method restore the NF, the relative error generated in the refinement area where the NF changes sharply is 0.0034. Meanwhile, the proposed sampling method reduces the required sampling points by 74.4% compared with the traditional uniform sampling method. Therefore, the

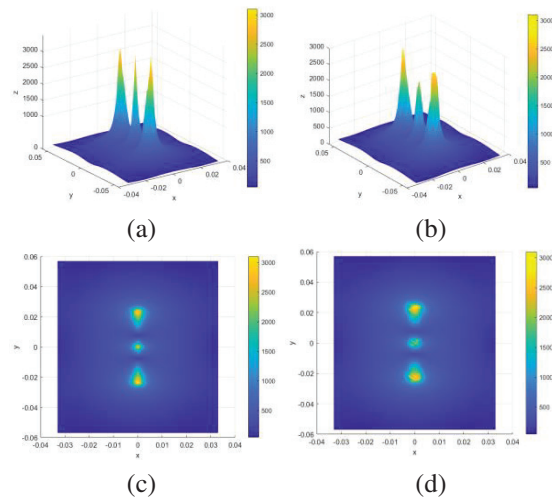


Fig. 6. Dipole antenna model: (a) 3D transient electric field distribution map under uniform sampling, (b) 3D transient electric field distribution map under adaptive sampling, (c) 2D transient electric field distribution map under uniform sampling, and (d) 2D transient electric field distribution map under adaptive sampling.

two-stage plane adaptive sampling method is accurate and effective in terms of restoration accuracy and the number of required sampling points.

B. BGA chip model

The second case is a chip with a BGA package structure with an operating frequency of 2.5 GHz. The package of the BGA chip consists of four layers, namely the top layer, the power supply Vdd_C1 layer, the power supply Vss_C1 layer, and the bottom layer. The package size is $9.40 \times 9.40 \text{ mm}^2$ and the thickness is 0.73152 mm.

Two differential pairs on the chip were selected for simulation analysis. At the same time, in order to speed up the simulation, we cut the chip without affecting the simulation results, and the size after cutting is $4.70 \times 9.40 \text{ mm}^2$, as shown in Fig. 7.

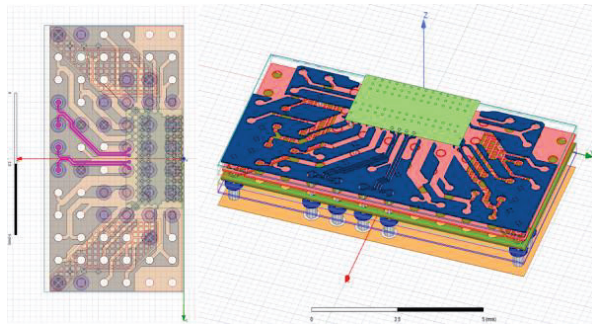


Fig. 7. Two differential pair models in a BGA chip from different perspectives.

The selected two pairs of differential data lines are RXDATA3+ and RXDATA3-, and RXDATA4+ and RXDATA4-, respectively, the operating frequency is 2.5 GHz, and the power feeding is the lumped port excitation.

The sampling surface size is set to $5 \times 9.6 \text{ mm}^2$, the sampling interval is 0.2 mm, and the NF sampling height is 0.3115 mm. The NF data is generated by ANSYS HFSS simulation. Figure 8 shows the distribution of the transient electric field amplitude of the BGA chip at the NF sampling surface. The effect diagram of the two-stage plane adaptive sampling algorithm with four steps is shown in Fig. 9.

The electromagnetic field distribution of the NF plane is restored by the two methods shown in Fig. 10, including a three-dimensional instantaneous electric field comparative analysis diagram and a two-dimensional plane instantaneous electric field comparative analysis diagram.

It can be seen from Fig. 10 that the restored electric field distributions are well matched. After calculation, it can be seen that when the two sampling methods restore

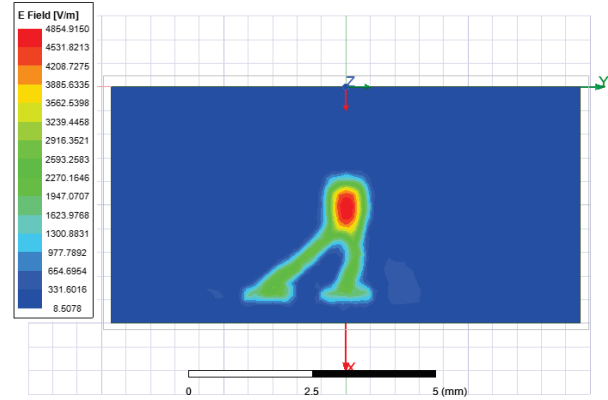


Fig. 8. Distribution diagram of transient electric field amplitude of BGA chip.

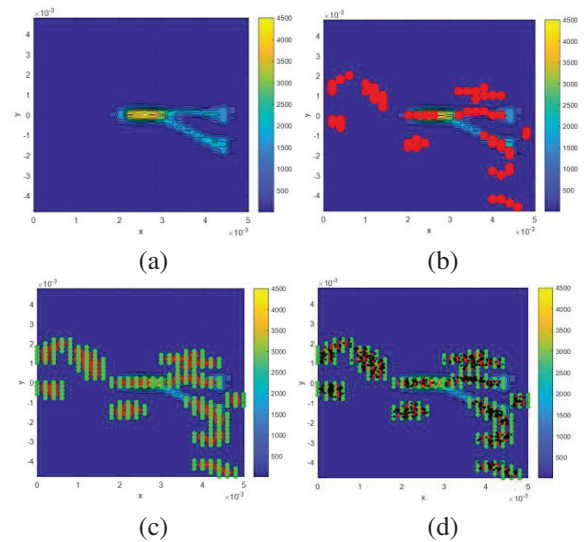


Fig. 9. BGA chip model: (a) Step 1: Initial rough uniform sampling, (b) Step 2: Determination of the central source point, (c) Step 3: Expansion and regularization of the refinement area, and (d) Step 4: Non-uniform sampling of the refinement area.

the NF, the relative error generated in the refinement area where the NF changes sharply is 0.0698. Meanwhile, the number of sampling points required by the two-stage plane adaptive sampling method is decreased by 74.2%. Therefore, compared with the traditional uniform sampling method, the proposed sampling method is more accurate and effective from the perspective of restoration accuracy and the number of required sampling points.

The number of NF samples required to use the two-stage planar adaptive sampling algorithm is smaller when the NF accuracy is similar. Compared with the traditional uniform sampling method, when the proposed sampling method samples the half-wave dipole module

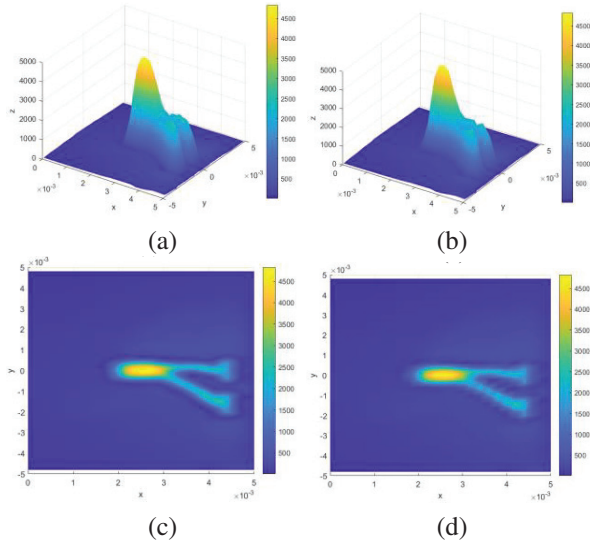


Fig. 10. BGA chip model: (a) 3D transient electric field distribution map under uniform sampling, (b) 3D transient electric field distribution map under adaptive sampling, (c) 2D transient electric field distribution map under uniform sampling, and (d) 2D transient electric field distribution map under adaptive sampling.

and the BGA chip module, the number of required NF samples is reduced by 74.4% and 74.2%, respectively. Therefore, the proposed sampling method can effectively reduce the number of required NF samples while ensuring the restoration accuracy.

V. CONCLUSION

In this paper, a two-stage plane adaptive NF scanning algorithm is proposed, which solves the problem of long acquisition time of NF data in the NF scanning process, and can efficiently image the radiation source in the high-speed integrated circuit board. Based on the region self-growth optimization algorithm and the Voronoi subdivision principle, the method significantly reduces the number of NF scanning points required to characterize the electromagnetic behavior of the DUT by means of uniform and non-uniform two-stage sampling, and reconstructs the NF electromagnetic distribution of the DUT with high resolution by means of Kriging interpolation.

By studying the specific performance of the new method in the application of NF scanning, this paper proves the correctness and effectiveness of the two-stage plane adaptive scanning algorithm in determining multiple strong radiation sources and accurately restoring the NF distribution of the DUT. The dominant advantage of the method proposed in this paper is to significantly reduce the number of NF samples by nearly 75% in near-field scanning. Therefore, it would

be widely applied in evaluating the EMC characteristics of integrated circuits, locating EMI sources, and efficiently completing the reconstruction of radiation sources.

REFERENCES

- [1] A. Taaghoul and T. Sarkar, "Near-field to near/far-field transformation for arbitrary near-field geometry, utilizing an equivalent magnetic current," *IEEE Trans. Electromagn. Compat.*, vol. 38, no. 3, pp. 536-542, 1996.
- [2] T. Sarkar and A. Taaghoul, "Near-field to near/far-field transformation for arbitrary near-field geometry utilizing an equivalent electric current and mom," *IEEE Trans. Antennas Propag.*, vol. 47, no. 3, pp. 566-573, 1999.
- [3] Y. Alvarez Lopez, F. Las-Heras Andres, M. R. Pino, and T. K. Sarkar, "An improved super-resolution source reconstruction method," *IEEE Trans. Instrum. Meas.*, vol. 58, no. 11, pp. 3855-3866, 2009.
- [4] P. Li and L. J. Jiang, "A rigorous approach for the radiated emission characterization based on the spherical magnetic field scanning," *IEEE Trans. Electromagn. Compat.*, vol. 56, no. 3, pp. 683-690, 2014.
- [5] H. Wang, V. Khilkevich, Y.-J. Zhang, and J. Fan, "Estimating radiofrequency interference to an antenna due to near-field coupling using decomposition method based on reciprocity," *IEEE Trans. Electromagn. Compat.*, vol. 55, no. 6, pp. 1125-1131, 2013.
- [6] J. Zhang and J. Fan, "Source reconstruction for IC radiated emissions based on magnitude-only near-field scanning," *IEEE Trans. Electromagn. Compat.*, vol. 59, no. 2, pp. 557-566, 2017.
- [7] W.-J. Zhao, E.-X. Liu, B. Wang, S.-P. Gao, and C. E. Png, "Differential evolutionary optimization of an equivalent dipole model for electromagnetic emission analysis," *IEEE Trans. Electromagn. Compat.*, vol. 60, no. 6, pp. 1635-1639, 2018.
- [8] Y.-F. Shu, X.-C. Wei, R. Yang, and E.-X. Liu, "An iterative approach for EMI source reconstruction based on phaseless and single-plane near-field scanning," *IEEE Trans. Electromagn. Compat.*, vol. 60, no. 4, pp. 937-944, 2018.
- [9] J.-C. Zhang, X. Wei, L. Ding, X.-K. Gao, and Z.-X. Xu, "An EM imaging method based on plane-wave spectrum and transmission line model," *IEEE Trans. Microw. Theory Tech.*, vol. 68, no. 10, pp. 4161-4168, 2020.
- [10] A. Tankielun, H. Garbe, and J. Werner, "Calibration of electric probes for post-processing of near-field scanning data," *Proc. IEEE Int. Symp.*

- Electromagn. Compat.*, vol. 1, pp. 119-124, Aug. 2006.
- [11] M. R. Ramzi, M. Abou-Khousa, and I. Prayudi, "Near-field microwave imaging using open-ended circular waveguide probes," *IEEE Sensors J.*, vol. 17, no. 8, pp. 2359-2366, 2017.
- [12] S. Jarrix, T. Dubois, R. Adam, P. Nouvel, B. Azais, and D. Gasquet, "Probe characterization for electromagnetic near-field studies," *IEEE Trans. Instrum. Meas.*, vol. 59, no. 2, pp. 292-300, 2010.
- [13] H. Weng, D. G. Beetner, and R. E. DuBroff, "Frequency-domain probe characterization and compensation using reciprocity," *IEEE Trans. Electromagn. Compat.*, vol. 53, no. 1, pp. 2-10, 2011.
- [14] D. Deschrijver, F. Vanhee, D. Pissort, and T. Dhaene, "Automated nearfield scanning algorithm for the EMC analysis of electronic devices," *IEEE Trans. Electromagn. Compat.*, vol. 54, no. 3, pp. 502-510, 2012.
- [15] P. Singh, D. Deschrijver, D. Pissort, and T. Dhaene, "Accurate hotspot localization by sampling the near-field pattern of electronic devices," *IEEE Trans. Electromagn. Compat.*, vol. 55, no. 6, pp. 1365-1368, 2013.
- [16] P. Singh, T. Claeys, G. A. E. Vandenbosch, and D. Pissort, "Automated line-based sequential sampling and modeling algorithm for EMC near-field scanning," *IEEE Trans. Electromagn. Compat.*, vol. 59, no. 2, pp. 704-709, 2017.
- [17] R. Brahimi, A. Kornaga, M. Bensetti, D. Baudry, Z. Riah, A. Louis, and B. Mazari, "Postprocessing of near-field measurement based on neural networks," *IEEE Trans. Instrum. Meas.*, vol. 60, no. 2, pp. 539-546, 2011.
- [18] Y.-R. Feng, X.-C. Wei, L. Ding, T.-H. Song, R. X.-K. Gao, "A hybrid Schatten p -norm and l_p -norm with plane wave expansion method for near-field transformation," *IEEE Trans. Electromagn. Compat.*, vol. 63, no. 6, pp. 2074-2081, 2021.
- [19] S. Tao, H. Zhao, and Z. D. Chen, "An adaptive sampling strategy based on region growing for near-field-based imaging of radiation sources," *IEEE Access*, vol. 9, pp. 9550-9556, 2021.
- [20] S. Serpaud, A. Boyer, S. Ben-Dhia, and F. Coccetti, "Fast and accurate near-field measurement method using sequential spatial adaptive sampling (SSAS) algorithm," *IEEE Trans. Electromagn. Compat.*, vol. 63, no. 3, pp. 858-869, 2021.
- [21] J.-R. Regue, M. Ribo, J.-M. Garrell, and A. Martin, "A genetic algorithm based method for source identification and far-field radiated emissions prediction from near-field measurements for PCB characterization," *IEEE Trans. Electromagn. Compat.*, vol. 43, no. 4, pp. 520-530, 2001.
- [22] W.-J. Zhao, B.-F. Wang, E.-X. Liu, H. B. Park, H. H. Park, E. Song, and E.-P. Li, "An effective and efficient approach for radiated emission prediction based on amplitude-only near-field measurements," *IEEE Trans. Electromagn. Compat.*, vol. 54, no. 5, pp. 1186-1189, 2012.
- [23] F.-P. Xiang, E.-P. Li, X.-C. Wei, and J.-M. Jin, "A particle swarm optimization-based approach for predicting maximum radiated emission from PCBs with dominant radiators," *IEEE Trans. Electromagn. Compat.*, vol. 57, no. 5, pp. 1197-1205, 2015.
- [24] J. A. Russer, N. Uddin, A. S. Awany, A. Thiede, and P. Russer, "Nearfield measurement of stochastic electromagnetic fields," *IEEE Electromagn. Compat. Mag.*, vol. 4, no. 3, pp. 79-85, 2015.
- [25] E. X. Liu, W. J. Zhao, B. F. Wang, and X. C. Wei, "Near-field scanning and its EMC applications," *Proc. Int. Symp. IEEE Electromagn. Compat.*, pp. 937-944, 2017.
- [26] H. P. Zhao, S. H. Tao, Z. Z. Chen, and J. Fan, "Sparse source model for prediction of radiations by transmission lines on a ground plane using a small number of near-field samples," *IEEE Antennas Wireless Propag. Lett.*, vol. 18, no. 1, pp. 103-107, Jan. 2019.
- [27] N. A. Abou-Khousa and A. Haryono, "Array of planar resonator probes for rapid near-field microwave imaging," *IEEE Trans. Instrum. Meas.*, vol. 69, no. 6, pp. 3838-3846, June 2020.
- [28] K. Crombecq, D. Gorissen, D. Deschrijver, and T. Dhaene, "A novel hybrid sequential design strategy for global surrogate modeling of computer experiments," *SIAM J. Sci. Comput.*, vol. 33, no. 4, pp. 1948-1974, Jan. 2011.
- [29] J. Tao, W. Tang, B. Li, S. Zhang, and R. Sun, "Efficient indoor signal propagation model based on LOLA-Voronoi adaptive meshing," *Applied Computational Electromagnetics (ACES) Society Journal*, vol. 35, no. 4, pp. 437-442, 2020.
- [30] S. Huang, Z. Peng, Z. Wang, X. Wang, and M. Li, "Infrared small target detection by density peaks searching and maximum-gray region growing," *IEEE Geosci. Remote Sens. Lett.*, vol. 16, no. 12, pp. 1919-1923, Dec. 2019.



Xiaoyong Liu received the bachelor's degree in radio technology and information system from Tsinghua University, Beijing, China, in 2002. He is currently working toward the doctor's degree in electronic science and technology from the Beijing University of Posts & Telecommunications, Beijing, China. His research interests include electromagnetic compatibility, testing and measurement, radio frequency spectrum technology.



Dan Shi (M'08) received the Ph.D. degree in electronic engineering from Beijing University of Posts & Telecommunications, Beijing, China, in 2008. She has been a professor in Beijing University of Posts & Telecommunications. Her interests include electromagnetic compatibility, electromagnetic environment, and electromagnetic computation.



Peng Zhang received the bachelor's degree in electronic engineering from Nanjing Institute of Technology, Nanjing, China, in 2020. He is currently working toward the master's degree in electronics and communication engineering from the Beijing University of Posts & Telecommunications, Beijing, China. His research interests include chip electromagnetic compatibility and reconstruction of emission sources.

Fast Coupling Iterative Algorithm for Media Rough Surface with Multiple Targets Below

Lilan Lei

School of Mathematics and Computer Science
Yichun University, Yichun, 336000, China
lilanlei0320@126.com

Abstract – This paper proposes a fast mutual coupling iteration algorithm for analyzing the composite electromagnetic scattering characteristics of a Gaussian rough surface with multiple targets below it. Firstly, an electromagnetic scattering model of Gaussian rough surface with multiple targets underneath is established. To improve the efficiency of electromagnetic scattering calculations, the (banded matrix iterative approach canonical grid - conjugate gradient method (BMIA/CAG-CMG) algorithm is used to calculate the surface scattering of the rough surface, while for the scattering of the targets, the traditional numerical algorithm moment of methods (MoM) is used for the calculation. Its main acceleration principle is to decompose the matrix into banded and Toeplitz matrices during the solution process, and then use fast Fourier transform (FFT) for fast solution based on their characteristics. By comparing the calculation results of this algorithm with those of the MoM algorithm, the correctness of this algorithm is verified. Several examples are studied, and the impact of different parameters on the surface current and composite scattering characteristics is discussed, which have important significance for deepening the understanding of scattering characteristics in complex electromagnetic environments.

Index Terms – BMIA/CAG-CMG, dielectric properties, electromagnetic scattering characteristics, mutual coupling iteration algorithm.

I. INTRODUCTION

The study of rough surfaces and composite electromagnetic scattering [1–6] is of significant importance in both military and civilian applications.

In military operations, researching the electromagnetic scattering properties of rough surfaces and targets below is critical to enhancing the ability to detect and track [7–8] enemy forces. As advanced technology and equipment increase the sensitivity of enemy reconnaissance and surveillance, studying methods for rough surface and target composite electromagnetic scattering

characteristics can help military units counter these threats and improve their anti-reconnaissance capabilities. Through observation and analysis of composite scattering characteristics, military units can quickly detect the presence and location of enemy forces, assisting in taking countermeasures promptly and effectively winning a battlefield advantage [9–13].

In civilian applications, scattering characteristics of rough surfaces and target composites can help people recognize and confirm underground mineral resources, fossil fuels, and other resources, accurately identifying exploitable locations. Additionally, studying these scattering characteristics can improve early warning and response capabilities toward changes in geological movements and natural disasters, making environmental monitoring and disaster warning [14–19] more effective.

Moreover, the study of rough surface and target composite electromagnetic scattering has penetrated the fields of space science and geophysics. The electromagnetic scattering characteristics of composite scenes are significant for detecting the earth's internal structure and mineral resources [20–25].

II. LITERATURE REVIEW

As computer technology and numerical algorithms [26–35] continue to evolve, more efficient methods for studying the electromagnetic scattering characteristics of complex composite scenes have emerged. Rapid algorithms, such as “fast multipole algorithm” and “extended boundary condition method,” have greatly improved the calculation efficiency and accuracy of electromagnetic scattering, thus becoming a hot research topic.

[26] studies the composite electromagnetic scattering characteristics of low-altitude targets above a complex valley rough surface using a hybrid SBR-EEC method. The method better simulates the complex structure of the valley surface and the target, providing a useful reference for practical applications. [27] proposes an improved FEM/MoM algorithm combining the MLFM algorithm for high-frequency electromagnetic

scattering of composite targets. This method better handles large-scale, three-dimensional target structures, improving the computational efficiency and accuracy of electromagnetic scattering. [28] studies the composite electromagnetic scattering characteristics of targets near the sea surface and proposes an efficient numerical algorithm. The method better simulates the complexity of the waves, target shape, and material. However, the algorithm's applicability is limited, and it cannot simulate scattering characteristics in other scenarios. [29] studies the electromagnetic scattering problem of targets above a rough surface and proposes an effective numerical method. The algorithm considers the roughness of the ground surface and the complexity of the target's shape and material. [30] proposes an improved FDTD algorithm to study the composite electromagnetic scattering problem of targets embedded below a 1D Weierstrass fractal land surface. The method better analyzes the complex scattering characteristics of targets and can be used to analyze more complex target structures. [31] proposes a fast high-order algorithm to solve the problem of high wave number electromagnetic scattering from a finite array of cavities under TE incidence. The method better handles the local characteristics of targets, improving computation efficiency and accuracy. [32] proposes a fast parallel FDFD algorithm to solve the electromagnetic scattering problem. The method better handles the complex shape and material of the target. [33] proposes a method based on the discontinuous Galerkin surface integral equation to handle large-scale electromagnetic scattering problems. The method better handles the target's complex structure, improving computation efficiency and accuracy. [34] studies the electromagnetic scattering problem of dielectric targets and proposes a numerical algorithm to directly solve the volume integral equation for targets with negative permittivity. The method better handles the complex scattering characteristics of targets and improves computation efficiency and accuracy. [35] proposes a method based on the pre-corrected fast Fourier transform (FFT) algorithm to analyze the spectrum characteristics of electromagnetic scattering targets. The method more accurately and quickly calculates the target's broadband scattering characteristics. Areas for improvement may include expanding the algorithm's applicability and optimizing implementation to improve computation efficiency and accuracy.

Although the above algorithms solve composite scattering problems under specific conditions, their range of applicability is limited. Some algorithms have high computational accuracy, but their complexity and computation speed limit their practical application in computational scenarios. As a supplement, this article proposes an accelerated algorithm based on

mutual iterative coupling to improve the algorithm's applicability and computation efficiency in practical applications.

This paper aims to explore the composite electromagnetic scattering characteristics between a dielectric Gaussian rough surface and multiple targets below it, and a fast mutual coupling iterative algorithm is proposed to achieve this goal. Based on this, the influence of the dielectric properties (rough surface and targets) and the distance between the targets on the surface current and composite scattering characteristics were studied, and then the mechanism of mutual influence between two targets was revealed, showing that their coupling effects cannot be ignored. The research results provide new insights and ideas for electromagnetic scattering theory and offer useful references for the application of electromagnetic scattering problems in related fields.

III. ROUGH SURFACE GEOMETRY MODELING

In the process of establishing a ground geometry model, we adopted a method that combines Monte Carlo method with Gaussian spectral function [36]. This method can generate a series of random numbers that follow a normal distribution function, and L represents the length of the rough surface. Afterwards, we used discrete Fourier transform (DFT) [37] to process the rough surface, and through this processing method, we can represent the height fluctuations of the surface as $f(x)$:

$$z = f(x) = \frac{1}{L} \sum_{n=-N/2+1}^{N/2} b_n e^{-jk_n x}, \quad (1)$$

where b_n is

$$b_n = \sqrt{2\pi LW(k_n)} \begin{cases} (N(0,1) + jN(0,1)) / \sqrt{2} & n = 1, 2, \dots, N/2 - 1 \\ N(0,1) & n = 0, N/2 \\ b_{-n}^* & n < 0. \end{cases} \quad (2)$$

The following formulas are satisfied by K_{xm} , K_{yn} , L_x , and L_y in the above equation:

$$K_{xm} = \frac{2\pi m}{L_x}, \quad K_{yn} = \frac{2\pi n}{L_y}. \quad (3)$$

In the equation, $k_n = 2\pi n/L$ represents the discrete points of the spatial spectrum, b_{-n}^* represents the complex conjugate, and $W(k_n)$ represents the spectral function. The first and second derivatives of the rough surface height function are represented as $f'(x)$ and $f''(x)$, respectively:

$$f'(x) = \frac{1}{L} \sum_{n=-N/2+1}^{N/2} (-jk_n) b_n e^{-jk_n x}, \quad (4)$$

$$f''(x) = \frac{1}{L} \sum_{n=-N/2+1}^{N/2} (-jk_n)^2 b_n e^{-jk_n x}. \quad (5)$$

The distribution characteristics of the spectral function $W(k_n)$ determine the statistical properties of the rough surface, which is of great significance in establishing ground models and other related fields. Among various spectral functions, the Gaussian spectral function is the most commonly used and basic one, which is widely used in establishing ground models and other related research fields. By appropriately adjusting its parameters, we can control the various characteristics and features of the generated ground model, providing accurate and reliable data and information for practical production and research fields. The expression of the Gaussian spectral function is

$$W(k) = \frac{h^2 l}{2\sqrt{\pi}} \exp(-k^2 l^2 / 4). \quad (6)$$

The Gaussian spectral function is a commonly used mathematical model for describing the surface morphology of rough surfaces, which can be used to study and analyze the characteristics and properties of various rough surfaces. The function's parameters include the root-mean-square height h and the correlation length l . The spectral density function of the Gaussian rough surface function is a Gaussian distribution function, and its shape determines the roughness characteristics of the surface. For a given Gaussian rough surface function, the degree and complexity of surface fluctuations can be controlled by changing the values of the root-mean-square height h and the correlation length l . When h is constant, a smaller correlation length will lead to a steeper and more chaotic surface, making the surface rougher. When l is constant, increasing h will increase the degree of surface fluctuations, making the surface rougher.

The Monte Carlo method is generally used to randomly simulate a Gaussian rough surface with specified parameters. By changing the parameter values, Gaussian rough surfaces of different shapes can be obtained. Figure 1 shows the undulation of Gaussian

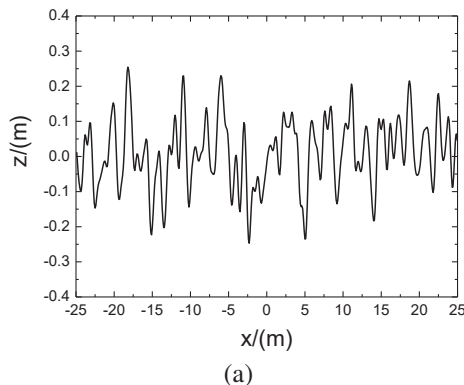


Fig. 1. Continued

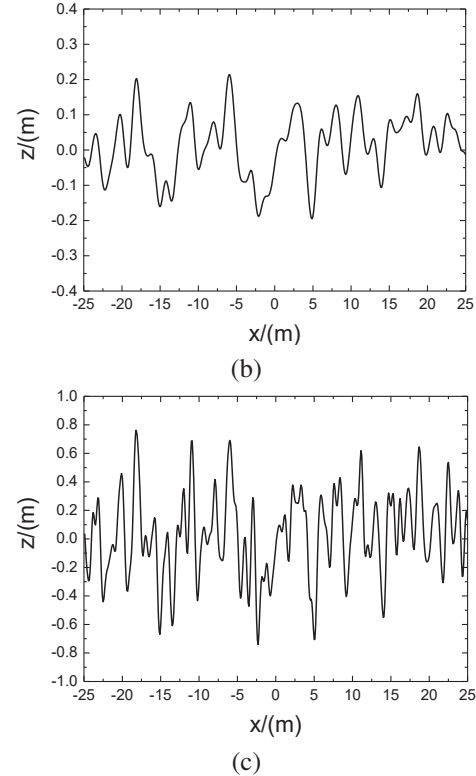


Fig. 1. Geometric model of rough surface: (a) $h = 0.1$ m, $l = 0.5$ m, (b) $h = 0.1$ m, $l = 1.0$ m, (c) $h = 0.3$ m, $l = 0.5$ m, and (d) $h = 0.1$ m, $l = 1.0$ m.

rough surfaces generated under different parameters. It can be seen that a smaller correlation length and a larger root-mean-square height will lead to a steeper and more complex surface, making the surface rougher.

IV. ALGORITHM MODEL AND VALIDATION ANALYSIS

A. Coupled iterative integral equation

In reality, rough surfaces and targets do not exist independently but exist in the same space and interact with each other. Similarly, the electromagnetic scattering coupling phenomenon between rough surfaces and targets is the main factor affecting their composite electromagnetic scattering characteristics. Therefore, we have established an integral equation coupling rough surfaces and targets and solved it iteratively until convergence. The composite scattering schematic is shown in Fig. 2.

Space 1 is the atmosphere, and its dielectric constant and magnetic permeability are ϵ_1 , and μ_1 . Space 2 is the dielectric rough surface, and its dielectric constant and magnetic permeability are ϵ_2 , and μ_2 . The depth of target 1 is H_1 , the depth of target 2 is H_2 , and the distance between them is L_{12} . The dielectric constant and magnetic permeability are $\epsilon_{01,02}$ and $\mu_{01,02}$, respectively.

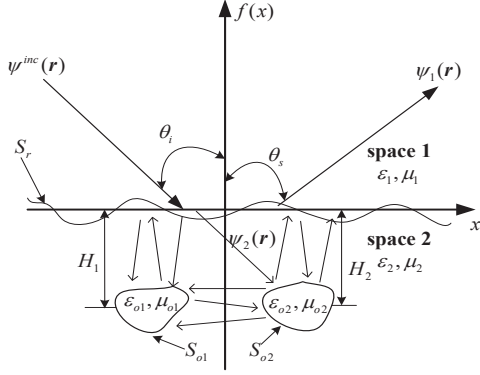


Fig. 2. Composite scattering model for rough surfaces and targets.

If the rough surface and the target are treated as a whole, the surface integral equation when the conical incident wave is irradiated onto the scattering model is

$$\begin{aligned} \frac{1}{2} \psi_1(\mathbf{r}) &= \psi^{inc}(\mathbf{r}) \\ &+ \int_{S_r} \left[\psi_1(\mathbf{r}') \frac{\partial g_1(\mathbf{r}, \mathbf{r}')}{\partial n'} - g_1(\mathbf{r}, \mathbf{r}') \frac{\partial \psi_1(\mathbf{r}')}{\partial n'} \right] ds' \quad (\mathbf{r} \in S_r), \end{aligned} \quad (7)$$

$$\begin{aligned} \frac{1}{2} \psi_2(\mathbf{r}) &= - \int_{S_r} \left[\psi_2(\mathbf{r}') \frac{\partial g_2(\mathbf{r}, \mathbf{r}')}{\partial n'} - g_2(\mathbf{r}, \mathbf{r}') \frac{\partial \psi_2(\mathbf{r}')}{\partial n'} \right] ds' \\ &+ \int_{S_{o1}} \left[\psi_2(\mathbf{r}') \frac{\partial g_2(\mathbf{r}, \mathbf{r}')}{\partial n'} - g_2(\mathbf{r}, \mathbf{r}') \frac{\partial \psi_2(\mathbf{r}')}{\partial n'} \right] ds' \\ &+ \int_{S_{o2}} \left[\psi_2(\mathbf{r}') \frac{\partial g_2(\mathbf{r}, \mathbf{r}')}{\partial n'} - g_2(\mathbf{r}, \mathbf{r}') \frac{\partial \psi_2(\mathbf{r}')}{\partial n'} \right] ds' \\ &(\mathbf{r} \in S_r \text{ or } \mathbf{r} \in S_{o1} \text{ or } \mathbf{r} \in S_{o2}), \end{aligned} \quad (8)$$

$$\begin{aligned} \frac{1}{2} \psi_{o1}(\mathbf{r}) &= - \int_{S_{o1}} \left[\psi_{o1}(\mathbf{r}') \frac{\partial g_{o1}(\mathbf{r}, \mathbf{r}')}{\partial n'} - g_{o1}(\mathbf{r}, \mathbf{r}') \frac{\partial \psi_{o1}(\mathbf{r}')}{\partial n'} \right] ds' \\ &(\mathbf{r} \in S_{o1}), \end{aligned} \quad (9)$$

$$\begin{aligned} \frac{1}{2} \psi_{o2}(\mathbf{r}) &= - \int_{S_{o2}} \left[\psi_{o2}(\mathbf{r}') \frac{\partial g_{o2}(\mathbf{r}, \mathbf{r}')}{\partial n'} - g_{o2}(\mathbf{r}, \mathbf{r}') \frac{\partial \psi_{o2}(\mathbf{r}')}{\partial n'} \right] ds' \\ &(\mathbf{r} \in S_{o2}), \end{aligned} \quad (10)$$

where $\psi_{1,2}$ denotes the wave functions in medium 1 and medium 2, respectively, and $\psi_{o1,o2}$ denotes the wave function in medium target 1 and medium target 2, respectively. The Green's function in the medium $g_{1,2}(\mathbf{r}, \mathbf{r}') = (j/4) H_0^{(1)}(k_{1,2} |\mathbf{r} - \mathbf{r}'|)$, and the Green's function in the target $g_{o1,o2}(\mathbf{r}, \mathbf{r}') = (j/4) H_0^{(1)}(k_{o1,2} |\mathbf{r} - \mathbf{r}'|)$.

The boundary conditions for the above system of equations are

$$\begin{cases} \psi_2(\mathbf{r}) = \psi_1(\mathbf{r}) \\ \frac{\partial \psi_2(\mathbf{r})}{\partial n} = \rho_s \frac{\partial \psi_1(\mathbf{r})}{\partial n} \end{cases} \quad (\mathbf{r} \in S_r), \quad (11)$$

$$\begin{cases} \psi_{o2}(\mathbf{r}) = \psi_2(\mathbf{r}) \\ \frac{\partial \psi_{o2}(\mathbf{r})}{\partial n} = \rho_{o2} \frac{\partial \psi_2(\mathbf{r})}{\partial n} \end{cases} \quad (\mathbf{r} \in S_{o2}), \quad (12)$$

$$\begin{cases} \psi_{o1}(\mathbf{r}) = \psi_2(\mathbf{r}) \\ \frac{\partial \psi_{o1}(\mathbf{r})}{\partial n} = \rho_{o1} \frac{\partial \psi_2(\mathbf{r})}{\partial n} \end{cases} \quad (\mathbf{r} \in S_{o1}). \quad (13)$$

Then the MOM is used to discretize the above integral equation, so the matrix equation can be obtained as follows:

$$\begin{bmatrix} \mathbf{A} & \mathbf{B} & \mathbf{0} & \mathbf{0} & \mathbf{0} & \mathbf{0} \\ \rho_s \mathbf{C} & \mathbf{D} & \mathbf{E} & \mathbf{F} & \mathbf{G} & \mathbf{H} \\ \rho_s \mathbf{I} & \mathbf{J} & \mathbf{K} & \mathbf{L} & \mathbf{M} & \mathbf{N} \\ \mathbf{0} & \mathbf{0} & \rho_{o1} \mathbf{P} & \mathbf{Q} & \mathbf{0} & \mathbf{0} \\ \rho_s \mathbf{R} & \mathbf{S} & \mathbf{T} & \mathbf{U} & \mathbf{V} & \mathbf{W} \\ \mathbf{0} & \mathbf{0} & \mathbf{0} & \mathbf{0} & \rho_{o2} \mathbf{X} & \mathbf{Y} \end{bmatrix} \begin{bmatrix} \mathbf{I}_1 = \partial \psi_1(\mathbf{r}) / \partial n|_{\mathbf{r} \in S_r} \\ \mathbf{I}_2 = \psi_1(\mathbf{r})|_{\mathbf{r} \in S_r} \\ \mathbf{I}_3 = \partial \psi_2(\mathbf{r}) / \partial n|_{\mathbf{r} \in S_{o1}} \\ \mathbf{I}_4 = \psi_2(\mathbf{r})|_{\mathbf{r} \in S_{o1}} \\ \mathbf{I}_5 = \partial \psi_2(\mathbf{r}) / \partial n|_{\mathbf{r} \in S_{o2}} \\ \mathbf{I}_6 = \psi_2(\mathbf{r})|_{\mathbf{r} \in S_{o2}} \end{bmatrix} = \begin{bmatrix} \psi^{inc} \\ \mathbf{0} \\ \mathbf{0} \\ \mathbf{0} \\ \mathbf{0} \\ \mathbf{0} \end{bmatrix}, \quad (14)$$

where ψ^{inc} denotes the conical incident wave on the rough surface. $\mathbf{A}, \mathbf{B}, \mathbf{C}, \mathbf{D}$ are the rough surface matrices, $\mathbf{K}, \mathbf{L}, \mathbf{P}, \mathbf{Q}$ are the target 1 matrices, $\mathbf{V}, \mathbf{W}, \mathbf{X}, \mathbf{Y}$ are the target 2 matrices, \mathbf{E}, \mathbf{F} are the scattering contributions from target 1 to the rough surface, \mathbf{G}, \mathbf{H} are the scattering contributions from target 2 to the rough surface, \mathbf{I}, \mathbf{J} are the scattering contributions from the rough surface to the target 1, \mathbf{R}, \mathbf{S} are the scattering contributions from the rough surface to the target 2, \mathbf{M}, \mathbf{N} are the scattering contributions from target 2 to the target 1, and \mathbf{T}, \mathbf{U} are the scattering contributions from target 1 to target 2. For the specific values of each parameter, please refer to the literature [38], which is not repeated here to save space.

Considering the coupling effect between the rough surface and the targets, as well as between the targets, the coupled iterative solution of the above equations is required, and the set of iterative equations are

$$\begin{aligned} \frac{1}{2} I_4^{(i)}(\mathbf{r}) &- \int_{S_{o1}} \left[I_4^{(i)}(\mathbf{r}') \frac{\partial g_2(\mathbf{r}, \mathbf{r}')}{\partial n'} - g_2(\mathbf{r}, \mathbf{r}') I_3^{(i)}(\mathbf{r}') \right] ds' \\ &= - \int_{S_r} \left[I_2^{(i-1)}(\mathbf{r}') \frac{\partial g_2(\mathbf{r}, \mathbf{r}')}{\partial n'} - \rho_s g_2(\mathbf{r}, \mathbf{r}') I_1^{(i-1)}(\mathbf{r}') \right] ds' \\ &+ \int_{S_{o2}} \left[I_6^{(i-1)}(\mathbf{r}') \frac{\partial g_2(\mathbf{r}, \mathbf{r}')}{\partial n'} - g_2(\mathbf{r}, \mathbf{r}') I_5^{(i-1)}(\mathbf{r}') \right] ds' \\ &(\mathbf{r} \in S_{o1}), \end{aligned} \quad (15)$$

$$\begin{aligned} \frac{1}{2} I_4^{(i)}(\mathbf{r}) &= - \int_{S_{o1}} \left[I_4^{(i)}(\mathbf{r}') \frac{\partial g_{o1}(\mathbf{r}, \mathbf{r}')}{\partial n'} - \rho_{o1} g_{o1}(\mathbf{r}, \mathbf{r}') I_3^{(i)}(\mathbf{r}') \right] ds' \\ &(\mathbf{r} \in S_{o1}), \end{aligned} \quad (16)$$

$$\begin{aligned} \frac{1}{2} I_6^{(i)}(\mathbf{r}) &- \int_{S_{o2}} \left[I_6^{(i)}(\mathbf{r}') \frac{\partial g_2(\mathbf{r}, \mathbf{r}')}{\partial n'} - g_2(\mathbf{r}, \mathbf{r}') I_5^{(i)}(\mathbf{r}') \right] ds' \\ &= - \int_{S_r} \left[I_2^{(i-1)}(\mathbf{r}') \frac{\partial g_2(\mathbf{r}, \mathbf{r}')}{\partial n'} - \rho_s g_2(\mathbf{r}, \mathbf{r}') I_1^{(i-1)}(\mathbf{r}') \right] ds' \\ &+ \int_{S_{o1}} \left[I_4^{(i-1)}(\mathbf{r}') \frac{\partial g_2(\mathbf{r}, \mathbf{r}')}{\partial n'} - g_2(\mathbf{r}, \mathbf{r}') I_3^{(i-1)}(\mathbf{r}') \right] ds' \\ &(\mathbf{r} \in S_{o2}), \end{aligned} \quad (17)$$

$$\begin{aligned} \frac{1}{2} I_6^{(i)}(\mathbf{r}) &= - \int_{S_{o2}} \left[I_6^{(i)}(\mathbf{r}') \frac{\partial g_{o2}(\mathbf{r}, \mathbf{r}')}{\partial n'} - \rho_{o2} g_{o2}(\mathbf{r}, \mathbf{r}') I_5^{(i)}(\mathbf{r}') \right] ds' \\ &(\mathbf{r} \in S_{o2}). \end{aligned} \quad (18)$$

$$\begin{aligned} \frac{1}{2} I_2^{(i)}(\mathbf{r}) &- \int_{S_r} \left[I_2^{(i)}(\mathbf{r}') \frac{\partial g_1(\mathbf{r}, \mathbf{r}')}{\partial n'} - g_1(\mathbf{r}, \mathbf{r}') I_1^{(i)}(\mathbf{r}') \right] ds' = \psi^{inc}(\mathbf{r}) \\ &(\mathbf{r} \in S_r), \end{aligned} \quad (19)$$

$$\begin{aligned}
& \frac{1}{2} I_2^{(i)}(\mathbf{r}) + \int_{S_r} \left[I_2^{(i)}(\mathbf{r}') \frac{\partial g_2(\mathbf{r}, \mathbf{r}')}{\partial n'} - \rho_s g_2(\mathbf{r}, \mathbf{r}') I_1^{(i)}(\mathbf{r}') \right] ds' \\
& = \int_{S_{o1}} \left[I_4^{(i-1)}(\mathbf{r}') \frac{\partial g_2(\mathbf{r}, \mathbf{r}')}{\partial n'} - g_2(\mathbf{r}, \mathbf{r}') I_3^{(i-1)}(\mathbf{r}') \right] ds' \\
& + \int_{S_{o2}} \left[I_6^{(i-1)}(\mathbf{r}') \frac{\partial g_2(\mathbf{r}, \mathbf{r}')}{\partial n'} - g_2(\mathbf{r}, \mathbf{r}') I_5^{(i-1)}(\mathbf{r}') \right] ds' \\
& (\mathbf{r} \in S_r), \tag{20}
\end{aligned}$$

I_3 is used as a criterion to determine whether the equation converges or not, and the convergence condition is

$$\sqrt{\left\| \frac{I_3^{(i+1)} - I_3^{(i)}}{I_3^{(i)}} \right\|} \times 100\% < \sigma. \tag{21}$$

If the above equation is solved directly, too many unknowns will lead to low solution efficiency, which is unacceptable in practical applications, so a suitable algorithm needs to be used to accelerate the solution process.

The core of the solution of the banded matrix iterative approach canonical grid - conjugate gradient (BMIA/CAG-CMG) method is to decompose the original matrix equation into near-field matrix and far-field matrix by the strong/weak correlation distances, the original matrix is decomposed into matrices with Band and Toeplitz characteristics, and then CMG is used to solve the matrix equations, and in the iterative process, the matrix vector product is calculated quickly by using the FFT, thus speeding up the computation. The next section focuses on the BMIA/CAG-CMG algorithm.

B. Banded matrix iterative approach canonical grid - conjugate gradient method

Let the distance between the field point and the source point on the rough surface be $x_d = |x - x'|$ and the strong/weak correlation distance be r_d , so the surface integral equation for the rough surface can be decomposed into a strong acting region and a weak acting region as follows:

$$\begin{aligned}
& \frac{1}{2} \psi(r') - \int_{x_d < r_d} \left[\psi(\mathbf{r}) \frac{\partial g_0(r, r')}{\partial n'} - g_0(r, r') \frac{\partial \psi(\mathbf{r})}{\partial n'} \right] ds \\
& = \psi_{inc}(r') + \int_{x_d > r_d} \left[\psi(\mathbf{r}) \frac{\partial g_0(r, r')}{\partial n'} - g_0(r, r') \frac{\partial \psi(\mathbf{r})}{\partial n'} \right] ds'. \tag{22}
\end{aligned}$$

$$\frac{1}{2} \psi_1(r') + \int_{x_d < r_d} \left[\psi_1(\mathbf{r}) \frac{\partial g_1(r, r')}{\partial n'} - g_1(r, r') \frac{\partial \psi_1(\mathbf{r})}{\partial n'} \right] ds' = 0. \tag{23}$$

The left parts of the above equations are the strong correlation matrix(band matrix) and the right parts are the weak correlation matrix. Therefore, according to the BMIA/CAG algorithm, the above set of equations can be transformed into the strong/weak correlation matrix equations as follows:

$$\begin{aligned}
& \sum_{n=1}^{N_{dg}} Z_{0u}^{(s)} u_n + \sum_{n=1}^{N_{dg}} Z_{0\psi}^{(s)} \psi_n = \psi_{inc}(x_m) - \sum_{n=1}^{N_{dg}} Z_{0u}^{(w)} u_n + \sum_{n=1}^{N_{dg}} Z_{0\psi}^{(w)} \psi_n \tag{24} \\
& \sum_{n=1}^{N_{dg}} Z_{1u}^{(s)} u_n + \sum_{n=1}^{N_{dg}} Z_{1\psi}^{(s)} \psi_n = 0, \tag{25}
\end{aligned}$$

where $Z_{0u}^{(s)}, Z_{0u}^{(w)}, Z_{0\psi}^{(s)}, Z_{0\psi}^{(w)}, Z_{1u}^{(s)}$, and $Z_{1\psi}^{(w)}$ denote the strong and weak matrices of the free space and medium space, respectively.

For the region of $x_d > r_d$, that belongs to the weak correlation matrix calculation region, which is very computationally intensive, and if calculated directly will greatly reduce the computational efficiency. Therefore, the weak correlation matrix is considered to be processed by CAG, and then the FFT can be used for fast calculation, so that:

$$Z_0^{(w)} = Z_{0u}^{(w)(0)} + Z_{0\psi}^{(w)(0)} + \left(Z_{0u}^{(w)} + Z_{0\psi}^{(w)} - Z_{0u}^{(w)(0)} - Z_{0\psi}^{(w)(0)} \right). \tag{26}$$

The expression of the strong and weak correlation matrix equations become

$$\begin{aligned}
& \left[Z_{0u}^{(s)} + Z_{0u}^{(w)(0)} \right] u + \left[Z_{0\psi}^{(s)} + Z_{0\psi}^{(w)(0)} \right] \psi \\
& = \psi_{inc} - \left[Z_{0u}^{(w)} - Z_{0u}^{(w)(0)} \right] u - \left[Z_{0\psi}^{(w)} - Z_{0\psi}^{(w)(0)} \right] \psi, \tag{27}
\end{aligned}$$

$$Z_{1u}^{(s)} u + Z_{1\psi}^{(s)} \psi = 0. \tag{28}$$

The above matrix can be solved by the iterative method, whose n -th order iterative equation is

$$Z_u^{(0)} u^{(n)} + Z_\psi^{(0)} \psi^{(n)} = b^{(n)}, \tag{29}$$

$$Z_{1u}^{(s)} u^{(n)} + Z_{1\psi}^{(s)} \psi^{(n)} = 0, \tag{30}$$

$$\begin{aligned}
b^{(n)} & = \psi_{inc} - \left[Z_{0u}^{(w)} - Z_{0u}^{(w)(0)} \right] u^{(n-1)} \\
& - \left[Z_{0\psi}^{(w)} - Z_{0\psi}^{(w)(0)} \right] \psi^{(n-1)}. \tag{31}
\end{aligned}$$

Its initial value is:

$$Z_u^{(0)} u^{(0)} + Z_\psi^{(0)} \psi^{(0)} = \psi_{inc}, \tag{32}$$

$$Z_{1u}^{(s)} u^{(0)} + Z_{1\psi}^{(s)} \psi^{(0)} = 0. \tag{33}$$

The iterative calculation ends when $\sqrt{\left\| \frac{b^{(n)}}{\psi_{inc}} \right\|} \times 100\% < \sigma$.

To handle the weakly correlated matrices in the iterative equation, the CAG method is required due to the large computational load. The method expands the weak matrix to Taylor series along the x -axis and represents the product of the weak matrix with vector as a product of several Toeplitz matrices and a vector. Then, the FFT algorithm is utilized for the quick computation of the matrix-vector product. This process allows us to effectively calculate weakly correlated matrices and avoid the issue of excessive computational load. The specific calculation process is as follows.

The elements y_m of each row in the weak correlation matrix can be expressed as

$$y_m = \left\{ \left(Z_{0u}^{(w)} - Z_0^{(w)(0)} \right) u_n \right\}_m. \tag{34}$$

Its Taylor series expansion takes the form of

$$\begin{aligned}
y_m & = \sum_{n=1}^{N_{dg}} \left[\frac{j}{4} H_0^{(1)} \left(k_0 \sqrt{x_d^2 + z_d^2} \right) - \frac{j}{4} H_0^{(1)} \left(k_0 x_d \right) \right] \\
u_n & = \sum_{n=1}^{N_{dg}} \sum_{l=1}^{N_r} a_l(x_d) \left(\frac{z_d^2}{x_d^2} \right)^l u_n, \tag{35}
\end{aligned}$$

where $a_l(x_d)$ denotes the l -th coefficient of the Taylor series expansion, N_r is the total number of terms of the Taylor series expansion, and $z_d = |f(x_m) - f(x_n)|$. Its first three coefficients are

$$a_1(x_d) = -\frac{j}{4} H_1^{(1)}(k_0 x_d) \frac{k x_d}{2}, \quad (36)$$

$$a_2(x_d) = -\frac{j}{4} \frac{k^2 x_d^2}{8} H_0^{(1)}(k_0 x_d) + \frac{j}{4} \frac{k_0 x_d}{4} H_1^{(1)}(k_0 x_d), \quad (37)$$

$$a_3(x_d) = -\frac{j}{4} \frac{k_0^2 x_d^2}{12} H_0^{(1)}(k_0 x_d) + \frac{j}{4} \frac{k_0^3 x_d^3}{48} H_1^{(1)}(k_0 x_d) - \frac{j}{4} \frac{k_0 x_d}{6} H_1^{(1)}(k_0 x_d). \quad (38)$$

It can be observed from the formula that when $m = 1, 2, \dots, N_{dg}$, each term in y is equivalent to the product of a Toeplitz matrix and a column vector, which makes it suitable for fast computation using FFT.

C. Validation of algorithm

The correctness of the algorithm proposed in this article needs to be verified before carrying out example calculations. We take an infinitely long cylindrical target with radius $R = 5\lambda$ located beneath the rough medium at point $H = 10\lambda$ as an example and analyze the composite electromagnetic scattering problem using two different methods, namely the BMIA/CAG-CMG-MoM method and the MoM method. We present the target surface current distribution obtained using different methods in Fig. 3, and their composite scattering coefficients are

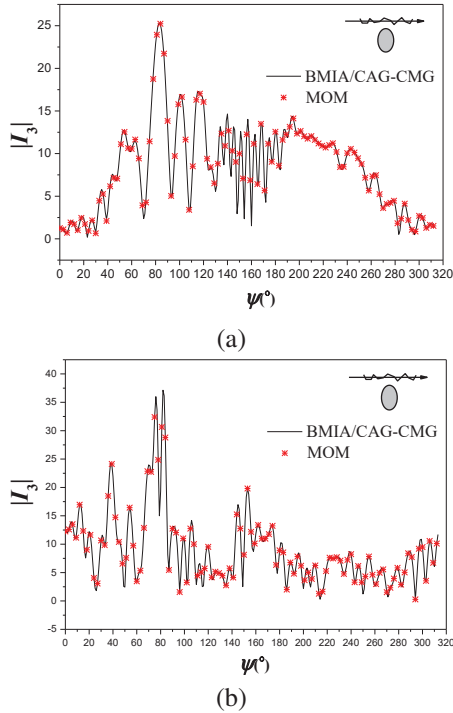


Fig. 3. Target surface current: (a) TE incident wave and (b) TM incident wave.

calculated and plotted in Fig. 4. Considering practical situations, we also introduce an incident wave with an incident angle of $\theta_i = 30^\circ$ and select different parameter settings, including rough surface length $L = 90\lambda$, root mean square height $h = 0.5\lambda$, correlation length $l = 4.0\lambda$, and incident wave frequency $f = 1.2\text{GHz}$. By comparing the results of the two methods, we find that they are consistent, indicating that the algorithm proposed in this article is correct. In addition, the time consumed by the two methods is listed in Table 1, which visually demonstrates the significant advantage of the proposed method in computational efficiency.

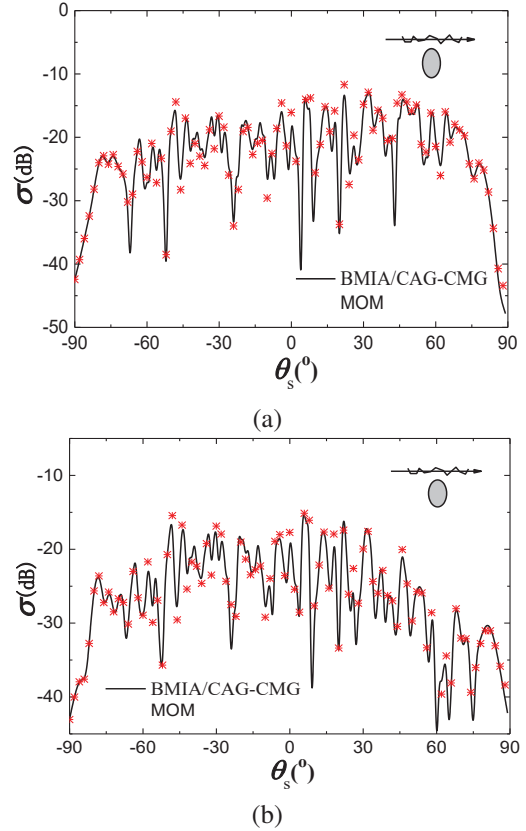


Fig. 4. Composite scattering coefficients: (a) TE incident wave and (b) TM incident wave.

Table 1: Time consumption comparison

Method	BMIA/CAG-CMG	MoM
Time	279 s	3721 s

BMIA/CAG-CMG is more than thirteen times faster than MoM

V. CALCULATION RESULTS AND ANALYSIS

In this section, we have carried out detailed studies and analyses on several computational examples

based on the proposed BMIA/CAG-CMG-MoM mutual coupling iteration algorithm. By simulating these examples, we have focused on the influence of the target on the scattering field of the rough surface when the relative permittivity of the rough surface, the distance between the target and the rough surface, the spacing between two targets, and the dielectric constant of the target change. The simulation results show that the proposed algorithm has good stability and computational accuracy when dealing with the above situations, and it has good reference value for studying the electromagnetic scattering characteristics of targets in complex backgrounds. At the same time, these analysis results provide valuable insights for further optimization and improvement of the BMIA/CAG-CMG-MoM mutual coupling iterative algorithm and may have guiding significance for future handling of similar problems.

A. The impact of rough surface dielectric constant on compound scattering characteristics

In Figs. 5 and 6, we conducted a comparative study on the surface currents and scattering coefficients of cylindrical targets under different rough surface relative permittivities. First, we set three different relative permittivities (5,0.6i), (10,0.6i), and (15,0.6i), keeping

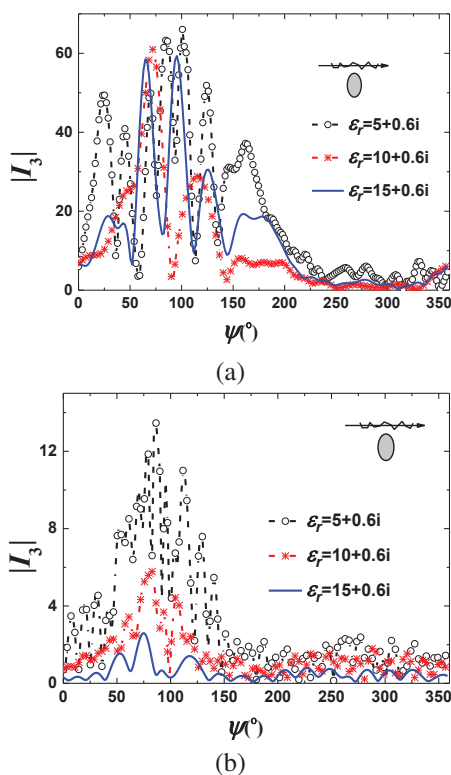


Fig. 5. The surface current of the cylinder beneath the rough dielectric surface: (a) TE incident wave and (b) TM incident wave.

other parameters unchanged. In these three cases, we observed that the induced surface currents and scattering coefficients of the target increase with the increase of relative permittivities.

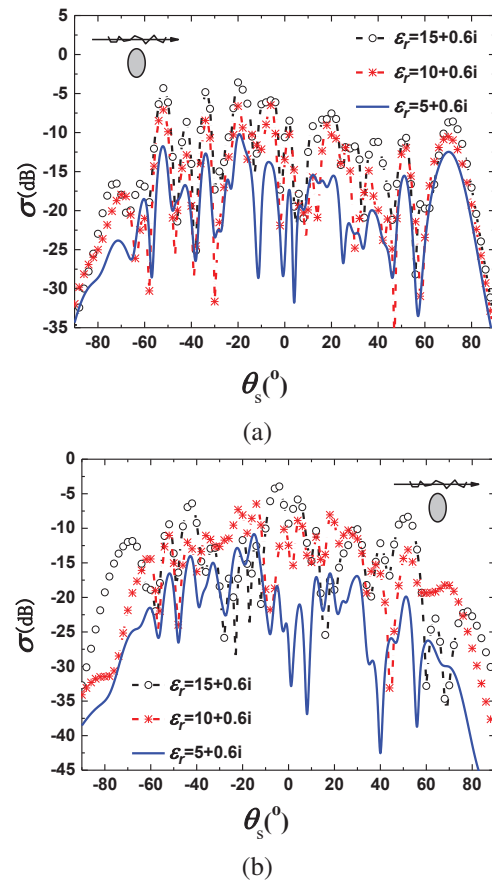


Fig. 6. The composite scattering coefficient of the rough dielectric surface and the cylinder: (a) TE incident wave and (b) TM incident wave.

To analyze this phenomenon in more depth, we further explored the impact of the rough surface relative permittivity on the target surface current. The higher the rough surface relative permittivity, the stronger the transmission of the dielectric, which in turn makes the excitation of the target stronger. This feature results in larger induced surface currents and better thermal conductivity when the relative permittivity is high.

At the same time, the scattering coefficient of the rough surface also increases with the increase of relative permittivity. This is because the scattering coefficient is affected by multiple reflections and interference of waves between rough and smooth surfaces. When the relative permittivity is high, the multiple reflection and interference effects become more apparent, leading to an increase in the scattering coefficient.

Further analysis suggests that this phenomenon is closely related to the transmission of the dielectric and

the multiple reflection and interference effects of the waves. Therefore, in practical applications, we need to consider these factors in order to more accurately assess and predict the scattering characteristics of the target.

B. The effect of changes in the target's dielectric constant on composite electromagnetic scattering properties

Figures 7, 8, and 9 show the changes in the surface currents and composite scattering coefficients of dielectric target 1 and dielectric target 2 when the dielectric constant of dielectric target 1 changes, respectively. We used a rough surface with a relative dielectric constant of $\varepsilon = 5 + 0.6i$ and set the radii of the two targets to $R_1 = R_2 = 1\lambda$, the depths to $H = 4\lambda$, and the distance between them to $D = 2\lambda$. In the calculation process, we took three different dielectric constants $\varepsilon_{o1} = 5 + 0.5i$, $\varepsilon_{o1} = 10 + 0.5i$, and $\varepsilon_{o1} = 15 + 0.5i$ as the dielectric constant of dielectric target 1, and the other parameters were consistent with previous settings.

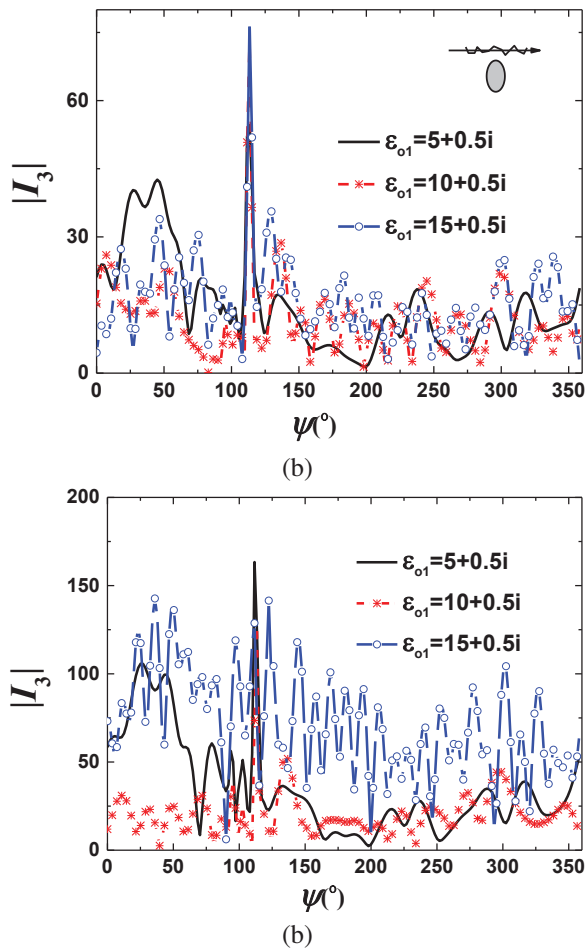


Fig. 7. The impact of changes in target 1's dielectric constant on its own surface current: (a) TE incident wave and (b) TM incident wave.

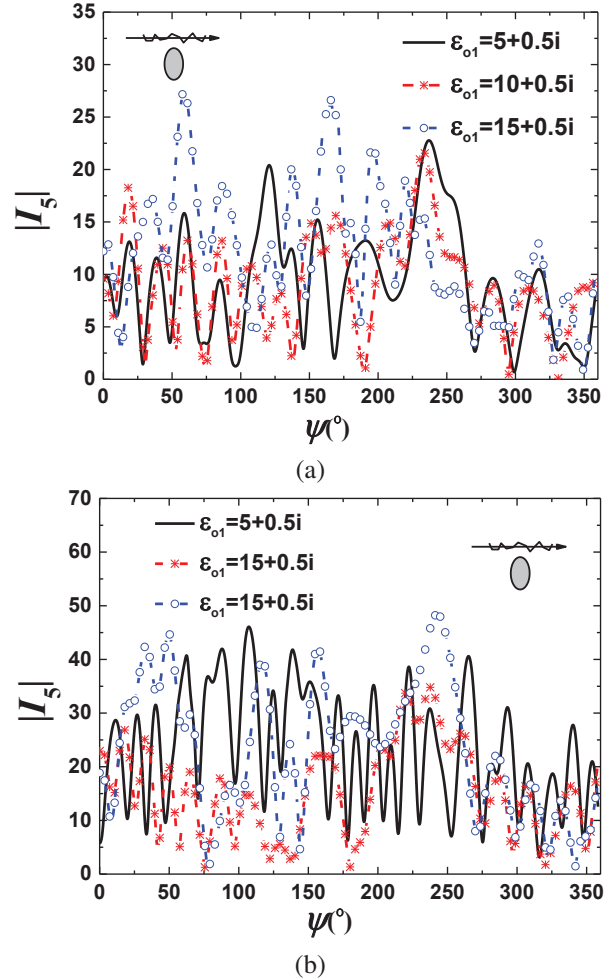


Fig. 8. The impact of changes in target 1's dielectric constant on the surface current of target 2: (a) TE incident wave and (b) TM incident wave.

In this study, we observed some interesting phenomena regarding how the target's dielectric properties affect the overall scattering characteristics. In particular, when the real part of the dielectric constant of target 1 is large, we found a significant increase in the induced current on the target surface, and the scattering effect of the rough surface became more pronounced. These observations strongly indicate that the dielectric properties of the target play a crucial role in its scattering characteristics. Therefore, it is essential to have a deep understanding and accurate prediction of the target's dielectric properties when analyzing or studying issues involving electromagnetic wave propagation and interaction.

In addition, we noticed in the experiment that the surface current of target 2 was affected by the changes in the dielectric constant of target 1. This phenomenon reveals the mutual influence between the two targets,

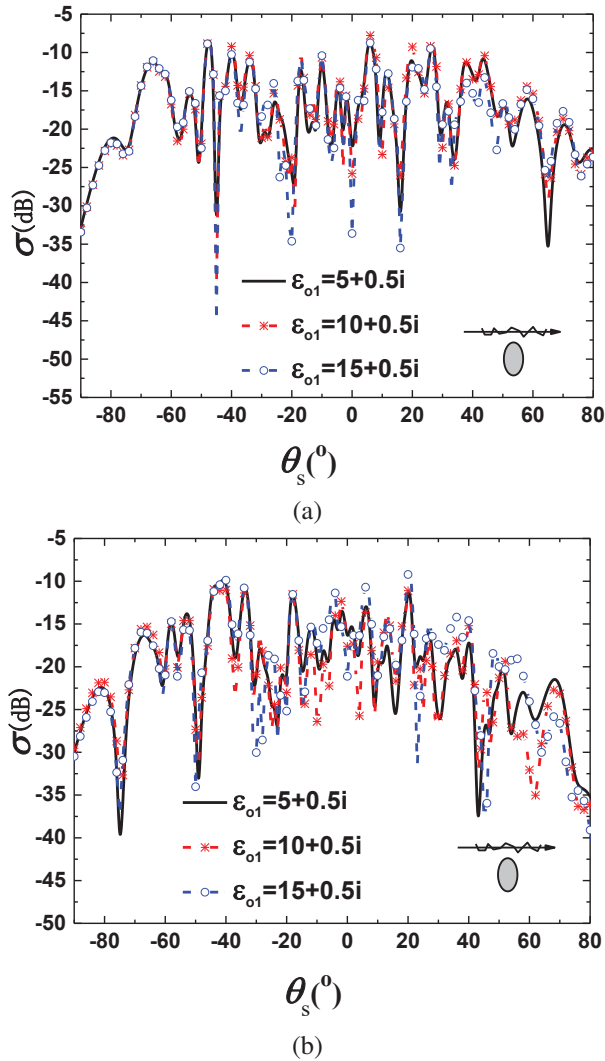


Fig. 9. The impact of changes in the target's dielectric constant on the scattering coefficient: (a) TE incident wave and (b) TM incident wave.

indicating that their coupling effect cannot be ignored. In the study of electromagnetic scattering problems, this coupling effect may cause certain prediction and estimation biases in practical applications. To avoid this situation, researchers need to fully consider and quantify the interactions between targets. Otherwise, neglecting the coupling effect between targets may lead to significant errors in the prediction and estimation of scattering characteristics, thereby affecting the accuracy and practicality of the model.

For practical applications, such as radar systems and communication systems, it is crucial to improve the accuracy of predicting and estimating scattering characteristics. The accuracy of prediction not only affects the effectiveness of applications but also affects the overall performance of the system. Therefore, consid-

ering the dielectric properties of targets and coupling effects is essential for studying electromagnetic wave propagation-related issues in practical applications.

C. The influence of the distance between two targets on the composite electromagnetic scattering characteristics

In Fig. 10, we observe that as the distance between the two targets gradually decreases, the coupling effect between them gradually strengthens. This coupling effect leads to an increase in the induced current on the target surface, which in turn significantly enhances the total scattering of the targets on the rough surface. Specifically, the smaller the distance between the two targets, the more intense their interaction, resulting in a more pronounced scattering phenomenon on the rough surface.

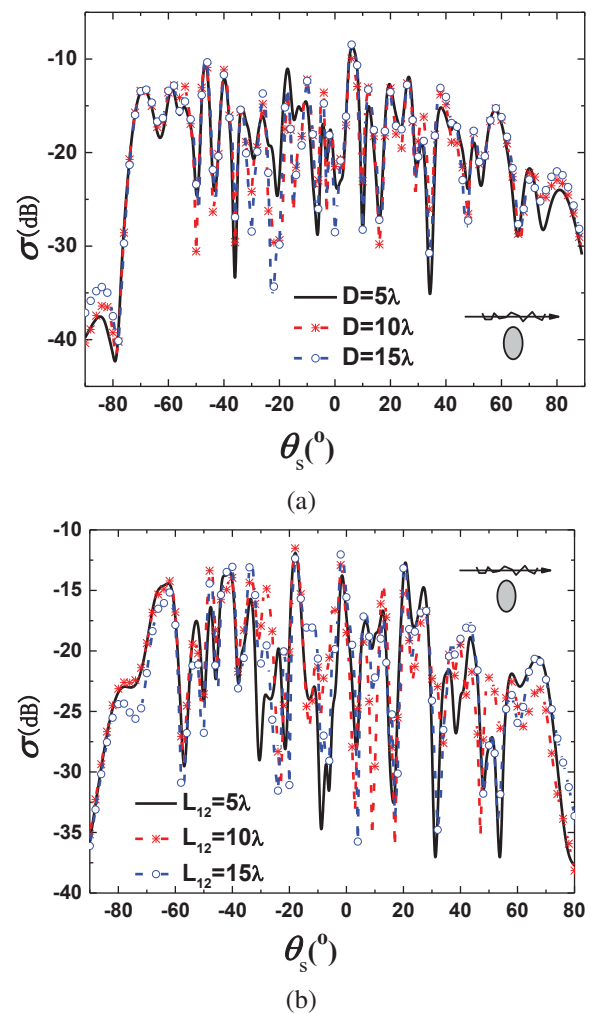


Fig. 10. The influence of the distance between two targets on the composite electromagnetic scattering characteristics: (a) TE incident wave and (b) TM incident wave.

In addition, the total scattering of the rough surface is also affected by the distance between the targets. When the two targets are closer together, the total scattering of the rough surface increases due to the enhanced coupling effect. This indicates that in practical applications such as radar detection systems, attention should be paid to this phenomenon.

In summary, the distance between targets has a significant impact on both the coupling effect between the two targets and the scattering on the rough surface. As the distance between the targets decreases, the mutual coupling between the targets becomes more prominent, leading to an increase in the scattering of the targets on the rough surface and the total scattering of the rough surface. Therefore, in-depth study of this phenomenon is of great importance for improving the detection accuracy in practical applications.

VI. CONCLUSION

In this paper, we propose a new fast iterative algorithm for investigating the electromagnetic scattering characteristics of a Gaussian rough surface and multiple targets below. We adopt the BMIA/CAG-CMG algorithm to improve computation efficiency and observe the effects of the dielectric properties of the rough surface and targets, as well as target spacing, on surface currents and composite scattering through simulation experiments. It is worth noting that we find that, under the same incident conditions, the higher the relative permittivity, the stronger the dielectric's transmission rate and target excitation, leading to an increase in scattering coefficients, which is consistent with our expectations.

In addition, we can also see that the smaller the target spacing, the stronger the interaction between them, resulting in more severe scattering on the rough surface. Ultimately, we reveal the interactive mechanism between two targets, providing valuable ideas and references for further understanding and studying composite scattering characteristics. In summary, our research results provide new insights and ideas for electromagnetic scattering theory and offer useful references for the application of electromagnetic scattering problems in related fields.

Next, we can explore more factors influencing electromagnetic scattering and further improve the algorithm's computation efficiency and accuracy. Meanwhile, we can also study the scattering characteristics of rough surfaces with different shapes and materials, as well as the electromagnetic scattering behavior of targets at different positions and directions, and so on. These studies will help us to understand electromagnetic scattering phenomena more deeply and provide more effective solutions for practical applications.

ACKNOWLEDGEMENT

This work was supported by Jiangxi Provincial Department of Education Science and Technology Project grant under GJJ2201716.

REFERENCES

- [1] Q. K. Wang, C. M. Tong, X. M. Li, Y. J. Wang, Z. L. Wang, and T. Wang, "Composite electromagnetic scattering and high-resolution SAR imaging of multiple targets above rough surface," *Remote Sensing*, vol. 14, no. 12, 2022.
- [2] J. Chen, M. Zhu, M. Wang, S. Li, and X. Li, "A Hybrid MoM-PO method combining ACA technique for electromagnetic scattering from target above a rough surface," *Applied Computational Electromagnetics Society (ACES) Journal*, vol. 29, no. 4, 2014.
- [3] L. Guan, J. E. Wang, X. Chen, D. H. Cai, and C. Z. Dong, "Electromagnetic scattering analysis of large-area vegetation based on multilevel periodic fast multipole algorithm," *Engineering Analysis with Boundary Elements*, vol. 147, pp. 1-8, 2023.
- [4] A. V. Setukha, S. L. Stavtsev, and R. M. Tret'yakova, "Application of mosaic-skeleton approximations of matrices in the physical optics method for electromagnetic scattering problems," *Computational Mathematics and Mathematical Physics*, vol. 62, no. 9, pp. 154-165, 2022.
- [5] X. M. Sun, "Influence evaluation of UAV inlet on electromagnetic scattering and time-frequency characteristics," *Journal of Physics: Conference Series*, vol. 1971, no. 1, pp. 1-6, 2021.
- [6] Y. Liang and L. X. Guo, "A study of composite scattering characteristics of movable/rotatable targets and a rough sea surface using an efficient numerical algorithm," *IEEE Journal of Oceanic Engineering*, vol. 46, no. 4, pp. 1412-1425, 2021.
- [7] D. Novák, L. Gregor, and J. Veselý, "Capability of a ground-based passive surveillance system to detect and track spaceborne SAR in LEO orbits," *Remote Sensing*, vol. 14, no. 18, 2022.
- [8] Y. C. Liang, Q. Z. Yang, Y. Q. Shi, J. Bai, and Q. Lin, "Numerical simulation and experimental study of ISAR imaging of spherical convergent flap nozzle," *Applied Computational Electromagnetics Society (ACES) Journal*, vol. 35, no. 4, 2020.
- [9] L. M. Madsen, T. Bording, D. Grombacher, N. Foged, N. Foley, H. A. Dugan, P. T. Doran, J. Mikucki, S. Tulaczyk, and E. Auken, "Comparison of ground-based and airborne transient electromagnetic methods for mapping glacial and permafrost environments: Cases from McMurdo Dry Valleys,

- Antarctica," *Cold Regions Science and Technology*, vol. 199, 2022.
- [10] J. He, Z. Xing, Q. Wang, F. Wu, and F. Lu, "A study on the diffraction correction prediction of electromagnetic field intensity based on the method of estimating aerial access network signal," *Wireless Commun. and Mobile Computing*, vol. 2021, 2021.
- [11] D. Zhang, C. Liao, J. Feng, X. Deng, and Y. Cheng, "Modeling of electromagnetic wave coupling to thin-wire structures in terrain environments using hybrid PE/TPIE method," *Int. J. Antennas and Propagation*, vol. 2019, 2019.
- [12] X. Deng, C. Gu, and Y. Zhou, "Electromagnetic scattering by arbitrary shaped three-dimensional conducting objects covered with electromagnetic anisotropic materials," *Applied Computational Electromagnetics Society (ACES) Journal*, vol. 26, no. 11, 2011.
- [13] C. Yang, and L. Wu, "GPU-Based volume rendering for 3D electromagnetic environment on virtual globe," *Int. J. Image Graphics and Signal Processing*, vol. 2, no. 1, 2010.
- [14] M. V. Grafkina, E. Y. Sviridova, and E. R. Veliyeva, "Environmental monitoring of electromagnetic fields in residential areas," *IOP Conference Series: Earth and Environmental Science*, vol. 688, no. 1, 2021.
- [15] X. L. Chen, C. Gu, X. Q. Deng, B. Z. Xu, Z. Li, and Z. Niu, "A hybrid ACA-FDM for electromagnetic scattering from PEC targets," *Applied Computational Electromagnetics Society (ACES) Journal*, vol. 27, no. 12, 2012.
- [16] J. Chen, S. Li, and Y. Song, "Analysis of electromagnetic scattering problems by means of a VSIE-ODDM-MLFMA method," *Applied Computational Electromagnetics Society (ACES) Journal*, vol. 27, no. 8, 2012.
- [17] O. Korostynska, A. Mason, M. Ortoneda-Pedrola, and A. Al-Shamma'a, "Electromagnetic wave sensing of NO₃ and COD concentrations for real-time environmental and industrial monitoring," *Sensors & Actuators: B. Chemical*, vol. 198, 2014.
- [18] E. Petraki, D. Nikolopoulos, A. Fotopoulos, D. Panagiotaras, G. Koulouras, A. Zisos, C. Nomicos, A. Louizi, and J. Stonham, "Self-organised critical features in soil radon and MHz electromagnetic disturbances: Results from environmental monitoring in Greece," *Applied Radiation and Isotopes*, vol. 72, 2013.
- [19] M. Tkalec, K. Malarić, and B. Pevalek-Kozlina, "Influence of 400, 900, and 1900 MHz electromagnetic fields on Lemna minor growth and peroxidase activity," *Bioelectromagnetics*, vol. 26, no. 3, 2005.
- [20] Y. Zeng, G. Zeng, L. Huang, X. Li, J. Guo, and J. Wang, "Application of transient electromagnetic method with multi-radiation field sources in deep edge mineral resources exploration," *Acta Geologica Sinica - English Edition*, vol. 95, no. S1, 2021.
- [21] H. Tan, F. Ling, Z. Guo, J. Li, and J. Liu, "Application of a wide-field electromagnetic method for hot dry rock exploration: A Case Study in the Gonghe Basin, Qinghai, China," *Minerals*, vol. 11, no. 10, 2021.
- [22] H. Wei, T. Qi, G. Feng, and H. Jiang, "Comparative Research on Noise Reduction of Transient Electromagnetic Signals Based on Empirical Mode Decomposition and Variational Mode Decomposition," *Radio Science*, vol. 56, no. 10, 2021.
- [23] M. Shen, "Launching system of helicopter aviation transient electromagnetic system," *Journal of Physics: Conference Series*, vol. 1802, no. 2, 2021.
- [24] G. Xue, L. Zhang, N. Zhou, and W. Chen, "Developments measurements of TEM sounding in China," *Geological Journal*, vol. 55, no. 3, 2020.
- [25] V. A. Kulikov, A. E. Kaminsky, and A. G. Yakovlev, "Combined 2D inversion of electrotomographic and audio-magnetotellurgic sounding data to solve mining problems," *Zapiski Gornogo Instituta*, vol. 223, no. 1, 2017.
- [26] G. X. Zou, C. M. Tong, J. Zhu, H. L. Sun, and P. Peng, "Study on composite electromagnetic scattering characteristics of low-altitude target above valley composite rough surface using hybrid SBR-EEC method," *IEEE Access*, vol. 8, pp. 152493-152502, 2020.
- [27] H. L. Sun, C. M. Tong, and P. Peng, "Improved hybrid FEM/MOM combining MLFMA for composite electromagnetic scattering," *Electromagnetics*, vol. 37, no. 8, pp. 479-492, 2017.
- [28] Y. Liang, L. X. Guo, Z. S. Wu, and Q. H. Liu, "A study of composite electromagnetic scattering from an object near a rough sea surface using an efficient numerical algorithm," *IEEE Antennas and Wireless Propagation Letters*, vol. 15, pp. 828-831, 2016.
- [29] J. Li, L. X. Guo, and S. Chai, "Composite electromagnetic scattering from an object situated above rough surface," *Applied Optics*, vol. 53, no. 35, pp. 8295-8304, 2014.
- [30] X. M. Zhu, and X. C. Ren, "Study on composite electromagnetic scattering from 1D weierstrass fractal land surface with buried target using FDTD," *Applied Mechanics and Materials*, vol. 539, pp. 539-543, June 2014.
- [31] M. L. Zhao, J. H. He, and N. Zhu, "Fast high-order algorithms for electromagnetic scattering problem from finite array of cavities in the case with high

- wave numbers,” *Mathematics*, vol. 10, no. 16, pp. 1-20, 2022.
- [32] J. M. Wu, X. B. He, B. Wei, and X. L. Li, “Fast parallel FDFD algorithm for solving electromagnetic scattering problems,” *Journal of Electrical and Electronic Engineering*, vol. 9, no. 6, pp. 455-460, 2021.
- [33] R. Q. Liu, X. W. Huang, Y. L. Du, M. L. Yang, and X. Q. Sheng, “Massively parallel discontinuous galerkin surface integral equation method for solving large-scale electromagnetic scattering problems,” *IEEE Transactions on Antennas and Propagation*, vol. 69, no. 9, pp. 5049-5059, 2021.
- [34] A. L. Deng, and L. M. Zhang, “Direct solution of the volume integral equation for electromagnetic scattering from dielectric objects with negative permittivity,” *Journal of the Optical Society of America. A, Optics, Image Science, and Vision*, vol. 38, no. 7, pp. 1031-1038, 2021.
- [35] W. Kong, X. Yang, F. Zhou, J. Xie, C. Chen, N. Li, and W. Yang, “Fast analysis of broadband electromagnetic scattering characteristics of electrically large targets using precorrected fast fourier transform algorithm based on near field matrix interpolation method,” *Applied Computational Electromagnetics Society (ACES) Journal*, vol. 36, no. 7, pp. 769-776, 2021.
- [36] L. Tsang, J. A. Kong, K. H. Ding, and C. O. Ao, “Scattering of electromagnetic waves: Numerical simulations,” *New York: Wiley Interscience*, 2001.
- [37] W. H. Press, S. A. Teukolsky, and W. T. Vetterling, “Numerical Recipes in FORTRAN,” *New York: Cambridge University Press*, 1992.
- [38] R. F. Harrington, “Field computation by moment method,” *New York: MacMillan*, 1968.



Lilan Lei was born in Jiangxi, China. She received the bachelor’s and master’s degrees from Jiangxi Normal University, Jiangxi, China, in 2002 and 2009, respectively. Her research interests include computer applications and computer communication.

Efficient Improved Local Time Stepping with the Leapfrog Scheme for Transient 3-D Electromagnetic Analyses

Minxuan Li^{1,2}, Qingkai Wu¹, Zhongchao Lin¹, Yu Zhang¹ and Xunwang Zhao¹

¹School of Electrical Engineering
Xidian University, Xi'an, 710071, China
zclin@xidian.edu.cn

²China Electronic Product Reliability and Environmental Testing Institute
Guangzhou, 511300, China
lwldlj@163.com

Abstract – An alternate boundary local time stepping (ABLTS) method is proposed for the discontinuous Galerkin time domain method for transient electromagnetic simulations to reduce the computation complexity of the local time stepping (LTS) method. The proposed method exhibits lower storage and time complexity than the conventional LF-LTS method. The stability, accuracy, and effectiveness of the ABLTS method are verified by applying it to the simulation of a resonator cavity and multi-layer microstrip antenna. The numerical results revealed that the developed method is effective for the transient electromagnetic simulation of antennas.

Index Terms – Antenna transient analysis, discontinuous Galerkin time domain method, high-order time integration, local time stepping.

I. INTRODUCTION

The discontinuous Galerkin time domain (DGTD) method is widely used in the transient simulation of antennas and microwave devices because of its high accuracy. The DGTD method introduces numerical flux into the finite element time domain (FETD) method [1–8] and exhibits higher accuracy and modeling flexibility than conventional time-domain methods such as finite difference time-domain (FDTD) method. The numerical flux decomposes the common basis function between neighboring elements, so that the governing equation can be established in one element and avoid building and decomposing large sparse matrices.

Runge-Kutta and leapfrog (LF) methods are the widely used explicit time integration schemes based on the DGTD method [6, 8, 9]. The LF scheme exhibits limited iteration steps. In the Courant–Friedrichs–Lewy (CFL) stability condition, the maximum time step size of explicit difference schemes is determined by the small-

est element. However, unstructured meshes typically produce some distorted and small-size elements, which leads to a minimal global time step size [9]. Local time stepping (LTS) methods are typically used to address the multi-scale problem [10–12]. The LTS method classifies elements into many parts according to their size in space; fine and coarse regions have different time step sizes [8–14]. However, if a fine region is adjacent to a coarse region, the fine region requires the numerical flux of the adjacent coarse region, and the coarse region cannot provide fields at the exact time because of the large time step. The LTS method based on the arbitrary high order (ADER) scheme compensates for the errors of different time steps through the high-order Taylor expansion of time partial conductance in the coarse region. The ADER-LTS method is highly accurate but requires time synchronization when it provides field information as the output. Furthermore, frequent synchronization leads to complications in time integration steps, the ADER-LTS requires extra memory because of storing fields at multiple time steps. Another LTS method based on the leapfrog (LF) scheme is frequently discussed [8–12]. The LF scheme presents second-order time accuracy and simpler iterations than the ADER scheme. When adjacent element fields are not obtained at the exact time, the accuracy of the LF scheme degrades to first-order and some interpolation methods [8, 11], which increase iteration complexity and memory, are used to compensate for the accuracy. However the interpolation slows the solving speed and needs to meet a more stringent stability condition.

In this study, we propose an alternate boundary LTS (ABLTS) method based on the LF-LTS method reported in [8]. The ABLTS method is applied to the DGTD method with hierarchical vector basis functions, avoids interpolation between coarse and fine regions, and maintains the concise iterations of the LF scheme. The storage

and time complexity of this method are lower than those of the interpolation LF-LTS method, which improves the universality of the LTS method. The simulation of a resonator cavity and patch antenna showed that the ABLTS method presents the high accuracy, fast speed, and low memory as the interpolation LF-LTS method.

II. PRINCIPLE AND FORMULATIONS

A. Numerical discretization of LTS-DGTD

The isotropic Maxwell's curl equations in 3-D space without sources and lossless are

$$\begin{cases} \nabla \times \mathbf{H} = \varepsilon \frac{\partial \mathbf{E}}{\partial t} \\ \nabla \times \mathbf{E} = -\mu \frac{\partial \mathbf{H}}{\partial t} \end{cases}, \quad (1)$$

where ε is the permittivity, μ is the permeability. \mathbf{E} and \mathbf{H} are expanded with the second-order hierarchical vector basis function reported in [6].

Using the Galerkin finite elements approach reported in [1], (1) can be expressed as the weak form with integration by parts as follows:

$$\begin{cases} \int_{\Omega_i} \varepsilon \frac{\partial \mathbf{E}}{\partial t} \cdot \mathbf{N}_i d\mathbf{v} - \int_{\Omega_i} \nabla \times \mathbf{N}_i \cdot \mathbf{H} d\mathbf{v} = \\ \int_{\Gamma_i} (\hat{\mathbf{n}} \times \mathbf{H}) \cdot \mathbf{N}_i ds, \\ \int_{\Omega_i} \mu \frac{\partial \mathbf{H}}{\partial t} \cdot \mathbf{N}_i d\mathbf{v} + \int_{\Omega_i} \nabla \times \mathbf{N}_i \cdot \mathbf{E} d\mathbf{v} = \\ - \int_{\Gamma_i} (\hat{\mathbf{n}} \times \mathbf{E}) \cdot \mathbf{N}_i ds, \end{cases} \quad (2)$$

where Ω is the computational domain divided into tetrahedrons Ω_i , Γ_i is the boundary of Ω_i , and $\hat{\mathbf{n}}$ is the normal vector located on Γ_i and points to the outside, \mathbf{N}_i is the weight functions of Ω_i . The DGTD method introduces numerical fluxes to evaluate the integration over tetrahedron interfaces. As a common numerical flux with excellent convergence, the upwind flux is introduced into (2), and the semi-discrete form with the upwind flux is expressed as follows [1]:

$$\begin{aligned} \varepsilon \mathbf{M}_i \frac{\partial \mathbf{E}_i}{\partial t} &= \mathbf{S}_i \mathbf{H}_i + \\ \sum_{p=1}^4 \left(k_h \mathbf{F}_{\Gamma_{pi}} (\mathbf{H}_j - \mathbf{H}_i) - v_e \mathbf{G}_{\Gamma_{pi}} (\mathbf{E}_j - \mathbf{E}_i) \right), \\ \mu \mathbf{M}_i \frac{\partial \mathbf{H}_i}{\partial t} &= -\mathbf{S}_i \mathbf{E}_i - \\ \sum_{p=1}^4 \left(k_e \mathbf{F}_{\Gamma_{pi}} (\mathbf{E}_j - \mathbf{E}_i) + v_h \mathbf{G}_{\Gamma_{pi}} (\mathbf{H}_j - \mathbf{H}_i) \right), \end{aligned} \quad (3)$$

where k_e , v_e , k_h , and v_h are the upwind flux coefficients [5], \mathbf{M} is the mass matrix, \mathbf{S} is the stiffness matrix, and \mathbf{F}_{Γ} and \mathbf{G}_{Γ} are the flux matrices.

(3) can be expressed in a highly concise form as follows:

$$\frac{\partial \mathbf{u}}{\partial t} = \mathbf{A}(\mathbf{u}), \quad (4)$$

where $\mathbf{u} = [\mathbf{E}, \mathbf{H}]^T$, \mathbf{A} denotes the terms of (3) other than the time partial term. According to the ADER scheme

reported in [12], \mathbf{u} can be expanded into Taylor series as follows:

$$\mathbf{u}(t + \Delta t) = \sum_{p=0}^{N_t} \frac{\Delta t^p}{p!} \frac{\partial^p \mathbf{u}(t)}{\partial t^p}, \quad (5)$$

where N_t is the order in the ADER scheme. The first order ADER scheme is expressed as follows:

$$\frac{\partial \mathbf{u}(t)}{\partial t} = \frac{\mathbf{u}(t + \Delta t) - \mathbf{u}(t)}{\Delta t} + O(t^2) = \mathbf{A}(\mathbf{u}). \quad (6)$$

For isotropic media, $\mathbf{A}(\mathbf{u}) = \mathbf{A}\mathbf{u}(t)$, this scheme becomes an explicit format and can be derived into the LF scheme using (6) as follows:

$$\begin{aligned} \frac{\mathbf{H}_i^{n+\frac{1}{2}} - \mathbf{H}_i^{n-\frac{1}{2}}}{\Delta t} &= \mu^{-1} \mathbf{M}_i^{-1} (-\mathbf{S}_i \mathbf{E}_i^n + f_{hi}(\mathbf{u})) \\ &= \mathbf{A}_{hi} \mathbf{u}(t), \\ \frac{\mathbf{E}_i^{n+1} - \mathbf{E}_i^n}{\Delta t} &= \varepsilon^{-1} \mathbf{M}_i^{-1} (\mathbf{S}_i \mathbf{H}_i^{n+\frac{1}{2}} + f_{ei}(\mathbf{u})) \\ &= \mathbf{A}_{ei} \mathbf{u}(t), \end{aligned} \quad (7)$$

where Δt is the size of the time step, and $f(\mathbf{u})$ denotes the flux term:

$$\begin{aligned} f_h(\mathbf{u}) &= - \sum_{p=1}^4 \left(k_e \mathbf{F}_{\Gamma_{pi}} (\mathbf{E}_j^n - \mathbf{E}_i^n) \right) + \\ &\quad \sum_{p=1}^4 \left(v_h \mathbf{G}_{\Gamma_{pi}} (\mathbf{H}_j^{n-\frac{1}{2}} - \mathbf{H}_i^{n-\frac{1}{2}}) \right), \\ f_e(\mathbf{u}) &= \sum_{p=1}^4 \left(k_h \mathbf{F}_{\Gamma_{pi}} (\mathbf{H}_j^{n+\frac{1}{2}} - \mathbf{H}_i^{n+\frac{1}{2}}) \right) - \\ &\quad \sum_{p=1}^4 \left(v_e \mathbf{G}_{\Gamma_{pi}} (\mathbf{E}_j^n - \mathbf{E}_i^n) \right). \end{aligned} \quad (8)$$

The half step between \mathbf{E} and \mathbf{H} proves that (8) has the second-order time accuracy [8]. The CFL condition constrains the Δt size [8, 9]:

$$\begin{aligned} 0 < \frac{\Delta t^2}{4} \max(\lambda(\mathbf{A}_{ei}), \lambda(\mathbf{A}_{hi})) < 1, \\ \Delta t_{LF} \leq \frac{2}{\sqrt{\max(\lambda(\mathbf{A}_{ei}), \lambda(\mathbf{A}_{hi}))}}, i \in \Omega \end{aligned} \quad (9)$$

where λ is the eigenvalue, and Δt_{LF} is the time step size of LF scheme.

B. Alternate boundary LTS scheme

The LF-LTS scheme can be used to expand (8) into the following:

$$\begin{cases} \frac{\mathbf{H}_i^{n+\frac{1}{2}} - \mathbf{H}_i^{n-\frac{1}{2}}}{\Delta t} = \\ \mathbf{A}_{hi} \left[\mathbf{E}_i^n, \mathbf{E}_j^n, \mathbf{H}_i^{n-\frac{1}{2}}, \mathbf{H}_j^{n-\frac{1}{2}} \right]^T, i \in e_c \\ \frac{\mathbf{E}_i^{n+1} - \mathbf{E}_i^n}{\Delta t} = \\ \mathbf{A}_{ei} \left[\mathbf{E}_i^n, \mathbf{E}_j^n, \mathbf{H}_i^{n+\frac{1}{2}}, \mathbf{H}_j^{n+\frac{1}{2}} \right]^T \end{cases} \quad (10)$$

$$\left\{ \begin{array}{l} \frac{\mathbf{H}_i^{n+\frac{1}{6}} - \mathbf{H}_i^{n-\frac{1}{6}}}{\Delta t/3} = \\ \mathbf{A}_{hi} \left[\mathbf{E}_i^n, \mathbf{E}_j^n, \mathbf{H}_i^{n-\frac{1}{6}}, \mathbf{H}_j^{n-\frac{1}{6}} \right]^T \\ \frac{\mathbf{E}_i^{n+\frac{1}{3}} - \mathbf{E}_i^n}{\Delta t/3} = \\ \mathbf{A}_{hi} \left[\mathbf{E}_i^n, \mathbf{E}_j^n, \mathbf{H}_i^{n+\frac{1}{6}}, \mathbf{H}_j^{n+\frac{1}{6}} \right]^T \end{array} \right., i \in e_f, \quad (11)$$

where e_f and e_c are the fine and coarse regions, respectively.

When the iteration steps of the fine region become an integer multiple of 3, the coarse region updates fields. According to the difference in the element scale, the computing domain can be classified into multiple LTS levels. The element of each level is coarse and fine for the upper and lower levels, respectively. Elements in the same LTS level Ω_{LTS} have the same time step Δt_{LTS} . A report [15] proved that

$$0 < \frac{\min(\Delta t_{LTS})^2}{4} \max(\lambda(\mathbf{A}_p)) < 1, \quad (12)$$

$$\mathbf{A}_p = \mathbf{A}_\Omega - \frac{\min(\Delta t_{LTS})^2}{8} \mathbf{A}_\Omega \mathbf{A}_{fine},$$

where \mathbf{A}_Ω is the matrix established using elements in Ω , \mathbf{A}_{fine} is the matrix established by employing elements in the fine region.

If i is in the fine region and j is in the coarse region, (11) becomes

$$\left\{ \begin{array}{l} \frac{\mathbf{H}_i^{n+\frac{1}{6}} - \mathbf{H}_i^{n-\frac{1}{6}}}{\Delta t/3} = \\ \mathbf{A}_h \left[\mathbf{E}_i^n, \mathbf{E}_j^n, \mathbf{H}_i^{n-\frac{1}{2}}, \mathbf{H}_j^{n-\frac{1}{2}} \right]^T \\ \frac{\mathbf{E}_i^{n+\frac{1}{3}} - \mathbf{E}_i^n}{\Delta t/3} = \\ \mathbf{A}_e \left[\mathbf{E}_i^n, \mathbf{E}_j^n, \mathbf{H}_i^{n-\frac{1}{2}}, \mathbf{H}_j^{n-\frac{1}{2}} \right]^T \end{array} \right., i \in e_f, \quad (13)$$

The field obtained using j is not at the exact time step and reduces the accuracy and stability; thus, the time accuracy of (13) has the first order. In general, efficient methods, such as introduction of interpolation or exact iteration in an interface, are used to refine this scheme [6, 9–11], which increases the computing time and requires additional memory.

To avoid introducing interpolation, the boundary of fine and coarse elements is reconstructed so that the difference scale of coarse elements on the boundary is changed to be consistent with that of fine elements. The changed elements are alternate boundary (AB) elements, as displayed as Fig. 1.

Considering (5), a different scheme of AB elements can be transformed into the following expression as the second-order scheme

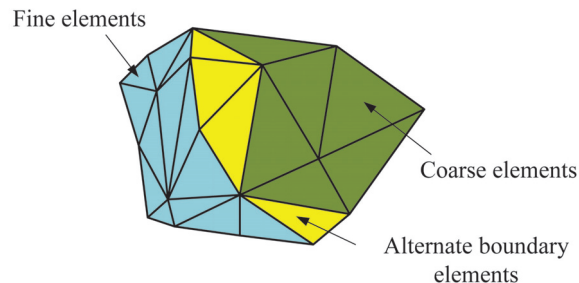


Fig. 1. Common case of alternate boundary method in which the yellow elements are alternate boundary elements that belong to the coarse region.

$$\mathbf{u}^{n+\frac{1}{3}} \simeq \mathbf{u} \left(t + \frac{\Delta t}{3} \right) = \mathbf{u}(t) + \frac{\Delta t}{3} \frac{\partial \mathbf{u}(t)}{\partial t} + \frac{1}{2} \left(\frac{\Delta t}{3} \right)^2 \frac{\partial^2 \mathbf{u}(t)}{\partial t^2} + O(\Delta t^3). \quad (14)$$

(14) provides the exact field of the coarse region and retains the second-order time accuracy in fine regions.

Different from the 2-D nodal basis function reported in [8, 9], the contribution of 3-D hierarchical vector basis functions to the upwind flux is mainly concentrated in the adjacent face and edges, and the orders are 0.5, 1.5, and 2, which render the spatial accuracy consistent with the time accuracy. The reciprocity of linear equations with the same order in space and time was confirmed in [16]. (14) of element i in the coarse region becomes:

$$\frac{\mathbf{u}_i^{n+\frac{1}{3}} - \mathbf{u}_i^n}{\Delta t/3} = \mathbf{A} \mathbf{u}_i^n + \frac{1}{2} \mathbf{A} \left[\frac{\Delta t}{2} \mathbf{A} \mathbf{u}_i^{n-\frac{1}{2}} \right] + O(\Delta t^3), \quad (15)$$

rewriting the equation in the LF scheme, we obtain

$$\frac{\mathbf{H}_i^{n+\frac{1}{6}} - \mathbf{H}_i^{n-\frac{1}{6}}}{\Delta t/3} = \mathbf{A}_h \left[\mathbf{E}_i^n, \mathbf{H}_i^{n-\frac{1}{6}}, \mathbf{E}_j^n, \mathbf{H}_j^{n-\frac{1}{6}} \right]^T + \frac{\Delta t}{4} \mathbf{A}_h \mathbf{A}_e \left[\mathbf{E}_i^n, \mathbf{H}_i^{n-\frac{1}{6}}, \mathbf{E}_j^n, \mathbf{H}_j^{n-\frac{1}{6}} \right]^T + O(\Delta t^3). \quad (16)$$

(16) indicates that only two iterations of the AB element are required to obtain a field with high-order accuracy, according to (15). (16) also maintains the characteristics of the explicit scheme; hence, the AB elements must meet the CFL conditions of the fine region.

C. Computation work of ABLTS

It's obvious that (16) is able to suppress errors in the coarse elements, and there will be an exact time step from the adjacent fine elements when (16) is applied in the upwind flux. Therefore, AB elements only need to maintain the same update scheme as adjacent fine elements to ensure that the accuracy of adjacent coarse elements is maintained at the second-order.

This feature makes the computation work of ABLTS method simpler than interpolation methods in [15]. For

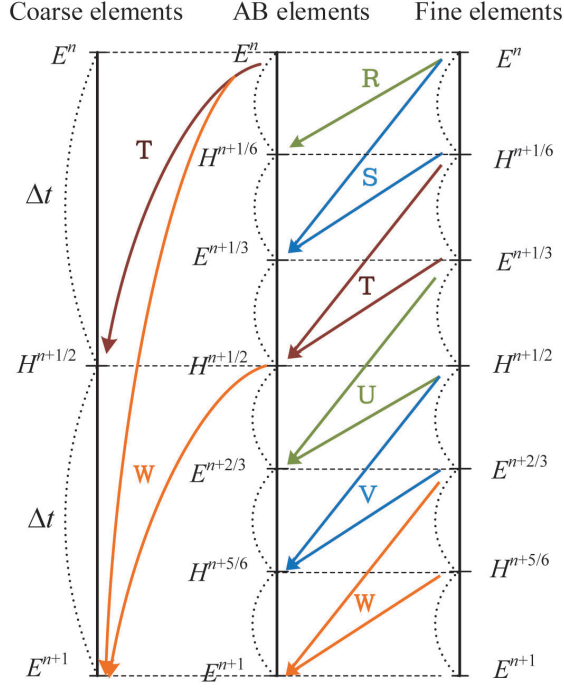


Fig. 2. Computation work of ABLTS in the LF scheme, The time step size has $\Delta t_2 = 3\Delta t_1$; the red dotted lines are fields provided by Eq. (16).

example, when the problem has 3 classes, the computation work of ABLTS is shown in Fig. 2.

The update for electric field of AB elements at the exact time is similar to (16):

$$\frac{E_i^{n+\frac{1}{3}} - E_i^n}{\Delta t/3} = \mathbf{A}_e \left[E_i^n, H_i^{n+\frac{1}{6}}, E_j^n, H_j^{n+\frac{1}{6}} \right]^T + \frac{\Delta t}{4} \mathbf{A}_h \mathbf{A}_e \left[E_i^n, H_i^{n+\frac{1}{6}}, E_j^n, H_j^{n+\frac{1}{6}} \right]^T + O(\Delta t^3). \quad (17)$$

From (16) and (17), the stability of the ABLTS method remains explicitly dependent on Δt , and the upwind flux ensures equation convergence. The order of time in AB elements is the same as second-order interpolation. Therefore, the time step size of ABLTS follows (12).

III. NUMERICAL RESULTS AND DISCUSSION

In this section, the simulation of a resonator cavity and multi-layer antenna is presented to show the stability and efficiency of the ABLTS method.

A. Resonator cavity

First, the characteristics of a resonator cavity are analyzed to confirm the stability and accuracy of the proposed method. The cavity is $1\text{ m} \times 1\text{ m} \times 1\text{ m}$ and is terminated using a perfect electronic conductor (PEC)

boundary. The interior of the resonant cavity is filled with air, so that the resonant frequency obtained using the analytical solution is 212.132 MHz. The cavity is partitioned to A, B, and C regions, and the mesh size ratio of these regions is set to 1:3:9 for showing the multi-scale situation.

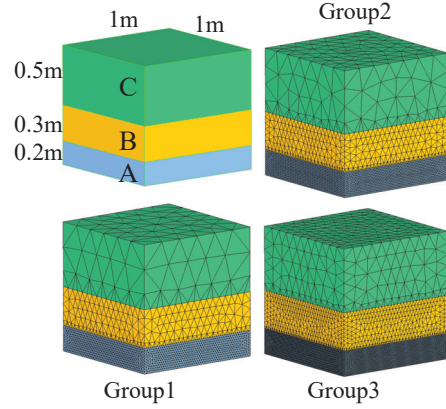


Fig. 3. Geometry and meshes of the resonator cavity.

To verify the stability and accuracy of the ABLTS method, three control groups are used for testing. The mesh size of region A in these control groups were 10, 15, and 20 mm. After mesh generation, the numbers of elements of these groups are 75,351, 35,679, and 17,114 tetrahedrons; the number of degree of freedoms (Dofs) are 3,014,040, 1,427,160, 684,560. A point source is excited at the center of the cavity with modulated Gaussian pulse from 100 to 300 MHz. The DGTD method with LF, LF-LTS presented in [9], and ABLTS methods are used to simulate the wave propagation of 1000 ns in the cavity. The minimum time step size of the above methods is 37.562 ps. Fig. 3 shows the geometry of the cavity.

Table 1 presents the performance comparison of the relative error and solution time of LF, LTS, and ABLTS methods, and the relative error is compared with the result of analytical solution of 212.132 MHz (absolute error/analytical solution). For the same mesh and excitation and solution times, the accuracy of the ABLTS method is the same as that of the LF method and higher than that of the LF-LTS method. The speed of the ABLTS method is similar to that of the LF-LTS method and considerably higher than that of the LF method. In this example, the spatial discretization at a maximum scale of 0.127 wavelengths and following eq. (9) and eq. (12) to estimate the time step, three groups of experiments at different scales all maintained stable working for a long time as Fig. 4 shows, demonstrating the stability of the proposed method. The electric field of the cavity is shown in Fig. 5.

Table 1: Performance comparison among different methods

Group	Performance	LF	LF-LTS	ABLTS
Group 1	Time (min)	315.4	90.64	90.75
	Speedup	\	3.48	3.48
	Freq (MHz)	212.106	212.011	212.105
	Relative error	0.01%	0.06%	0.01%
Group 2	Time (min)	69.12	22.35	22.07
	Speedup	\	3.09	3.08
	Freq (MHz)	212.095	212.003	212.093
	Relative error	0.02%	0.06%	0.02%
Group 3	Time (min)	27.51	9.09	9.1
	Speedup	\	3.02	3.02
	Freq (MHz)	212.039	211.991	212.039
	Relative error	0.04%	0.07%	0.04%

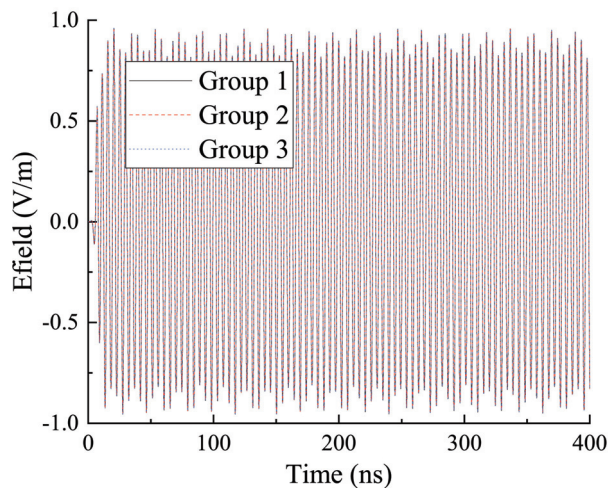


Fig. 4. Nearfield of the proposed method.

B. Multi-layer microstrip antenna array

A multi-layer microstrip antenna array is analyzed using the DGTD-ABLTS method to show its efficiency and accuracy. The array had four layers (Fig. 6); the first layer of the upper part is made of Rogers RO3203, whose permittivity is 3.02. The second and fourth layers are composed of Arlon CuClad 250GT, whose permittivity is 2.5. The third layer is a perfect electric conductor. The computation domain is terminated by the Silver-Muller absorb boundary condition. Four lump ports excited the feed network through a modulated Gaussian pulse from 13.5 GHz to 17.5 GHz. The number of tetrahedrons is 1,735,017, the number of Dofs is 69,400,680, and the ABLTS method decomposes meshes into three levels. The numbers of tetrahedron of each LTS levels are 42,264, 408,453, and 1,731,841. The pulse propagated in the model in 4 ns.

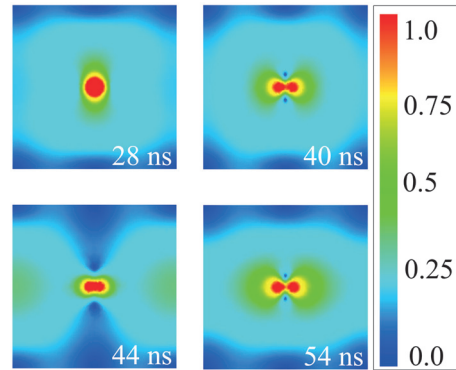


Fig. 5. Electric field (V/m) of the cavity at 28 ns, 40 ns, 44 ns, and 54 ns.

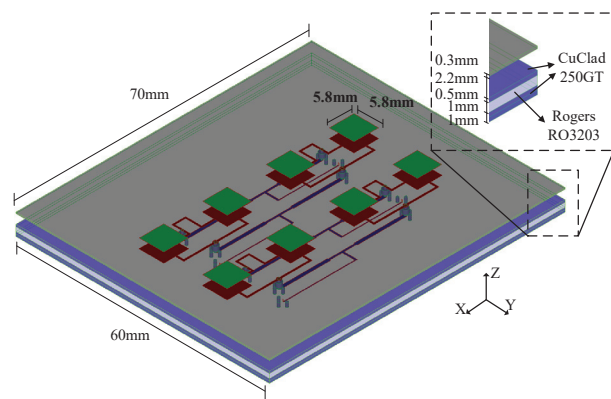


Fig. 6. Geometry of the multi-layer microstrip antenna array.

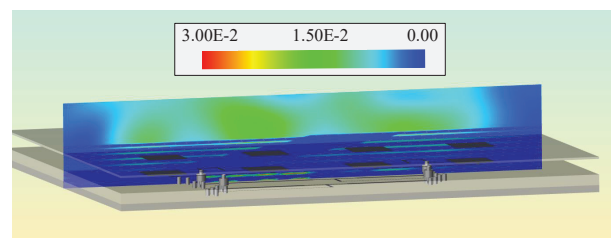


Fig. 7. Electric field (V/m) in the XOZ plane at 0.8 ns.

Figure 7 shows the electric field distribution in the XOZ plane at 0.8 ns, and Fig. 6 presents the Gain Total in the YOZ plane in comparison with the result of HFSS. Furthermore, Table 2 presents the computational performance of the LF-DGTD and proposed methods, in which δ denotes the relative error. All the methods are run on CPUs with 240 processors. The computation efficiency of the DGTD method considerably improved with ABLTS and the memory and accuracy are almost unchanged.

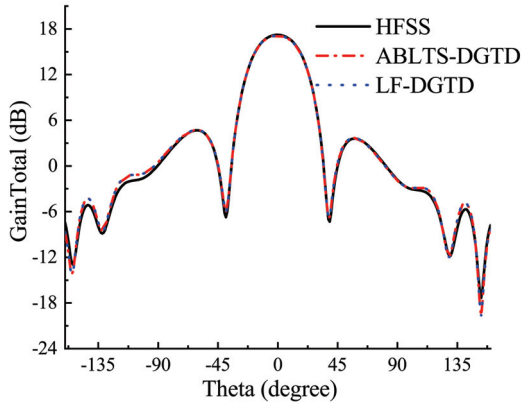


Fig. 8. GainTotal in YOZ plane calculated by the proposed method and HFSS.

Table 2: Performance of the DGTD with ABLTS

	Peak Memory (MB)	Solution Time (min)	δ (Compare with LF)	Speedup (Compare with LF)
LF	29,264.1	416.3	\	\
LTS	29,266.9	54.2	0.0937	7.68
ABLTS	29,267.3	54.7	0.0815	7.61

IV. CONCLUSIONS

An ABLTS method of DGTD is introduced for electromagnetic simulation of antennas. The DGTD-ABLTS method is a noninterpolation local time stepping scheme based on the leapfrog integration scheme, which reduces the error of the LTS method by two iterations with the second-order accuracy. The simulation of a resonator cavity and multi-layer antenna array proved the accuracy and efficiency of the DGTD-ABLTS method. The DGTD-ABLTS method is efficient for the large-scale electromagnetic simulation of antennas.

ACKNOWLEDGMENT

This work was supported by the Key Research and Development Program of Shaanxi(2023-ZDLGY-09, 2021GXLH-02), and the Fundamental Research Funds for the Central Universities (QTZX22160), and the Special Funds of CEPREI (23Z013).

REFERENCES

- [1] J. S. Hesthaven and T. Warburton, *Nodal Discontinuous Galerkin Methods: Algorithms, Analysis, and Applications*, New York, NY, USA: Springer, 2008.
- [2] A. Bossavit, "Whitney forms: a class of finite elements for three-dimensional computations in electromagnetism," *IEE Proceedings A Physical Science, Measurement and Instrumentation, Management and Education, Reviews*, vol. 135, no. 8, pp. 493-500, 1988.
- [3] X. Zhao, Z. Lin, Y. Zhang, S. Ting, and T. K. Sarkar, "Parallel Hybrid method of HO-MoM-MLFMA for analysis of large antenna arrays on an electrically large platform," *IEEE Transactions on Antennas and Propagation*, vol. 64, no. 12, pp. 5501-5506, Dec. 2016, doi:10.1109/TAP.2016.2621029.
- [4] L. Zhao, G. Chen, W. Yu, and J. M. Jin, "A fast waveguide port parameter extraction technique for the DGTD method," *IEEE Antennas and Wireless Propagation Letters*, vol. 16, pp. 2659-2662, 2017, doi:10.1109/LAWP.2017.2740298.
- [5] S. Dosopoulos and J. F. Lee, "Interior penalty discontinuous Galerkin finite element method for the time-dependent first order Maxwell's equations," *IEEE Transactions on Antennas and Propagation*, vol. 58, no. 12, pp. 4085-4090, Dec. 2010, doi:10.1016/j.jcp.2010.07.036.
- [6] J. Chen and Q. Liu, "Discontinuous Galerkin time-domain methods for multiscale electromagnetic simulations: A review," *Proceedings of the IEEE*, vol. 101, no. 2, pp. 242-254, Feb. 2013, doi:10.1109/JPROC.2012.2219031.
- [7] L. Zhao, G. Chen, W. Yu, and J. M. Jin, "A fast waveguide port parameter extraction technique for the DGTD method," *IEEE Antennas and Wireless Propagation Letters*, vol. 16, pp. 2659-2662, 2017, doi:10.1109/LAWP.2017.2740298.
- [8] M. J. Grote and M. Teodora, "Explicit local time-stepping methods for time-dependent wave propagation," *arXiv: Numerical Analysis*, 2012, doi:10.48550/arXiv.1205.0654.
- [9] E. Montseny, S. Pernet, X. Ferrières, and G. Cohen, "Dissipative terms and local time-stepping improvements in a spatial high order Discontinuous Galerkin scheme for the time-domain Maxwell's equations," *Journal of Computational Physics*, vol. 227, no. 14, pp. 6795-6820, 2008.
- [10] L. Fezoui, S. Lanteri, S. Lohrengel, and S. Piperno, "Convergence and stability of a discontinuous Galerkin time-domain method for the 3D heterogeneous Maxwell equations on unstructured meshes," *ESAIM, Mathematical Modelling and Numerical Analysis*, vol. 39, no. 6, pp. 1149-1176, 2005.
- [11] J. Alvarez, L. D. Angulo, A. R. Bretones, C. M. Coevorden and S. G. Garcia, "Efficient antenna modeling by DGTD: Leap-frog discontinuous Galerkin timedomain method," *IEEE Antennas and Propagation Magazine*, vol. 57, no. 3, pp. 95-106, June 2015, doi:10.1109/MAP.2015.2437279.
- [12] M. Li, Q. Wu, Z. Lin, Y. Zhang, and X. Zhao, "Novel parallelization of discontinuous galerkin method for transient electromagnetics simulation based on sunway supercomputers," *Applied*

Computational Electromagnetics Society (ACES) Journal, vol. 37, no. 7, pp. 795-804, Sep. 2021, doi:10.13052/2022.ACES.J.370706.

- [13] M. Li, Q. Wu, Z. Lin, Y. Zhang, and X. Zhao, "A minimal round-trip strategy based on graph matching for parallel dgt method with local Time-stepping," *IEEE Antennas and Wireless Propagation Letters*, vol. 22, no. 2, pp. 243-247, Feb. 2023, doi:10.1109/LAWP.2022.3208010.
- [14] Z. G. Ban, Y. Shi, and P. Wang, "Advanced parallelism of DGT method with local time stepping based on novel MPI + MPI unified parallel algorithm," *IEEE Transactions on Antennas and Propagation*, vol. 70, no. 5, pp. 3916-3921, 2022, doi:10.1109/TAP.2021.3137455.
- [15] G. Cohen, X. Ferrieres, and S. Pernet, "A spatial high-order hexahedral discontinuous Galerkin method to solve Maxwell's equations in time domain," *Journal of Computational Physics*, vol. 217, no. 2, pp. 340-363, 2006, doi:10.1016/j.jcp.2006.01.004.
- [16] S. Zuo, Z. Lin, D. G. Doñoro, Y. Zhang, and X. Zhao, "A parallel direct domain decomposition solver based on schur complement for electromagnetic finite element analysis," *IEEE Antennas and Wireless Propagation Letters*, vol. 20, no. 4, pp. 458-462, Apr. 2021, doi:10.1109/LAWP.2021.3053566.



Minxuan Li was born in Changzhi, Shanxi, China, in 1994. He received the B.S. degree in electronic information engineering from Harbin Institute of Technology in 2016. He is currently pursuing the Ph.D. degree with Xidian University. He joined the China Institute of Electronic Product Reliability and Environmental Testing in 2023. His research interests include channel modeling, parallel computation, and transient electromagnetic analysis.



Qingkai Wu was born in Yangzhou, Zhejiang, China, in 1997. He received the B.S. degree in electronic science and technology from Xidian University in 2020. He is currently pursuing the Ph.D. degree with Xidian University. His current research interests include transient electromagnetic analysis.



Zhongchao Lin was born in Hubei, China, in 1988. He received the B.S. and Ph.D. degrees from Xidian University, in 2011 and 2016, respectively. He joined Xidian University, in 2016, as a post doctoral fellow, where he was lately promoted as an associate professor. His research interests include large-scale computational electromagnetic, scattering, and radiation electromagnetic analysis.



YU ZHANG received the B.S., M.S., and Ph.D. degrees from Xidian University, in 1999, 2002, and 2004, respectively. In 2004, he joined Xidian University as a faculty member. He was a visiting scholar and an adjunct professor with Syracuse University, from 2006 to 2009. As a principal investigator, he works on projects, including the project of NSFC. He has authored four books: *Parallel Computation in Electromagnetics* (Xidian University Press, 2006), *Parallel Solution of Integral Equation-Based EM Problems in the Frequency Domain* (Wiley IEEE, 2009), *Time and Frequency Domain Solutions of EM Problems Using Integral Equations and a Hybrid Methodology* (Wiley, 2010), and *Higher Order Basis Based Integral Equation Solver* (Wiley, 2012), as well as more than 100 journal articles and 40 conference papers.



Xunwang Zhao was born in Shanxi, China, in 1983. He received the B.S. and Ph.D. degrees from Xidian University, in 2004 and 2008, respectively. He joined Xidian University, in 2008, as a faculty member, where he was lately promoted as a full professor. He was a visiting scholar with Syracuse University, from December 2008 to April 2009. As a principal investigator, he works on several projects, including the project of NSFC. His research interests include computational electromagnetic and electromagnetic scattering analysis.

Novel Characteristic Mode Basis Functions Accelerating Iteration Convergence of CMM for Analyzing Electromagnetic Scattering Problems

Fei Guo¹, Zhonggen Wang^{1*}, Yufa Sun², Wenyan Nie³, Pan Wang¹, and Juan Wu¹

¹School of Electrical and Information Engineering
Anhui University of Science and Technology, Huainan, 232001, China
fguo@aust.edu.cn, zgwang@ahu.edu.cn, pwangsunny@foxmail.com, yj165@mail.ustc.edu.cn
*Corresponding author: Zhonggen Wang

²School of Electronics and Information Engineering
Anhui University, Hefei, 230039, China
yfsun_ahu@sina.com

³School of Mechanical and Electrical Engineering
Huainan Normal University, Huainan, 232001, China
wynie5240@163.com

Abstract – In this study, a novel characteristic mode basis function construction method is proposed to solve the problems of low efficiency and slow convergence of the iterative solution of the characteristic mode method. First, the characteristic modes (CMs) of each extended block are calculated separately by dividing objects, the CMs construction efficiency is improved for the decreased matrix dimensionality. Next, the effective CMs are selected as basis functions according to the modal significances. Finally, to improve the poor conditional number of the reduced matrix for the block extension, the singular value decomposition is used to enhance the orthogonality among these basis functions. Several numerical calculations show that the proposed method has significant efficiency and accuracy.

Index Terms – Characteristic mode, method of moments, reduced matrix, singular value decomposition.

I. INTRODUCTION

The method of moments (MoM) [1] is a popular method for solving electromagnetic scattering, which has the advantage of high computational accuracy. However, as the size of the object increases, there is a substantial escalation in computational complexity and memory usage. To alleviate this problem, various fast and effective methods have been proposed, such as the fast multipole method (FMM) [2], multilevel fast multipole method (MLFMM) [3], adaptive cross approximation (ACA) [4], and adaptive integration method (AIM) [5]. These methods effectively reduce the complexity of matrix-vector product computation, but they usually

resort to iterative methods. In order to reduce the dimensionality of the matrix, macro basis function is introduced into the MoM. For example, the synthetic basis function (SBF) method [6], sub-entire-domain (SED) basis function method [7], and characteristic basis function method (CBFM) [8]. Based on the principle of domain decomposition, the CBFM divides the object into multiple blocks. Nevertheless, it demands a substantial number of incident excitations, and the construction of basis functions consumes a considerable amount of time.

The characteristic mode (CM) is an intrinsic mode adapted to an arbitrary electromagnetic structure, independent of the applied excitation [9]. It is particularly suitable for the analysis of multi-excitation problems. Thus, the CM theory is widely used in the design and simulation of antennas [10–13], while it is rarely applied in the analysis of electromagnetic scattering problems. The traditional CM method (CMM) [14] presents a high computational complexity and low efficiency in solving CMs. Subsequently, it is unsuitable for large electrical problems. To improve the efficiency of CMM analysis of electromagnetic scattering problems, the CMs are used directly as the basis functions in [15]. Nevertheless, it is difficult to apply it to electrically large problems due to the complexity of the algorithm. Consequently, a fast multipole algorithm is introduced in [16] to accelerate the solution of CMs. However, the improvement is not significant due to the large size of the impedance matrix. In addition, the CMM is combined with compressive sensing, used to analyze the bistatic scattering problems in [17], but the dimensionality of the measurement

matrix is large. Furthermore, considering the coupling between the incident wave and the dielectric body, a new CMM is proposed to analyze the scattering problems in [18]; however, the computation complexity of CMs is relatively high. Innovatively, a method proposed in [19] utilizes principal component analysis (PCA) to accelerate the iterative solution of CMM, which improved the solution efficiency.

Unlike the previous works, based on the idea of regional blocking, this study proposes a novel characteristic mode basis function method (NCMBFM). First, the object is divided into multiple blocks and extended, selecting effective modes as basis functions. Next, the orthogonality between these basis functions is strengthened by using the singular value decomposition (SVD) [20] method. As a result, the condition number of the reduced matrix is improved, which could effectively boost the efficiency of the iterative solution. The corresponding numerical results verify the efficiency and reliability of the proposed method in the analysis of electrically large problems.

II. THEORY

A. Characteristic mode method

The surface currents on the object are extended using the Rao-Wilton-Glisson (RWG) [21] basis function, and the MoM is employed to generate the matrix equation as follows:

$$\mathbf{Z}\mathbf{J} = \mathbf{V}, \quad (1)$$

where \mathbf{Z} is an impedance matrix with the size of $N \times N$ and N is the number of unknowns; \mathbf{J} and \mathbf{V} represent the current coefficients vector and excitation vector, respectively. According to the CM theory, for an arbitrarily shaped PEC, the CMs are generated from its impedance matrix as follows:

$$\mathbf{Z} = \mathbf{R} + j\mathbf{X}, \quad (2)$$

$$\mathbf{X}\mathbf{J}^{\text{CM}} = \lambda\mathbf{R}\mathbf{J}^{\text{CM}}, \quad (3)$$

where \mathbf{R} and \mathbf{X} are the real and imaginary parts of \mathbf{Z} , respectively. \mathbf{J}^{CM} denotes the eigenvector, corresponding to the eigenvalue λ . Depending on the nature of the CMs, the superposition of a few low-order CMs is sufficient to approximate the surface currents. In this context, these low-order modes are chosen as basis functions. This selection approach relies on modal significances (MS), defined as

$$\text{MS} = \left| \frac{1}{1 + j\lambda} \right|. \quad (4)$$

Moreover, a threshold τ_{cm} related to the MS is set, and then, a group of eigenvalues is determined based on $\text{MS} > \tau_{cm}$. The corresponding significant CMs are obtained as the characteristic mode basis functions (CMBFs). Assuming that the total number of CMBFs is K , the surface currents of the object is expressed by a

linear superposition of these CMBFs as

$$\mathbf{J} = \sum_{k=1}^K a^k \mathbf{J}^{\text{CM}_k}, \quad (5)$$

where a^k is the coefficient of the CMBFs to be solved and \mathbf{J}^{CM_k} the k th CMBFs. Substituting equation (5) into equation (1) and multiplying both sides of the equation with the transpose of \mathbf{J}^{CM} , a reduced matrix equation about a^k of reduced order is obtained, expressed as

$$\mathbf{Z}^{\text{R}}a = \mathbf{V}^{\text{R}}, \quad (6)$$

where \mathbf{Z}^{R} is a reduced matrix with a dimension of $K \times K$ and $\mathbf{V}^{\text{R}} = (\mathbf{J}^{\text{CM}})^{\text{T}}\mathbf{V}$ is a $K \times 1$ vector. Furthermore, a is the matrix of extension coefficients obtained by solving equation (6).

However, when analyzing electrically large objects, as the matrix dimension increases, solving equation (3) becomes more complex, which poses challenges to the solution of the CMs.

B. Novel characteristic mode basis function method

Different from the CMM to construct CMBFs, this study builds on the idea of regional blocking to divide the object into m blocks. However, the blocking resulted in a change in the shape of the object, causing corresponding changes in the CMs of each block. As a consequence, these CMs could no longer accurately represent the original current distribution on each block. To solve this issue, each block is extended to ensure the smoothness and continuity of the characteristic current near the virtual boundary. The principle and application of blocking is shown in Fig. 1 (take a cylinder as the example). Where the blue part indicates the mutual impedance matrix, the yellow part indicates the self-impedance matrix, and the dashed line portion indicates the extended self-impedance matrix.

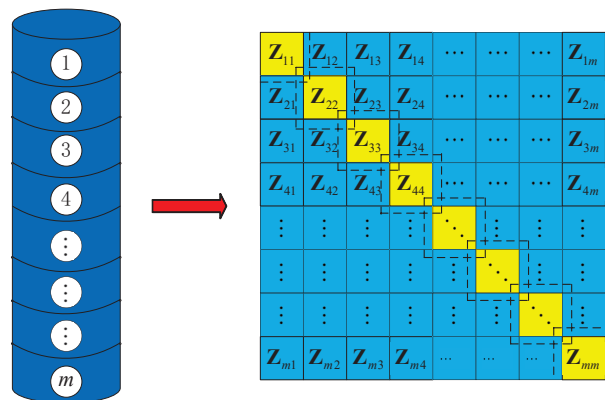


Fig. 1. The principle and application of blocking.

As a result, equation (1) changed as follows:

$$\begin{bmatrix} \mathbf{Z}_{11} & \mathbf{Z}_{12} & \cdots & \mathbf{Z}_{1m} \\ \mathbf{Z}_{21} & \mathbf{Z}_{22} & \cdots & \mathbf{Z}_{2m} \\ \vdots & \vdots & \cdots & \vdots \\ \mathbf{Z}_{m1} & \mathbf{Z}_{m2} & \cdots & \mathbf{Z}_{mm} \end{bmatrix} \begin{bmatrix} \mathbf{J}_1 \\ \mathbf{J}_2 \\ \vdots \\ \mathbf{J}_m \end{bmatrix} = \begin{bmatrix} \mathbf{V}_1 \\ \mathbf{V}_2 \\ \vdots \\ \mathbf{V}_m \end{bmatrix}, \quad (7)$$

where the self-impedance matrix \mathbf{Z}_{ii} and mutual impedance matrix \mathbf{Z}_{ij} are used to represent the interactions between different blocks. The current coefficient vector \mathbf{J}_i and excitation vector \mathbf{V}_i are associated with block i . The CMs of each extension block are solved by equations (8) and (9), selected effective modes as basis functions by MS, as follows:

$$\mathbf{Z}_{ii} = \mathbf{R}_{ii} + j\mathbf{X}_{ii}, \quad (8)$$

$$\mathbf{X}_{ii}\mathbf{J}_i^{\text{CM}} = \lambda\mathbf{R}_{ii}\mathbf{J}_i^{\text{CM}}. \quad (9)$$

It is worth noting that as the number of blocks increases, the dimension of the self-impedance matrix for each block becomes smaller, leading to improved efficiency in solving CMs. However, the increase in the number of CMs results in a higher dimensionality of the reduced matrix, necessitating iterative solutions. Furthermore, even though blocking and extending could improve the efficiency of solving CMs, they weaken the orthogonality between CMs, which eventually leads to a worse condition number of the reduced matrix, and the iterative solution converges slowly.

For this reason, after removing the extension and selecting effective CMs using the MS, the SVD is applied to these CMs. The process of SVD is as follows:

$$\mathbf{J}_i^{\text{CM}} = \mathbf{U}\mathbf{W}\mathbf{V}^{\text{T}}, \quad (10)$$

where \mathbf{J}_i^{CM} represent the set of all basis functions on the block i with a dimension of $N_i^e \times P_i$; N_i^e and P_i denote the number of unknowns and initial basis functions after extending on block i , respectively. \mathbf{U} and \mathbf{V}^{T} are both orthogonal matrixes with the dimension of $N_i^e \times N_i^e$ and $P_i \times P_i$, respectively. \mathbf{W} is a diagonal matrix with the dimension of $N_i^e \times P_i$. The elements of the diagonal are arranged from largest to smallest with a rapid decay trend, all of which are singular values of \mathbf{J}_i^{CM} . Afterwards, the left singular value vectors in \mathbf{U} are retained as the novel characteristic mode basis functions (NCMBFs). Supposing that the number of NCMBFs retained on each block is L_i , the current of block i is expressed as

$$\mathbf{J}_i = \sum_{l=1}^{L_i} a_i^l \mathbf{J}_i^{\text{NCMB}_l}, \quad (11)$$

where a_i^l is the coefficient matrix to be solved and $\mathbf{J}_i^{\text{NCMB}_l}$ is the l th NCMBFs of block i . On this basis, the original current of the object is expressed as

$$\mathbf{J} = \sum_{i=1}^M \sum_{l=1}^{L_i} a_i^l \mathbf{J}_i^{\text{NCMB}_l}, \quad (12)$$

where a_i^l is obtained by solving a reduced matrix with the size of $\sum_{i=1}^M L_i \times \sum_{i=1}^M L_i$.

In general, solving equation (6) is categorized into direct and iterative methods. However, the construction of the reduced matrix $\mathbf{Z}^{\text{R}} = (\mathbf{J}^{\text{NCM}})^{\text{T}} \mathbf{Z} \mathbf{J}^{\text{NCM}}$ is associated with the CMs. For electrically large problems, as the number of dividing blocks increases, the count of CMs increases, resulting in a larger dimension of the reduced matrix, thereby making direct method solution difficult. Based on this situation, the SVD technique and an iterative method are employed to solve the problem in this paper. Compared to the CMM, the condition number of the reduced matrix constructed using NCMBFs is diminished, leading to a notably improved convergence rate in the iterative solution of the reduced matrix.

III. COMPLEXITY ANALYSIS

The calculation of CMM and NCMBFM mainly primarily involve three processes, generating basis functions, constructing the reduced matrix, and solving the reduced matrix. For simplicity, the effect of the extension in NCMBFM is ignored, and the number of NCMBFs and unknowns in each block are assumed to be P and N/M , respectively. The computational complexity is analyzed for the CMM and NCMBFM as follows:

1. Generating basis functions: In the CMM, equation (3) is commonly solved using the implicitly restarted Arnoldi method (IRAM), the most time-consuming of which is the LU decomposition [22], with the complexity of $O(N^3)$. However, constructing NCMBFs in NCMBFM mainly consists of LU decomposition and SVD; both of them have the complexity of $O(M(N/M)^3)$, so the complexity of the NCMBFM is $O(2M(N/M)^3) \approx O((N/M)^3)$. Since N is always greater than N/M , NCMBFM can expedite the generation of basis functions, and the acceleration factor is M^3 .
2. Constructing the reduced matrix: Because of the different number of basis functions, the complexity of constructing the reduced matrix in the CMM and NCMBFM is $O(KN^2)$ and $O(PMN^2)$, respectively. Since K and PM are constants, the computational complexities of both are close.
3. Solving the reduced matrix equation: In CMM, the small number of solved CMs leads to a smaller dimension of the reduced matrix, which is suitable for using LU decomposition with complexity $O(N_c^3)$ to solve it directly, where N_c is the dimension of the reduced matrix. However, in CMB_iLU (CMB_iLU means the incomplete LU decomposition preconditioning method is used to accelerate the iterative convergence of the blocked CMM) and NCMBFM, as the number of unknowns increases,

more CMs are obtained, resulting in the increased dimensionality of the reduced matrix that requires iterative method with a complexity of $O(N_{iter}N_r^2)$ to solve. N_{iter} and N_r represent the number of iterations and the size of the reduced matrix, respectively. For NCMBFM, the condition number of the reduced matrix is better and the required N_{iter} is smaller, resulting in an acceleration factor of N'_{iter} (N'_{iter} is the difference in the number of iterations).

In summary, compared to CMM, the blocking operation in NCMBFM accelerates the generation of basis functions, albeit resulting in larger dimension of the constructed reduced matrix. In comparison to CMB_iLU, the introduction of the SVD process enhances the orthogonality between basis functions, optimizes the condition number of reduced matrices, and accelerates the iterative solution of the reduced matrix equation.

IV. NUMERICAL RESULTS

To verify the efficiency of the proposed method, the scattering properties of three objects are analyzed using the MoM, CMM, CMB, and NCMBFM. For convenience of expression, the CMM of blocking is defined as CMB. The generalized minimal residual (GMRES) method is used for the iterative algorithm. The threshold of the iLU decomposition is empirically set to 0.001 and the tolerance of the GMRES to 1E-05. In addition, to estimate the accuracy of the calculation results, the relative error is introduced as follows:

$$\text{Err} = \left(\frac{\|\sigma_{\text{cal}} - \sigma_{\text{MoM}}\|_2}{\|\sigma_{\text{MoM}}\|_2} \right) \times 100\%, \quad (13)$$

where σ_{cal} and σ_{MoM} represent the radar cross section (RCS), calculated via the used method and MoM, respectively. Since CMM generates fewer basis functions and has a lower reduced matrix dimension, the reduced matrix equation is solved using a direct method. Meanwhile, the calculated results of CBFM are added as a comparison. Besides, we have included a comparison of the effects between NCMBFM and CM-PCA [19] in this section.

Initially, the bistatic RCS of a cylinder with a radius of 0.2 m and a height of 1 m is analyzed at an incident frequency of 1.8 GHz. The cylinder's surface is discretized using RWG functions, resulting in 18,478 triangles and 27,711 unknowns. With the threshold τ_{cm} of the MS set to 0.001, 1404 effective modes are generated in CMM. Subsequently, the object is divided into 16 blocks, and the extension size is set to 0.15λ in NCMBFM, creating 3520 effective modes and 41244 unknowns.

To investigate the effect of different extended sizes on the accuracy, the change of RCS Err with τ_{cm} under different extended sizes is given in Fig. 2. It can be observed that as the extended size increases, the accuracy increases, but so does the number of unknowns and the

number of NCMBFs. To balance time and accuracy, the extended size and τ_{cm} are set to 0.15λ and 0.001, respectively. To test the effect of with and without SVD on the orthogonality between NCMBFs, the changes in the condition number of the reduced matrix with different extended sizes are shown in Table 1. It can be found that the condition number of the reduced matrix, constructed without SVD, increases significantly as the extended size grows, eventually reaching the point of becoming an ill-conditioned matrix. However, when NCMBFs are handled with SVD, the condition number of their constructed reduced matrix is significantly decreased. Therefore, the SVD helps to strengthen the orthogonality between basis functions to achieve the effect of optimizing the condition number of the reduced matrix.

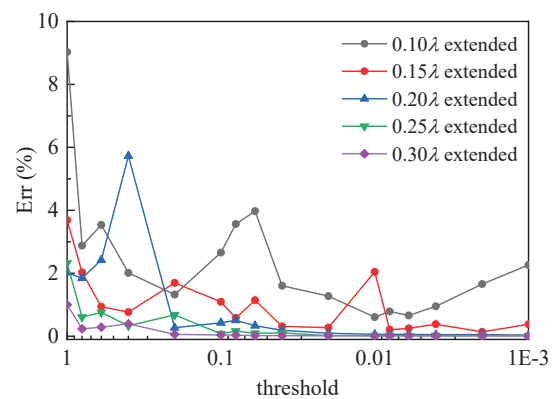


Fig. 2. Err of NCMBFM with different extended sizes.

Table 1: Condition number of reduced matrix constructed with and without SVD for different extended sizes

Extended Size	Condition Number of Reduced Matrix	
	Without SVD	With SVD
0.10λ	6.0388E+05	1.4050E+04
0.15λ	3.8820E+06	1.2081E+04
0.20λ	9.6412E+06	1.5381E+04
0.25λ	9.8231E+06	6.5468E+03
0.30λ	2.4077E+07	4.7326E+03

The iteration number of several different methods for the reduced matrix solution is compared in Fig. 3. Compared to these methods, the proposed approach exhibits the fewest iterations, resulting in a more efficient solution to the reduced matrix equation. The bistatic RCS of cylinder horizontal polarization is plotted in Fig. 4. It is shown that the proposed method is in excellent agreement with the calculated results of the MoM, CMM, and CBFM.

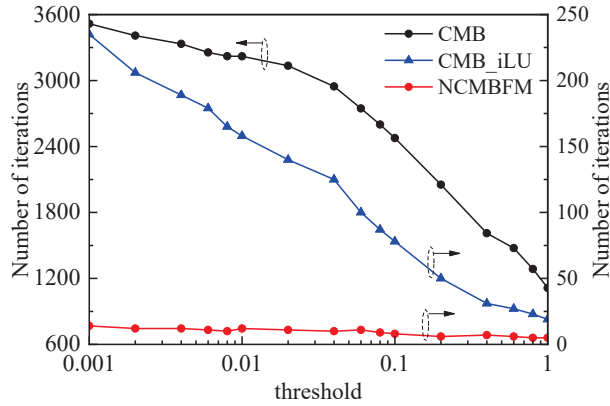


Fig. 3. The number of iterations for solving the reduced matrix using different methods.

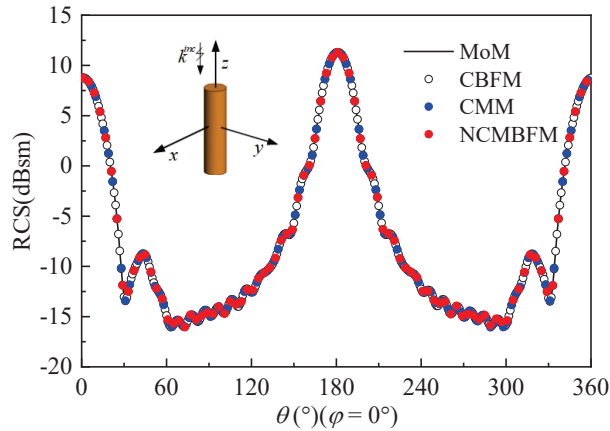


Fig. 4. Bistatic RCS of cylinder in horizontal polarization.

Next, a missile with a length of 1 m is calculated for bistatic RCS at 3 GHz. The surface of the missile is discretized by the RWG functions to generate 21,880 triangles and 32,820 unknowns. Meanwhile, the threshold τ_{cm} of MS is set to 0.001. In NCMBFM, the missile is divided into 26 blocks, and an extension of 0.15λ is chosen to create 52,662 unknowns. 1609 effective modes are obtained in CMM, while 4663 effective modes are acquired in NCMBFM. Compared with the CMB_iLU, the condition number of the reduced matrix constructed by NCMBFs decreased from $1.1309E+08$ to $1.6832E+04$ in NCMBFM. Moreover, the proposed method diminished the number of iterations in solving the reduced matrix equation from 277 to 17. Hence, the solution efficiency is significantly improved. The bistatic RCS of vertical polarization for several methods is shown in Fig. 5. The results show that the proposed method is consistent with the calculation results of the MoM and CMM with high accuracy.

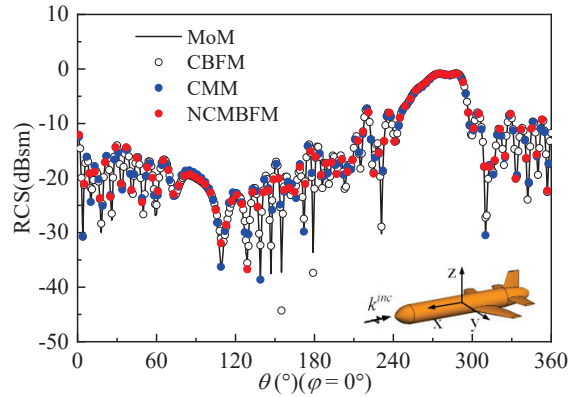


Fig. 5. Bistatic RCS of missile in vertical polarization.

Finally, the bistatic RCS with a cone-sphere with a gap at an incident frequency of 6.2 GHz is calculated. The RWG basis functions discretize the target surface to obtain 27,898 triangles and 41,847 unknowns. At the same time, the threshold τ_{cm} of MS is set to 0.001. In the CMM, 1959 effective modes are obtained. In NCMBFM, 6357 effective modes and 73,638 unknowns are acquired by dividing the target into 45 blocks and extending each block by 0.15λ . Compared to CMB_iLU, the proposed approach reduces the matrix condition number from $6.2385E+08$ to $1.1048E+04$, while it decreases to $4.8327E+04$ in CM-PCA. In addition, the iteration number for solving the reduced matrix equation dropped from 530 to 30, while it is 42 in CM-PCA. The efficiency of iterative solution is greatly improved. The horizontal polarized bistatic RCS of the cone-sphere with a gap is shown in Fig. 6. It can be concluded that the proposed method is in good agreement with the results of the MoM.

Although both SVD and PCA are featured to enhance orthogonality within the data, but there are

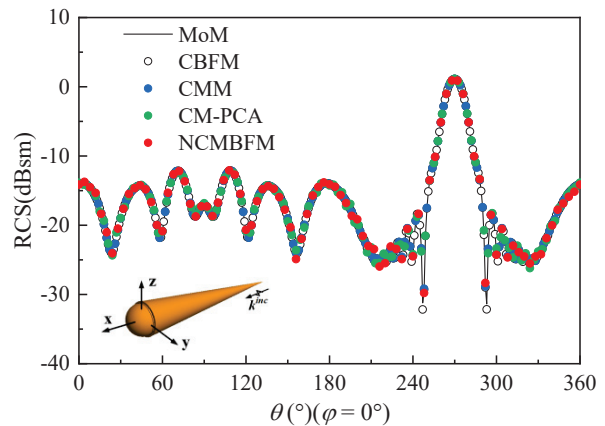


Fig. 6. Bistatic RCS of cone-sphere with a gap in vertical polarization.

Table 2: The simulation time of different processes and RCS Err

Model	Method	Basis Functions Construction Time (s)	Number of Basis Functions	Reduced Matrix Filling Time (s)	Solving Time (s)	Total Time (s)	RCS Err (%)
Cylinder	CBFM	716.4	4303	495.0	6.3	2163.6	0.34
	CMM	3325.3	1404	47.5	2.1	4834.7	0.21
	CMB_iLU	108.1	3520	131.1	247.4	1931.4	0.25
	NCMBFM	117.7	3520	132.1	9.1	1702.6	0.37
	CBFM	1148.8	5798	933.7	9.2	4118.5	2.78
Missile	CMM	5336.1	1609	76.5	2.5	7516.1	1.52
	CMB_iLU	185.9	4663	441.8	282.8	3650.6	1.87
	NCMBFM	223.8	4663	440.9	9.5	3375.9	2.11
	CBFM	1889.4	7875	1508.2	29.7	5638.3	2.63
Cone-sphere with a gap	CMM	8136.3	1959	323.8	3.2	11618	1.33
	CM-PCA	541.3	6357	627.7	41.8	4382.4	1.97
	CMB_iLU	336.1	6357	630.7	914.1	5071.2	1.60
	NCMBFM	374.9	6357	629.4	33.3	4229.1	1.81

differences in the implementation and advantages. First, SVD is applicable to various types of data and provides an optimal low-rank approximation of the data, which has global optimality and stability. In contrast, PCA is a statistical method based on the covariance matrix, which may be influenced by the distribution of the data. Second, SVD is a rigorous mathematical method that precisely decomposes a matrix into a product between two orthogonal matrixes and a diagonal matrix, which maximizes the enhancement of orthogonality. Third, SVD has a wider application, such as data noise reduction, data reconstruction, and matrix approximation. Finally, SVD can be viewed as a special case of PCA, which also has data interpretability.

In addition, the simulation times of different processes and RCS Err corresponding to Figs. 4, 5, and 6 are given in Table 2. Compared to the CMM, the proposed method greatly reduces the time of generating basis functions and solving the reduced matrix equation. The total time for the three simulations is decreased by 65%, 56% and 63%, respectively. Thus, the solution efficiency is substantially improved. However, in CM-PCA, the covariance matrix is constructed by computing the covariance, and then the principal components are obtained through SVD. Subsequently, data reconstruction is performed. In contrast, the proposed method handles CMs faster and with greater efficiency.

Furthermore, both the proposed method and CBFM are based on the idea of regional decomposition; the CBFM compared in the paper constructs the characteristic basis functions (CBFs) by multilevel plane wave and SVD. But the proposed method has the following advantages: In CBFM, the construction of the basis functions is very time-consuming since it requires massive incident excitations and uses SVD to remove redundancy. In

contrast, CM is independent of excitation, applicable to objects of any shape, and the basis functions are faster to construct. Simultaneously, multiple experimental results have demonstrated that, under comparable accuracy conditions, the proposed method generates fewer basis functions. Therefore, the proposed method constructs the reduced matrix faster.

V. CONCLUSION

In this study, a novel method is proposed to accelerate the analysis of electromagnetic scattering properties of large electrical objects. By introducing the idea of blocking to decrease the dimensionality of the impedance matrix, the efficiency of solving CMs is significantly improved. Innovatively, SVD is applied to process the CMs, thereby enhancing their orthogonality, improving the condition number of the reduced matrix, and achieving rapid convergence in the iterative solution of the reduced matrix equation. Compared to CMM, the proposed method significantly reduces computational time while maintaining accuracy, as evidenced by the complexity analysis and numerical simulation results. Simultaneously, it provides a new way to analyze the electromagnetic scattering properties of electrically large objects.

ACKNOWLEDGMENT

This work is supported in part by the Natural Science Foundation of Anhui Provincial under Grant no. 2108085MF200, in part by the National Natural Science Foundation of China under Grant no. 62071004 and no. 62105004, and in part by the Natural Science Foundation of the Anhui Higher Education Institutions of China under Grant no. 2022AH051583.

REFERENCES

- [1] R. F. Harrington, *Field Computation by Moment Methods*, New York, Macmillan, 1968.
- [2] N. Engheta, W. D. Murphy, V. Rokhlin, and M. S. Vassiliou, "The fast multipole method (FMM) for electromagnetic scattering problems," *IEEE Transactions on Antennas and Propagation*, vol. 40, no. 6, pp. 634-641, June 1992, DOI:10.1109/8.144597.
- [3] J. M. Song and W. C. Chew, "Multilevel fast-multipole algorithm for solving combined field integral equations of electromagnetic scattering," *Microwave and Optical Technology Letters*, vol. 10, no. 1, pp. 14-19, 1995, DOI:10.1002/mop.4650100107.
- [4] K. Zhao, M. N. Vouvakis, and J. Lee, "The adaptive cross approximation algorithm for accelerated method of moments computations of EMC problems," *IEEE Transactions on Electromagnetic Compatibility*, vol. 47, no. 4, pp. 763-773, Nov. 2005, DOI:10.1109/TEMC.2005.857898.
- [5] E. Bleszynski, M. Bleszynski, and T. Jaroszewicz, "AIM: Adaptive integral method for solving large-scale electromagnetic scattering and radiation problems," *Radio Science*, vol. 31, no. 5, pp. 1225-1251, Sep. 1996, DOI:10.1029/96RS02504.
- [6] A. Freni, P. De Vita, P. Pirinoli, L. Matekovits, and G. Vecchi, "Fast-factorization acceleration of mom compressive domain-decomposition," *IEEE Transactions on Antennas and Propagation*, vol. 59, no. 12, pp. 4588-4599, Dec. 2011, DOI:10.1109/TAP.2011.2165474.
- [7] W. B. Lu, T. J. Cui, and H. Zhao, "Acceleration of fast multipole method for large-scale periodic structures with finite sizes using sub-entire-domain basis functions," *IEEE Transactions on Antennas and Propagation*, vol. 55, no. 2, pp. 414-421, Feb. 2007, DOI:10.1109/TAP.2006.889805.
- [8] E. Lucente, A. Monorchio, and R. Mittra, "An iteration free MoM approach based on excitation independent characteristic basis functions for solving large multiscale electromagnetic scattering problems," *IEEE Transactions on Antennas and Propagation*, vol. 56, no. 4, pp. 999-1007, Apr. 2008, DOI:10.1109/TAP.2008.919166.
- [9] R. Harrington and J. Mautz, "Theory of characteristic modes for conducting bodies," *IEEE Transactions on Antennas and Propagation*, vol. 19, no. 5, pp. 622-628, Sep. 1971, DOI:10.1109/TAP.1971.1139999.
- [10] J. Zeng, X. Liang, L. He, F. Guan, F. H. Lin, and J. Zi, "Single-fed triple-mode wideband circularly polarized microstrip antennas using characteristic mode analysis," *IEEE Transactions on Antennas and Propagation*, vol. 70, no. 2, pp. 846-855, Feb. 2022, DOI:10.1109/TAP.2021.3111280.
- [11] S. Zhao, X. Li, Y. Chen, W. Zhao, and Z. Qi, "A wide-beam metasurface antenna using pattern combination of characteristic modes," *Applied Computational Electromagnetics Society (ACES) Journal*, vol. 37, no. 1, pp. 41-49, Jan. 2022, DOI:10.13052/2022.ACES.J.370105.
- [12] Y. Zeng, S. Zhang, and S. Luo, "pattern analysis of conformal antenna arrays via the characteristic modes of isolated elements," *Applied Computational Electromagnetics Society (ACES) Journal*, vol. 36, no. 12, pp. 1562-1568, Dec. 2021, DOI:10.13052/2021.ACES.J.361207.
- [13] C. Jia, P. Gu, Z. He, and R. Chen, "Convergence acceleration of characteristic mode-based basis function method for connected array structures," *IEEE Transactions on Antennas and Propagation*, vol. 70, no. 8, pp. 7322-7327, Aug. 2022, DOI:10.1109/TAP.2022.3145471.
- [14] G. Angiulli, G. Amendola, and G. Di Massa, "Application of characteristic modes to the analysis of scattering from microstrip antennas," *Journal of Electromagnetic Waves and Applications*, vol. 14, no. 8, pp. 1063-1081, 2000, DOI:10.1163/156939300X00978.
- [15] X. Qi, Z. Nie, Y. Chen, X. Que, and J. Hu, "Multi-excitation simulation of half-space scattering using characteristic mode theory," *2018 IEEE International Conference on Computational Electromagnetics*, Chengdu, China, pp. 1-2, 2018, DOI:10.1109/COMP.2018.8496703.
- [16] Q. I. Dai, J. Wu, H. Gan, Q. S. Liu, W. C. Chew, and W. E. I. Sha, "Large-scale characteristic mode analysis with fast multipole algorithms," *IEEE Transactions on Antennas and Propagation*, vol. 64, no. 7, pp. 2608-2616, July 2016, DOI:10.1109/TAP.2016.2526083.
- [17] Z. Wang, P. Wang, Y. Sun, and W. Nie, "Fast analysis of bistatic scattering problems for three-dimensional objects using compressive sensing and characteristic modes," *IEEE Antennas and Wireless Propagation Letters*, vol. 21, no. 9, pp. 1817-1821, Sep. 2022, DOI:10.1109/LAWP.2022.3181602.
- [18] Y. Chen and S. Yang, "Scattering analysis for arbitrarily shaped dielectric bodies using characteristic modes," *2016 10th European Conference on Antennas and Propagation*, Davos, Switzerland, pp. 1-5, 2016, DOI:10.1109/EuCAP.2016.7481129.
- [19] Z. Wang, F. Guo, W. Nie, Y. Sun, and P. Wang, "Principal component analysis accelerated the iterative convergence of the characteristic mode basis function method for analyzing electromagnetic

scattering problems,” *Progress in Electromagnetics Research M*, vol. 117, pp. 129-138, 2023, DOI: 10.2528/PIERM23041504.

- [20] E. Lucente, A. Monorchio, and R. Mittra, “An iteration-free mom approach based on excitation independent characteristic basis functions for solving large multiscale electromagnetic scattering problems,” *IEEE Transactions on Antennas and Propagation*, vol. 56, no. 4, pp. 999-1007, Apr. 2008, DOI:10.1109/TAP.2008.919166.
- [21] S. Rao, D. Wilton, and A. Glisson, “Electromagnetic scattering by surfaces of arbitrary shape,” *IEEE Transactions on Antennas and Propagation*, vol. 30, no.3, pp 409-418, May 1985, DOI:10.1109/TAP.1982.1142818.
- [22] Y. Chen and C. F. Wang, *Characteristic Modes: Theory and Applications in Antenna Engineering*. Hoboken, NJ, USA: Wiley, 2015.



Fei Guo received the B.E degree from Anqing Normal University in 2021. He is currently pursuing the M.S degree in Anhui University of Science and Technology. His current research interest includes computational electromagnetics.



Zhonggen Wang received the Ph.D. degree in electromagnetic field and microwave technique from the Anhui University of China (AHU), Hefei, P. R. China, in 2014. Since 2014, he has been with the School of Electrical and Information Engineering, Anhui University of Science and Technology. His research interests include computational electromagnetics, array antennas, and reflect arrays.



Wenyan Nie is a professor at Huainan Normal University. She received the B.S. and M.S degrees from Anhui University of Science and Technology in 2007 and 2012, respectively. Her research interests include computational electromagnetic methods, antenna theory and design.

Gain-enhanced and Mechanical Reconfigurable Slot Antenna with Metasurface

Xueyan Song, Ang Dong, Xuping Li, Yunqi Zhang, Haoyuan Lin, Yapeng Li, and Hailong Yang

School of Electronic Engineering
Xi'an University of Posts & Telecommunications, Xi'an, 710121, China
xysong65@xupt.edu.cn, 1361580350@qq.com, lixuping@163.com, johnny_5@126.com
2806198782@qq.com, liyapengedu@163.com, yanghl68@163.com

Abstract – A novel wideband slot antenna with metasurface is presented. In order to achieve broadband, high-gain, and mechanical reconfigurable performance, a metasurface is adopted and combined with a new-type planar slot antenna. The antenna and metasurface are designed on F4B substrate, and the overall dimension of the antenna is $1.48\lambda_0 \times 1.48\lambda_0 \times 0.2\lambda_0$ (λ_0 is the free space wavelength at center frequency). Different from the traditional square metasurface, a structure with different properties in the x and y directions is utilized in the proposed antenna, which can be reconstructed by adjusting the relative position between the slot antenna and the metasurface. By introducing the metasurface, the maximum gain of the whole antenna is improved. The antenna works in two states with respect to the two locations of the metasurface. The impedance bandwidth of the proposed antenna in state A is from 5.49 to 9.40 GHz (52.5%), and the impedance bandwidth of the proposed antenna in state B is from 5.83 to 6.01 GHz (3%) and 7.05 to 9.62 GHz (30.8%). The gain of the whole antenna in both states is higher than that of the original slot antenna (without metasurface), and the maximum gain is 9.1 dBi.

Index Terms – Metasurface, reconfigurable performance, slot antenna, wideband.

I. INTRODUCTION

Antennas with wideband, high-gain, and programmable properties have attracted significant attention from academics in the field of wireless communication due to the growing demand of wireless communication systems [1], [2]. Due to their ability to manipulate electromagnetic waves, metasurfaces have been designed to obtain various performances in antennas [3], [4]. Usually, the structure of reconfigurable antennas can be mechanical or electrical. Electrical reconfigurable antennas are popular, and their states can be switched by

PIN-diode switches [5], [6]. However, there are some problems to be solved. For example, the addition of electronic components may affect the performance of the antenna. The operation of the antenna depends on the reliability of the electronic components and the DC power supply [7].

The metasurface has been demonstrated in the literatures [8–12]. When combined with metasurface, the antenna can achieve reconfigurable performance. In [8], a polarization and frequency-reconfigurable antenna with metasurface was proposed to reconfigure the performance of the antenna by changing the relative positions of the metasurface and antenna layer. The antenna proposed in [8] can achieve a bandwidth of 8 to 11.2 GHz (33.33%). In [9], two layers of metasurfaces are loaded above the slot antenna, and the frequency reconfigurable characteristic is achieved by rotating the top metasurface with respect to the center of the slot antenna. The operating frequency band ranges from 2.55 to 3.45 GHz (28%). And the gain curve of the antenna ranges from 5.3 dBi to 8.3 dBi. Because it does not require additional biasing circuits or switches, the physical rotation technique is attractive, which is adopted in this paper to achieve radiation pattern and impedance bandwidth reconfiguration. Therefore, the state of the proposed design in this paper can be freely switched in the communication system to achieve interference immunity. Methods to improve the overall antenna gain by incorporating metasurfaces have been used extensively, such as using the metasurface as a reflector [10],[11] and using the metasurface as a secondary radiation source to modulate the beam [12]. Nevertheless, the bandwidth and the gain of the designed antenna needs to be further improved.

In this letter, an antenna that can achieve mechanical reconfigurability, gain enhancement, and wideband is proposed. The antenna consists of a metasurface and a slot antenna, which are connected by a nylon column. In order to enhance the gain, a metasurface structure is utilized under a broadband slot antenna. The metasurface

is composed of 66 units to achieve different responses to incident waves in x and y directions. To achieve broadband characteristic, some new structures such as gradual feeder line are introduced in the presented slot antenna. The proposed antenna operates in two radiation states by mechanical rotation, and gain of the proposed antenna can be enhanced in both states compared with the original slot antenna (without metasurface). The antenna in state A provides fractional bandwidths of 52.5% at 7.45 GHz, and the antenna in state B provides fractional bandwidths of 3% at 5.92 GHz and 30.8% at 8.34 GHz. And the maximum gain of proposed antenna can reach 9.1 dBi. All in all, the proposed antenna can achieve broadband, high-gain and mechanically reconfigurable characteristics.

II. ANTENNA DESIGN

A. Antenna configuration

The proposed antenna consists of a new slot antenna and a metasurface, as shown in Fig. 1. The antenna and the metasurface are printed on a 1 mm substrate with

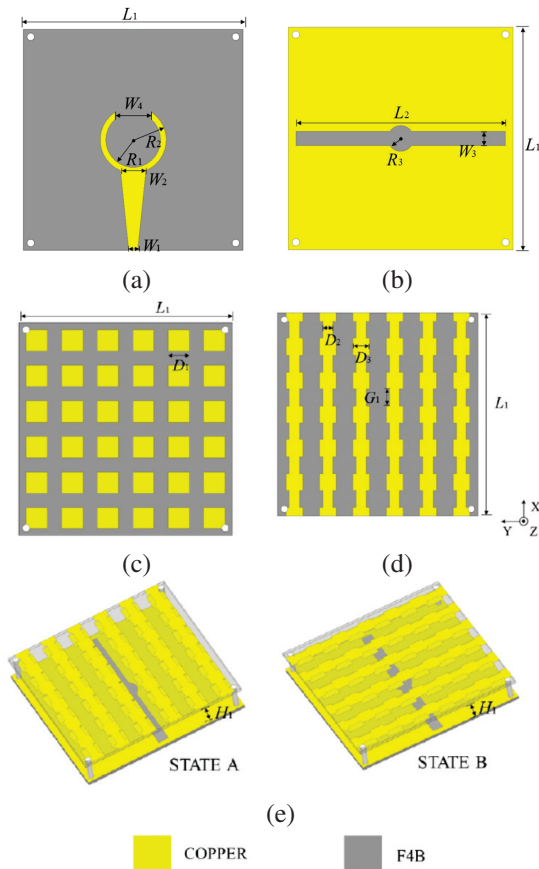


Fig. 1. (a) Feeder line of slot antenna, (b) surface of slot antenna, (c) bottom view, (d) top view of the metasurface, and (e) 3D geometry of proposed structure in states A and B.

Table 1: Dimensions of the proposed antenna (unit: mm)

Parameter	Value	Parameter	Value
L_1	60	L_2	56
R_1	7.5	R_2	9
R_3	3.5	W_1	2.4
W_2	6.95	W_3	1.9
W_4	10	D_1	6
D_2	3	D_3	5
G_1	5	H_1	8

a relative permittivity of 2.2 and loss tangent of 0.001. The antenna is on the top layer, and the metasurface is on the bottom layer. In order to improve the impedance bandwidth of the slot antenna, a new gradual feeder line, which splits at the end into a two-part circular arc and circular slot are designed, as shown in Figs. 1 (a) and (b). The metasurface is composed of 6×6 two-layer patch units, which are etched on the both sides of one substrate. The top patch layer is arranged by an inverted H-shaped patch unit in x and y directions and the bottom layer consists of a square patch. The units are designed as shown in Figs. 1 (c) and (d). By rotating the metasurface around the center with respect to the slot antenna, the reconfigurable characteristic of the proposed antenna can be achieved. The detailed operation of mechanical reconfiguration is achieved by manually adjusting the four nylon columns on the four corners of the substrates. When the four columns are unscrewed, the metasurface can be manually rotated by 90 degrees around the z -axis along the center, and then installed under the antenna, bringing in the switching between two states. The structure of the proposed antenna in two states is shown in Fig. 1 (e). The dimensions of the antenna are shown in Table 1.

B. Working mechanism

The characteristics of the proposed slot antenna and metasurface are simulated by using ANSYS HFSS. In order to obtain broadband characteristics of the slot antenna, the design of the feeder line is especially important. The impedance characteristics of the slot antenna can be greatly improved by the design of the tapering structure and the open ring. Therefore, of all the parameters, R_1 and W_1 make great contributions to the characteristics of the slot antenna. Figure 2 depicts the simulated S_{11} of the proposed antenna with different values of R_1 and W_1 . From Fig. 2 (a), it can be seen that when R_1 decreases, the resonance characteristics of the low frequency band become worse, when R_1 increases, mainly the resonance characteristics of the high frequency part become worse. when $R_1 = 7.5$ mm, the impedance bandwidth is the best, From Fig. 2 (b), it can be seen that when W_1 changes, there will be two frequency points

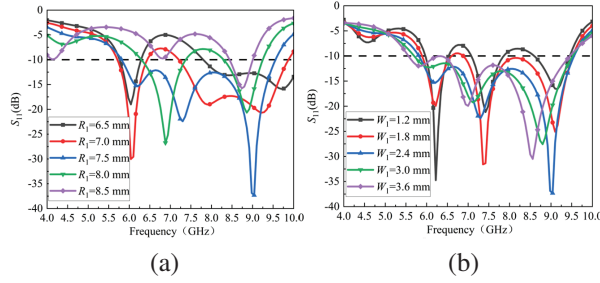


Fig. 2. Simulated S_{11} of the proposed slot antenna with different values of the main parameters including (a) R_1 , and (b) W_1 .

where the resonance performance becomes worse. When $W_1 = 1.8$ mm, the impedance bandwidth is optimal. To obtain good matching property, it reaches a compromise to choose the value R_1 as 7.5 mm and W_1 as 2.4 mm.

As mentioned above, the reconfigurability of the antenna results from the units of the metasurface. When the metasurface and the antenna are in two different relative positions, the metasurface can achieve transmission and reflection performance, respectively. The units of the metasurface are shown in Figs. 3 (a) and (b). In order to investigate properties of the metasurface, the unit cell is simulated by the simulation software ANSYS HFSS, and the simulation model is shown in Fig. 3 (c). The unit is imposed by the Master-Slaver boundary conditions and excited by the Floquet ports. With this electromagnetic simulation method, the response characteristics

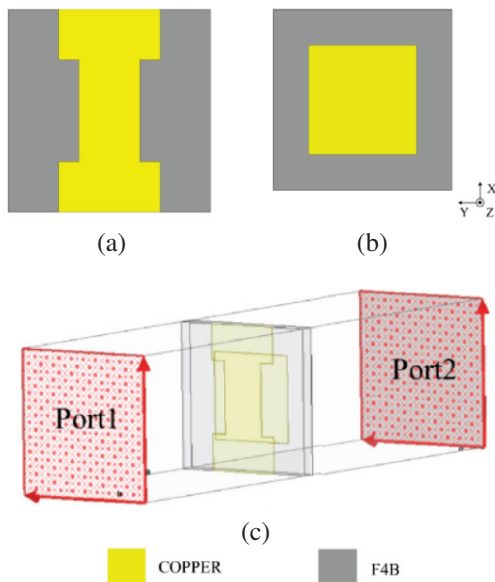


Fig. 3. (a) Top view of the unit cell, (b) bottom view of the unit cell and (c) the simulation model of the proposed unit cell of the metasurface.

of the metasurface with infinitely large dimensions can be simulated and thus save computational resources.

For different incident waves in x -polarized and y -polarized directions, the metasurface works in a different state. When the incident wave is x -polarized, the metasurface is reflective, which is defined as state A; and when the incident wave is y -polarized, the metasurface is transmissive, which is defined as state B. When in state A, electromagnetic energy is reflected from the metasurface and superimposed, which contributes to the improvement of the maximum gain. And when in state B, the aperture of the antenna is increased by the addition of a metasurface, which narrows the beam and raises maximum gain.

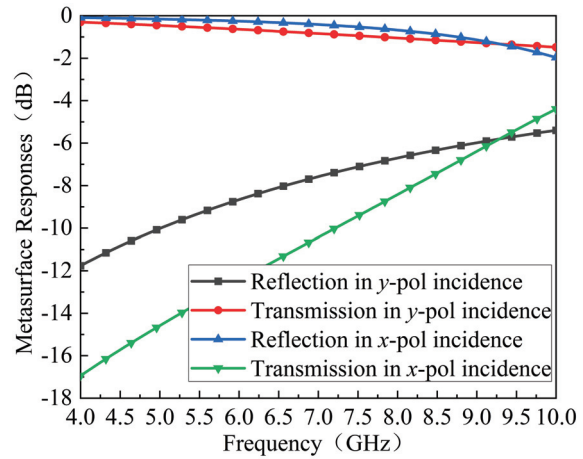


Fig. 4. Simulated reflection and transmission coefficients of metasurface.

The response of the metasurface from the incident x -polarized wave and y -polarized wave is shown in Fig. 4. It can be seen from the blue curve in Fig. 4, when the incident electromagnetic wave is x -polarized, the metasurface reflects the majority of the energy. From the red curve in Fig. 4, it can be obtained that the metasurface transmits most of the energy when the incident electromagnetic wave is y -polarized. Due to the different performances of the metasurface in two states, the proposed antenna in this work can achieve various characteristics.

In order to investigate the influence of the metasurface on the original slot antenna, the proposed combined antenna at 6.5 GHz in two states is taken as an example. And Fig. 5 depicts the electric field intensity distribution of the antenna in both states, from which it can be determined that the electric field intensity distribution the both sides of the slot and terminal feeder line are different. That is because the addition of the metasurface changes the electromagnetic environment around the slot antenna. When operating in state A, the slot antenna

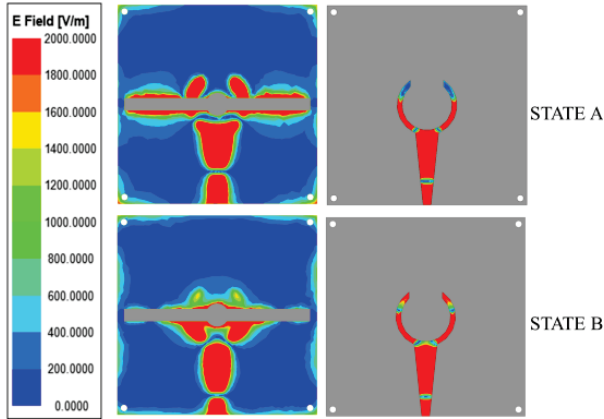


Fig. 5. Electric field distributions in states A and B at 6.5 GHz.

around the electromagnetic energy is scarcely affected because the metasurface is transmissive, bringing in the similar frequency response between the whole antenna in state A and the original slot antenna (without metasurface). In state B, the metasurface reflects the energy initially radiated in the $+z$ direction. The reflected energy is then excited again on the terminal feeder line of the slot antenna, which results in the difference in reflection coefficient between the whole antenna in state B and the original slot antenna at 6.5 GHz.

III. SIMULATED RESULTS

The simulated S_{11} and radiation efficiency of the original proposed slot antenna (without metasurface) and the whole antenna in states A and B are shown in Fig. 6. It can be seen that the original slot antenna operates in the band between 5.81 GHz and 9.56 GHz (48.8%). The bandwidth of the whole antenna in state A is from 5.49

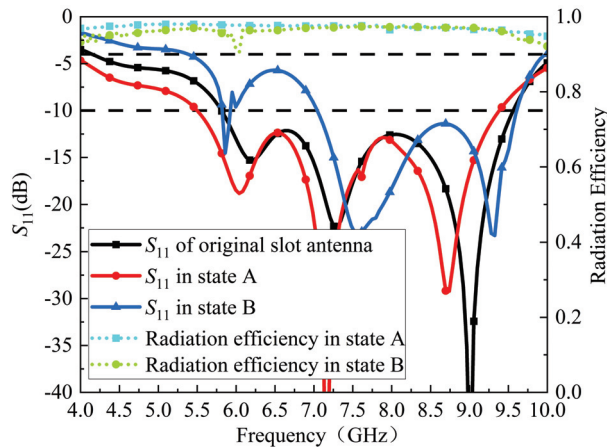


Fig. 6. Simulated S_{11} and radiation efficiency of the proposed original slot antenna and the slot antenna with metasurface in two states.

GHz to 9.40 GHz (52.5%). The bandwidth of the whole antenna in state B is 5.83 GHz to 6.01 GHz (3.0%) and 7.05 GHz to 9.62 GHz (30.8%). And the radiation efficiency of the proposed antenna is greater than 90% in two states.

Figure 7 depicts the radiation patterns in xoz and yoz plane of the original slot antenna, and the whole antenna in state A and state B at 6 GHz, 7.5 GHz, and 9 GHz. As shown in Fig. 7, the maximum gain of the antenna in both state A and state B is higher than that of the original slot antenna. Moreover, it can also be seen that the addition of the metasurface makes the original slot antenna generate two radiation patterns, which brings in reconfigurable achievement. Table 2 demonstrates the increase in maximum gain of the proposed antenna at the three frequency points. It can be found that, with the metasurface, the proposed slot antenna can achieve significantly

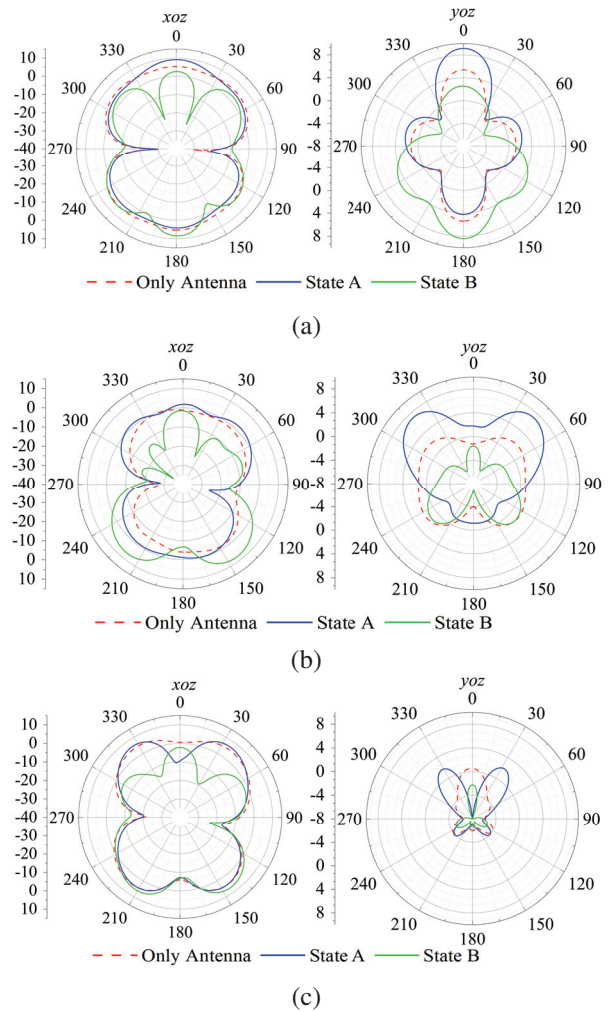


Fig. 7. The simulated radiation patterns of the proposed slot antenna with and without metasurface at (a) 6 GHz, (b) 7.5 GHz, and (c) 9 GHz.

Table 2: Gain enhancement effect (unit: dBi)

Frequency (GHz)	Only Antenna	State A	State B	State A Enhance	State B Enhance
6	5.6	9.1	8.4	3.5	2.8
7.5	3.4	7.1	7.7	3.7	4.3
9	5.8	6.7	8.1	0.9	2.3

more gain improvement than the original slot antenna. The maximum gain of the slot antenna with metasurface can reach 9.1 dBi.

IV. EXPERIMENTAL RESULTS

To verify the antenna performance, a prototype of the same size as in Table 1 is fabricated and measured. The specific appearance is shown in Fig. 8. For easy switching between state A and state B, four nylon columns are fixed to connect the antenna and the metasurface. The reflection coefficient is measured by Keysight E5063A network analyzer.

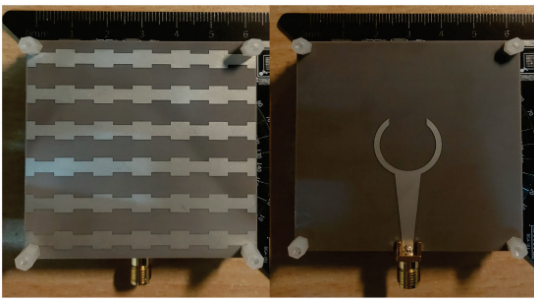


Fig. 8. Front and back sides of the prototype.

The simulated and measured S_{11} in state A and state B are depicted in Fig. 9. It can be seen that the measured results are in good accordance with the simulated ones except for small deviations in operating frequencies, which are mainly due to fabrication and experimental tolerances. The operating bandwidth of the antenna in state A is from 5.41 GHz to 9.55 GHz (55.35%). The operating band of the antenna in state B ranges from 5.95 GHz to 6.13 GHz (3%) and from 7.03 GHz to 9.87 GHz (33.6%). The radiation patterns are measured in the microwave lab. The simulated and measured radiation patterns of the proposed antenna in state A and B in xoz and yoZ plane at 8 GHz are shown in Fig. 10. The proposed antenna exhibits different radiation characteristics in different states and realizes the reconfigurable characteristics in the radiation patterns. In the xoz plane, the cross-polarization is less than -30 dB. The cross-polarization level in the yoZ plane is small in the direction of maximum radiation and does not affect communication. The little difference between the measured and the

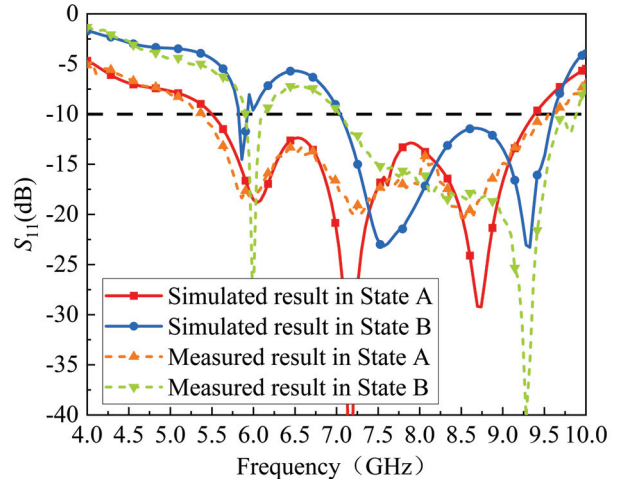
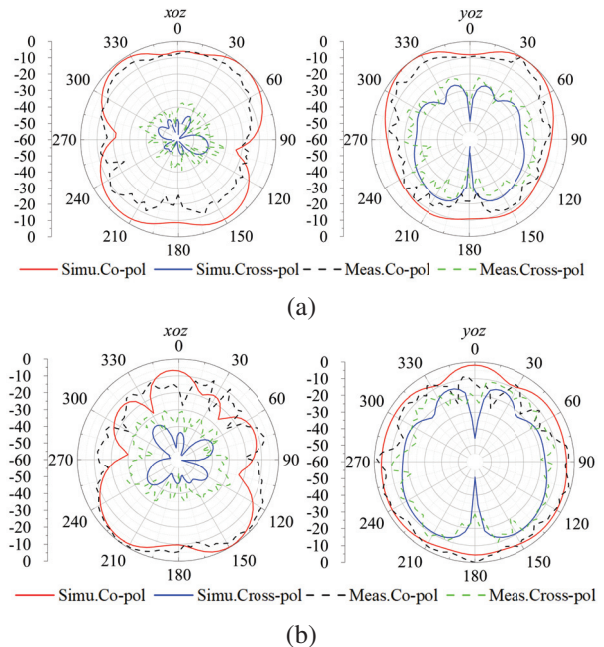
Fig. 9. Simulated and measured S_{11} of the proposed antenna in state A and state B.

Fig. 10. Simulated and measured radiation patterns of the proposed antenna at 8 GHz in (a) state A and (b) state B.

simulated results is mainly due to the measure environment and manufacturing errors.

The performances of the proposed antenna compared with that of antennas are illustrated by Table 3 in references. Compared with [4], [7], and [9–11], the proposed antenna has a wider bandwidth and high gain. Compared with [8], the dimension of the proposed antenna is smaller and the bandwidth is wider. In conclusion, the proposed antenna can achieve broadband, high-gain, and reconfigurable characteristics.

Table 3: Comparison of the proposed antenna and references

References	Bandwidth (%)	Gain (dBi)	Overall size ($\lambda 0$)	Whether Reconfigurable
[4]	23.6	8.1	$0.78 \times 0.78 \times 0.038$	no
[7]	14.6	5	$0.67 \times 0.67 \times 0.05$	yes
[8]	33.33	16.5	$2.56 \times 2.56 \times 0.93$	yes
[9]	28	8.3	$1 \times 1 \times 0.07$	yes
[10]	40	9.9	$1.2 \times 1.2 \times 0.12$	no
[11]	43.1	6.12	$0.348 \times 0.348 \times 0.07$	No
This work	52.5	9.1	$1.48 \times 1.48 \times 0.2$	yes

V. CONCLUSION

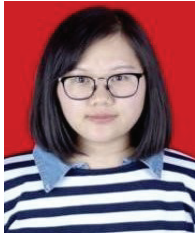
In this paper, a reconfigurable, high-gain, and wide-band slot antenna with metasurface is designed and fabricated, and two radiation states can be realized by physically rotating the metasurface. The impedance bandwidth of the proposed antenna in state A is from 5.49 GHz to 9.40 GHz (52.5%), and the impedance bandwidth of the proposed antenna in state B is from 5.83 GHz to 6.01 GHz (3%) and from 7.05 GHz to 9.62 GHz (30.8%), and the maximum gain reaches 9.1 dBi. The measured results agree well with the simulated ones, which validates that the antenna has the advantages of large bandwidth, high gain, and reconfigurable performance. Therefore, the proposed antenna can be utilized in C and X bands for high-capacity microwave communication, such as satellite communication and medical service.

ACKNOWLEDGMENT

This work was supported by the Natural Science Basic Research Program of Shaanxi (Program Nos. 2022JQ-699, 2022JQ-633, and 2021JQ-710) and the Key Research and Development Program of Shaanxi (Program No. 2021GY-049).

REFERENCES

- [1] H. Li, G. Wang, X. Gao, J. Liang, and H. Hou, "A novel metasurface for dual-mode and dual-band flat high-gain antenna application," *IEEE Transactions on Antennas and Propagation*, vol. 66, pp. 3706-3711, July 2018.
- [2] B. Heydari, A. Afzali, and H. R. Goodarzi, "A new ultra-wideband omnidirectional antenna [antenna designer's notebook]," *IEEE Antennas and Propagation Magazine*, vol. 51, no. 4, pp. 124-130, Aug. 2009.
- [3] D. Chen, W. Yang, Q. Xue, and W. Che, "Miniaturized wideband planar antenna using interembedded metasurface structure," *IEEE Transactions on Antennas and Propagation*, vol. 69, no. 5, pp. 3021-3026, May 2021.
- [4] J. Zhu, G. Zhang, Z. Li, Z. Che, J. Yue, Y. Feng, Q. Zhang, and R. Qiu, "A high-gain, low-profile filtering antenna based on a novel metasurface," *Applied Computational Electromagnetics (ACES) Journal*, vol. 37, no. 11, pp. 1153-1161, Apr. 2023.
- [5] Y. Liu, W. Zhang, Y. Jia, and A. Wu, "Low RCS antenna array with reconfigurable scattering patterns based on digital antenna units," *IEEE Transactions on Antennas and Propagation*, vol. 69, no. 1, pp. 572-577, Jan. 2021.
- [6] M. Shirazi, J. Huang, T. Li, and X. Gong, "A switchable-frequency slot-ring antenna element for designing a reconfigurable array," *IEEE Antennas and Wireless Propagation Letters*, vol. 17, no. 2, pp. 229-233, Feb. 2018.
- [7] H. L. Zhu, X. H. Liu, S. W. Cheung, and T. I. Yuk, "Frequency-reconfigurable antenna using metasurface," *IEEE Transactions on Antennas and Propagation*, vol. 62, no. 1, pp. 80-85, Jan. 2014.
- [8] C. Ni, M. S. Chen, Z. X. Zhang, and X. L. Wu, "Design of frequency-and polarization-reconfigurable antenna based on the polarization conversion metasurface," *IEEE Antennas and Wireless Propagation Letters*, vol. 17, no. 1, pp. 78-81, Jan. 2018.
- [9] B. Majumder, K. Krishnamoorthy, J. Mukherjee, and K. P. Ray, "Frequency-reconfigurable slot antenna enabled by thin anisotropic double layer metasurfaces," *IEEE Transactions on Antennas and Propagation*, vol. 64, no. 4, pp. 1218-1225, Apr. 2016.
- [10] Z. Jiang, Z. Wang, L. Nie, X. Zhao, and S. Huang, "A low-profile ultrawideband slotted dipole antenna based on artificial magnetic conductor," *IEEE Antennas and Wireless Propagation Letters*, vol. 21, no. 4, pp. 671-675, Apr. 2022.
- [11] D. Feng, H. Zhai, L. Xi, S. Yang, K. Zhang, and D. Yang, "A broadband low-profile circular-polarized antenna on an AMC reflector," *IEEE Antennas and Wireless Propagation Letters*, vol. 16, pp. 2840-2843, 2017.
- [12] D. Chen, Q. Xue, W. Yang, K.-S. Chin, H. Jin, and W. Che, "A compact wideband low-profile metasurface antenna loaded with patch-via-wall structure," *IEEE Antennas and Wireless Propagation Letters*, vol. 22, no. 1, pp. 179-183, Jan. 2023.



Xueyan Song was born in Henan Province, China, 1989. She received the B.E. degree in electronic and information engineering from Xidian University, Xi'an, China, in 2012. She received the Ph.D. degree from Xidian University, Xi'an, China, in 2018. She joined the School of Electronic Engineering, Xi'an University of Posts and Telecommunications in 2018. Her research interests include artificial magnetic conductors, low RCS antennas, low-profile antennas, frequency selective surfaces, and reflector antennas.



Ang Dong was born in Hebei, China, in 1999. He is currently pursuing a Master of Engineering degree in the School of Electronic Engineering, Xi'an University of Posts and Telecommunications. His current research interests include metasurface, microstrip antennas.



Xuping Li was born in Xi'an, Shanxi, China in 1981. He received the Ph.D. degree in electromagnetic field and microwave from the Xidian University, Xi'an, China in 2015. In January 2019, he was transferred to Xi'an University of Posts and Telecommunications as the leader of the phased array antenna technology research team. The principal focus of his research program is the development of phased array antennas.



Yunqi Zhang was born in BaoTou, Inner Mongolia, China, in 1986. He received the Ph.D. degree from Xidian University, Xi'an, China in 2015. He is currently working in the Xi'an University of Posts & Telecommunications. His research interests include GPS antennas, CP antennas, omnidirectional antennas, and antenna array designs.



Haoyuan Lin was born in Shandong, China, in 2003. He is currently pursuing a B.E. degree in the school of Electronic Engineering from Xian University of Posts and Telecommunications. His current research interests include circuits, microwave, antennas.



Hailong Yang received the B.S. in communicating engineering from Heze University, Heze, China, in 2012, M.S. and Ph.D. degrees in communicating engineering from Xi'an University of Technology, Xi'an, China, in 2015 and 2019. He joined the faculty of Electronic Engineering Department, Xi'an University of Posts&Telecommunications, in 2019. His research interests include wave propagation and antenna design.



Yapeng Li received the Doctor's degree from Xidian University in 2020. He is currently an associate professor with the School of Electric Engineering, Xi'an University of Post and Telecommunications. His research interests include filtering antennas, wideband antennas, dual-polarized antennas and circular polarized antennas.

Wideband Monostatic RCS Prediction of Complex Objects using Support Vector Regression and Grey-wolf Optimizer

Zhourui Zhang¹, Pengyuan Wang^{2,3}, and Mang He³

¹School of Integrated Circuits and Electronics
Beijing Institute of Technology, Beijing, 100081, China
3120215371@bit.edu.cn

²School of Integrated Circuits and Electronics
Beijing Institute of Technology, Beijing, 100081, China
3120205355@bit.edu.cn

³School of Integrated Circuits and Electronics
Beijing Institute of Technology, Beijing, 100081, China
hemang@bit.edu.cn

Abstract – This paper presents a method based on the support vector regression (SVR) model and grey wolf optimizer (GWO) algorithm to efficiently predict the monostatic radar cross-section (mono-RCS) of complex objects over a wide angular range and frequency band. Using only a small-size of the mono-RCS data as the training set to construct the SVR model, the proposed method can predict accurate mono-RCS of complex objects under arbitrary incident angle over the entire three-dimensional space. In addition, the wideband prediction capability of the method is significantly enhanced by incorporating the meta-heuristic algorithm GWO. Numerical experiments verify the efficiency and accuracy of the proposed SVR-GWO model over a wide frequency band.

Index Terms – Complex objects, grey wolf optimizer, machine learning, radar cross-section, support vector regression.

I. INTRODUCTION

Radar cross-section (RCS) is one of the most important concepts in radar stealth technology [1], and the traditional methods for RCS estimation can be divided into two categories. One type is the full-wave numerical method, which has high accuracy but is time-consuming and computationally expensive. The other one is the high-frequency approximate method, which is fast but precision-limited. A common shortage of these methods is the incapability to accomplish the RCS of radar targets in real-time, especially for the monostatic RCS (mono-RCS) prediction of complex objects because it usually takes long computation time for each incident

angle repeatedly. Therefore, new approaches are required to address the problem of real-time mono-RCS computation.

Due to the regression capability of nonlinear fitting and generalization ability, machine learning (ML) has recently been applied in solving computational electromagnetics (EM) problems. An essential benefit of ML is that once the relationship has been established between the input and output spaces, the results for any other given inputs can be predicted instantaneously, which could save computation resources massively. Researchers have proposed ML models for EM solver design [2], repairing damaged receivers' data [3], and low scattering meta-surface design [4], etc. ML has also been applied in RCS prediction [5–10], but the existing techniques still have some limitations. For instance, 8326 samples are required for a single frequency point in [5], which may not be applicable for computationally expensive EM problems. The ML models in [6, 7] are effective only when the direction of the incident wave varies in one direction (θ or φ direction), which ignore the mono-RCS variation in the entire space. The physics-inspired model in [9] is suitable for the mono-RCS estimation at a single frequency point, while its wideband performance is not further considered. [10] discusses the RCS prediction over a wide frequency band, but the aspect angle variation range is only 10 degrees, and the sampling interval is very close (0.2-degree step), which results in massive computational costs. To the best of our knowledge, few works have been found to solve the problem of fast and accurate mono-RCS prediction in real-time using ML over a wide range of incident angles and wide frequency bands simultaneously.

This work proposes an alternative method that combines the support vector regression (SVR) model and grey-wolf optimizer (GWO) [11] to predict the mono-RCS of complex targets under any incident angle over a wide frequency band. The proposed method employs the SVR model to establish the approximate function between mono-RCS and incident angle and frequency, i.e., RCS (θ, φ, f) . The metaheuristic algorithm GWO is applied to accomplish the parameter optimization of the SVR model and achieves better prediction ability in comparison with other metaheuristic algorithms. Unlike the existing deep learning (DL) algorithms that need enormous datasets, the new SVR-GWO model achieves high-accuracy prediction and has robust generalization to unknown samples by using small-sized training datasets, which is crucial for mono-RCS prediction of complex targets that need extensive computation. With a well-trained SVR-GWO model, for arbitrary angle of incidence, the mono-RCS of complex targets over a wide frequency band can be predicted with good accuracy almost in real time.

II. SVR-GWO METHOD

In order to achieve fast prediction of wideband mono-RCS of complex targets under the arbitrary incident angle, the SVR model representing the nonlinear relationship between the mono-RCS and input parameters, i.e., the operating frequency f and the angle of incidence (θ, φ) , should be first constructed. Typical mono-RCS data need to be sampled within the target frequency band and angular range, and the approximation function of the mono-RCS and input parameters can be represented [12] as:

$$f(\mathbf{x}_i) = \mathbf{w}^T \phi(\mathbf{x}_i) + b, \quad (1)$$

where $\phi(\mathbf{x}_i)$ is the nonlinear function of the input parameter vector \mathbf{x}_i that consists of f , θ , and φ , and $f(\mathbf{x}_i)$ is the output of the SVR model; i.e. the predicted value of mono-RCS for the target. \mathbf{w}^T and b are weight and bias vectors, respectively.

As shown in Fig. 1, the SVR model assumes that a deviation of at most ε between the predicted value of the mono-RCS and its true value (obtained from accurate numerical calculations) can be tolerated, which is called the ε -tube. The slack variable ξ is often introduced to measure the deviation of data points beyond the ε -tube, representing a soft margin that the SVR model allows some samples not to satisfy the constraints [13]. Thus, the SVR model aims to optimize the following constrained target function [12]:

$$\begin{aligned} \min_{\mathbf{w}, b} \quad & \frac{1}{2} \|\mathbf{w}\|_2^2 + C \sum_{i=1}^n (\xi_i^V + \xi_i^\wedge), \\ \text{s.t.} \quad & -\varepsilon - \xi_i^V \leq |y_i - (\mathbf{w}^T \phi(x_i) + b)| \leq \varepsilon + \xi_i^\wedge, \\ & \xi_i^V \geq 0, \xi_i^\wedge \geq 0, \quad i = 1, 2, 3 \dots n, \end{aligned} \quad (2)$$

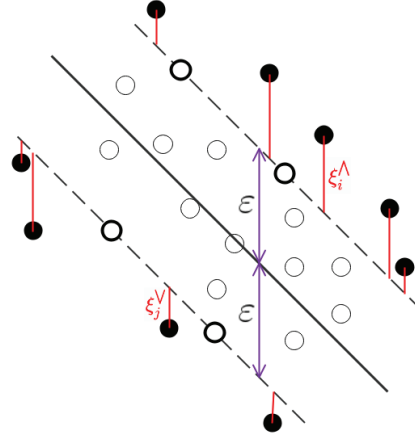


Fig. 1. Diagram of the SVR model.

where y_i is the true value of mono-RCS, and C is a constant called the penalty parameter. When C is infinitely large, equation (2) forces all samples to fulfill constraints but tends to cause the model overfitting. If C has a finite value, the model allows some samples not to fall into the ε -tube, and the variables ξ_i^V and ξ_i^\wedge determine the allowable deviation below and above the ε -tube, respectively.

The constrained optimization problem can be reformulated into a pairwise problem form using the *Lagrangian* multiplier approach. By doing so, the correlation of the input and output of the SVR model [12] becomes:

$$f(\mathbf{x}_i) = \sum_{i=1}^N (\alpha_i, \alpha_i^*) K(x, x_i) + b, \quad (3)$$

where α_i and α_i^* are the *Lagrangian* multipliers. $K(x, x_i)$ is the kernel function, representing the inner product of x_i and x_j in their feature space $\phi(x_i)$ and $\phi(x_j)$.

In this paper, the radial basis function (RBF) [12] is chosen as the kernel function due to its capability for nonlinear fitting and relatively fewer parameters:

$$K(x_i, x_j) = \exp(-\gamma \|x_i - x_j\|^2). \quad (4)$$

Once the SVR model is constructed, its accuracy should be verified by the validation set. The coefficient of determination R^2 defined in [14] is applied to measure the goodness of the SVR model:

$$R^2 = 1 - \frac{\sum_i (y_i - \hat{y}_i)^2}{\sum_i (y_i - \bar{y})^2}, \quad (5)$$

where \hat{y}_i is the predicted mono-RCS, and \bar{y} is the mean of the true value of mono-RCS y_i . Apparently, the range of R^2 is $[0, 1]$, and the higher the value is, the better the model fits.

As mentioned before, the penalty parameter C and threshold tolerance ε are crucial for constructing a high-precision SVR model and must be pre-determined before applying the *Lagrangian* multiplier approach. Similarly,

the parameter γ in the kernel RBF should also be predetermined. In this paper, the recently proposed GWO algorithm [11] is utilized to optimize the parameters of the SVR model for better performance, and the optimal solution of the target function R^2 is obtained by parameter search within the range of values of the input parameters C , ε , and γ .

The GWO algorithm mimics the leadership hierarchy and hunting mechanism of grey wolves in nature. A wolf pack is created and is used to search for the optimal solution. In the first iteration, each individual's position, i.e., the values of input parameters, are randomly allocated, and the corresponding R^2 is calculated and ranked. Wolf α , β , δ are assumed to learn better about the position of the optimal solution and keep the best three solutions for the current iteration. Other individuals search for the position of the better solution based on the positions of the best three solutions [11] by

$$\begin{cases} \vec{D}_\alpha = |\vec{C}_1 \cdot \vec{X}_\alpha - \vec{X}(t)| \\ \vec{D}_\beta = |\vec{C}_2 \cdot \vec{X}_\beta - \vec{X}(t)| \\ \vec{D}_\delta = |\vec{C}_3 \cdot \vec{X}_\delta - \vec{X}(t)| \end{cases}, \quad (6)$$

$$\begin{cases} \vec{X}_1 = \vec{X}_\alpha - \vec{A}_1 \cdot \vec{D}_\alpha \\ \vec{X}_2 = \vec{X}_\beta - \vec{A}_2 \cdot \vec{D}_\beta \\ \vec{X}_3 = \vec{X}_\delta - \vec{A}_3 \cdot \vec{D}_\delta \end{cases}, \quad (7)$$

$$\vec{X}(t+1) = \frac{\vec{X}_1 + \vec{X}_2 + \vec{X}_3}{3}, \quad (8)$$

where t means the iteration number, and \vec{A}_i and \vec{C}_i ($i = 1, 2, 3$) are the vectors of coefficients. \vec{A}_i is a random vector with its entry being in the range of $[-2, +2]$ and gradually shrinks toward 0 with iterations. When $|\vec{A}_i| < 1$, the individual approaches the target position; otherwise, the individual is forced to search for the more suitable position. \vec{C}_i is a random vector with its entry being between 0 and 2, and \vec{X} is each individual's position vector, representing the values of input parameters. \vec{X}_k ($k = \alpha, \beta, \delta$) denotes the position of the best three solutions, and \vec{D}_k means the distance between the individual's position and the position of the best three solutions. The search and individual sorting are repeated until the error is satisfied or the maximum number of iteration steps is reached. The final position of the wolf α , which is the optimal solution of the input parameters in their domain, is returned.

The flowchart of the proposed SVR-GWO method is shown in Fig. 2. It starts from the construction of the SVR model, then hyperparameters of the SVR model are tuned by the GWO algorithm. By evaluating the coefficient of determination for each individual, optimal

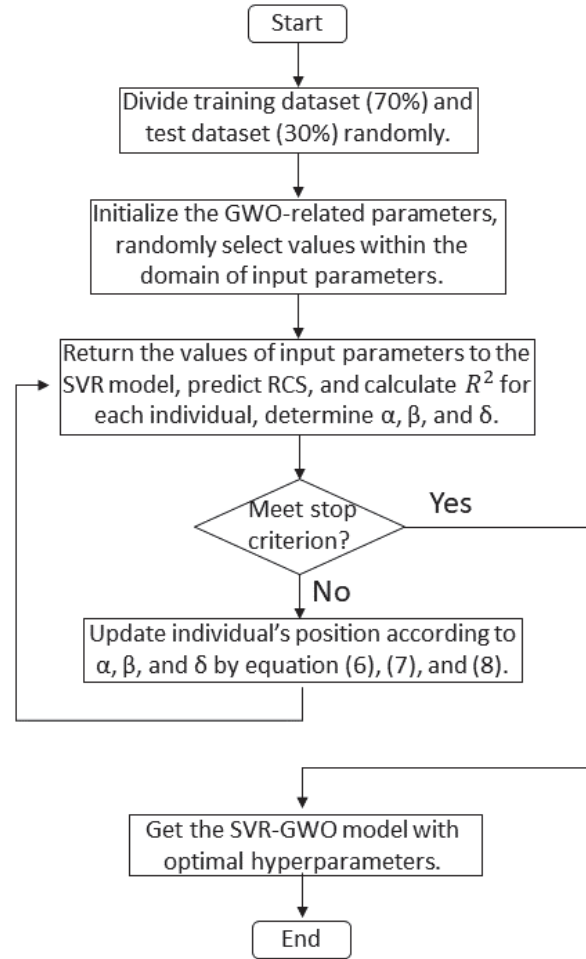


Fig. 2. Flowchart of the SVR-GWO method.

hyperparameters are selected to update the SVR model until reaching the final convergence.

III. NUMERICAL VALIDATION

In this section, the predicted mono-RCS of complex targets by the SVR-GWO method are compared with the true values from full-wave numerical calculations to evaluate the accuracy and effectiveness of the proposed model. The sampling datasets are achieved by an in-house multilevel fast multipole algorithm (MLFMA) accelerated volume-surface integral equation (VSIE) solver (referred to as the VSIE-MLFMA hereinafter) [15], and the computing platform is a personal computer with an Intel i5-10400 2.9 GHz CPU and 16 GB RAM. The proposed method is implemented in PyCharm.

A. Mono-RCS of a missile model

The geometry of the perfect electric conductor (PEC) missile model is shown in Fig. 3 (a), and it is

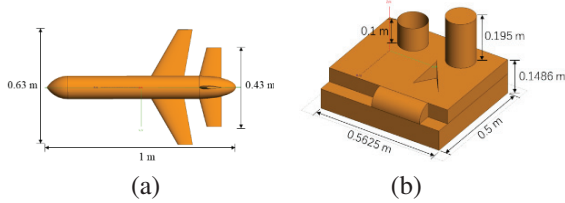


Fig. 3. The geometries of two numerical models: (a) missile and (b) SLICY.

illuminated by a vertically polarized plane wave with a frequency varying from 0.3 to 0.7 GHz. The predicted mono-RCS of the missile model at 0.6 GHz is first used to demonstrate the accuracy of the SVR-GWO method for single frequency point. Figure 4 shows good agreement between predicted values and true values in a wide angular range. The wideband performance of the proposed method is verified in Fig. 5, in which the comparison of the mono-RCS between predicted values and true values is shown at four different frequencies (0.325, 0.425, 0.575, and 0.675 GHz). For the training and testing datasets of the model, the sampling interval of incident angle in both θ and φ directions is 3° , with θ varying from 0° to 90° , and φ varying from 0° to 360° in the single frequency case and from 0° to 180° in the wideband case; the sampling interval of frequency is 0.05 GHz. In all cases, 70% of sampling data are used for training, and 30% are used for testing. Therefore, the sizes of sampling datasets are 3751 in the single frequency case and 17,019 in the broadband prediction, respectively.

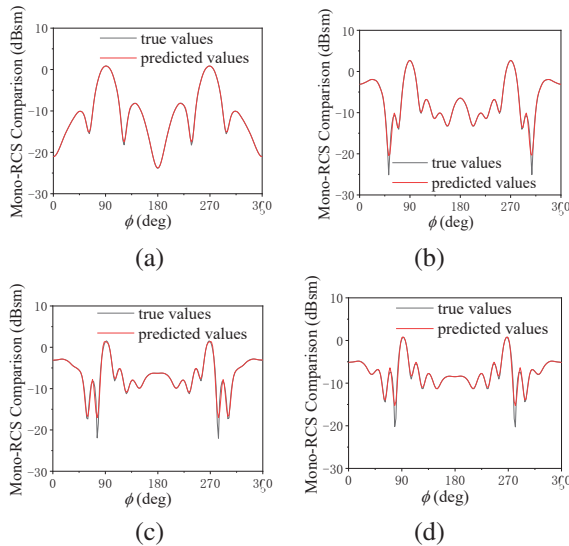


Fig. 4. Comparison of the predicted mono-RCS with the true values at 0.6 GHz for fixed elevation angles (a) $\theta = 30^\circ$, (b) $\theta = 50^\circ$, (c) $\theta = 70^\circ$, and (d) $\theta = 80^\circ$.

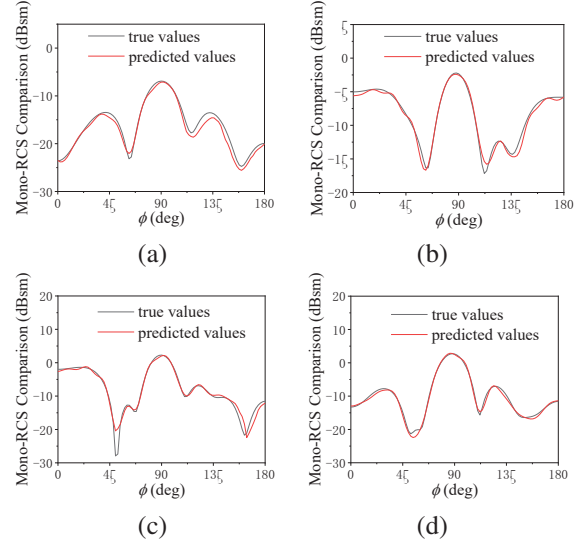


Fig. 5. Comparison of the predicted mono-RCS of the missile model and the true values under different incident angles at various frequencies: (a) $\theta = 75^\circ, f = 0.325$ GHz, (b) $\theta = 60^\circ, f = 0.425$ GHz, (c) $\theta = 48^\circ, f = 0.575$ GHz, and (d) $\theta = 36^\circ, f = 0.675$ GHz.

The root mean square error (RMSE) [16] is used to evaluate the prediction performance of the SVR-GWO model, which is defined as:

$$RMSE = \sqrt{\frac{1}{n} \sum_{i=1}^n (\hat{y}_i - y_i)^2}. \quad (9)$$

The RMSE and the cost time of the missile model were also calculated using following methods: The SVR model optimized by particle swarm optimizer (PSO); the SVR model without any optimizer; the backward propagation (BP) neural network [5–7]; the Gaussian process regression (GPR) model [8]; the polynomial chaos expansion (PCE) [17], and the low rank approximation (LRA) [18].

The comparison of different models is given in Table 1. The results prove the prediction accuracy and

Table 1: Comparison of RMSE and cost time with different models

Models	RMSE (dBsm)	Cost Time (s)
Proposed method	1.48	21,711
SVR-PSO	2.17	89,568
SVR	3.99	N/A
BP neural network	2.51	51,84
GPR	1.71	13,053
PCE	3.41	1,673
LRA	5.10	476

the efficacy of the proposed method. The RMSE of the SVR-GWO model is 62.9% and 31.8% lower than those of the SVR and the SVR-PSO models, respectively, and the training time is reduced by 75.8%. Compared with algorithms in similar literatures or other ML benchmark techniques, the RMSE of the missile model is also reduced from 13% to 71%.

To evaluate the regression performance of the SVR-GWO model, Figs. 6 and 7 (a) show the deviation of the predicted mono-RCS of the missile model from the accurate ones by the VSIE-MLFMA solver at a single frequency (0.6 GHz) and at four typical frequencies (0.325, 0.425, 0.575, and 0.675 GHz) within a wide frequency band. Two types of validation datasets of the same size (2024) are used in Fig. 6. One dataset is generated by using uniform sampling, and the other one is obtained from random sampling. The RMSEs of the uniform and random samplings are 0.65 and 0.92 dBsm, respectively, while the training time used in both sampling schemes is almost the same (900 seconds). The results clearly indicate that the uniform sampling scheme is better for the proposed model. Numerical simulations also show that once the SVR-GWO model is well trained, it can predict the mono-RCS of over 2000 samples per second, which means nearly real-time RCS calculation capability.

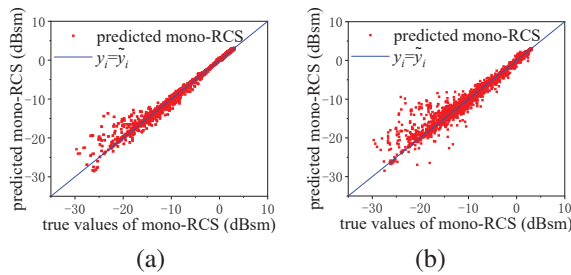


Fig. 6. Deviation of the predicted values from the accurate mono-RCS of the missile at a single frequency: (a) Uniform sampling and (b) random sampling.

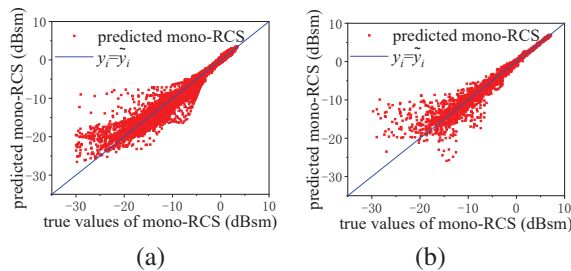


Fig. 7. Deviation of the predicted values from the accurate mono-RCS of complex targets within a wide frequency band: (a) Missile model and (b) SLICY model.

B. Mono-RCS of the SLICY model

The geometry of the second example (a PEC SLICY [19] model), is shown in Fig. 3 (b), and a vertically polarized plane wave illuminates the target with the frequency varying from 0.6 to 1.4 GHz. To obtain the dataset used for training and testing, the sampling interval of frequency is 0.1 GHz. At each sampling frequency, the incident angles in both θ and φ directions vary from 0° to 90° with a 3° sampling interval. 70% of the samplings are used for training, and 30% are used for testing. Therefore, the size of the dataset is 8649.

Table 2: Comparison of RMSE and cost time with different models

Models	RMSE (dBsm)	Cost Time (s)
Proposed method	1.42	7,600
SVR-PSO	1.75	16,933
SVR	2.28	N/A
BP neural network	3.26	3,167
GPR	2.24	5,573
PCE	4.19	1,254
LRA	3.33	423

The mono-RCS values at four typical working frequencies (0.65, 0.75, 1.15, and 1.35 GHz) are selected for validation. For each frequency point, the incident angles θ and φ run from 0° to 90° , and the sampling interval in θ and φ directions are 3° and 1° , respectively. So the size of the validation dataset is 11,284. A comparison of the results between the RCS predicted by the SVR-GWO model and those calculated by the VSIE-MLFMA solver is shown in Fig. 8, and the predicted results are found in good agreement with the accurate values.

Table 2 gives the RMSE and cost time comparison of different models. The RMSE of the SVR-GWO is 37.7% and 18.8% lower than those of the SVR and the SVR-PSO models, respectively, and the training time is reduced by 55.1%. It is seen that as the size of training data increases, the convergence speed of the GWO is faster compared to the PSO. Compared with algorithms in similar literatures or other ML benchmark techniques, the RMSE of the SLICY model is reduced from 36.6% to 66.1%. Figure 7 (b) illustrates the regression performance of the SVR-GWO model for the validation datasets of the SLICY model; again, the results indicate high prediction accuracy of the proposed method.

In Table 3, the mono-RCS prediction capability of the proposed method for a single frequency point is compared with the physical-optics-inspired (POI) SVR [9], which is a physical-inspired method. As shown in the table, for mono-RCS prediction of target at a single

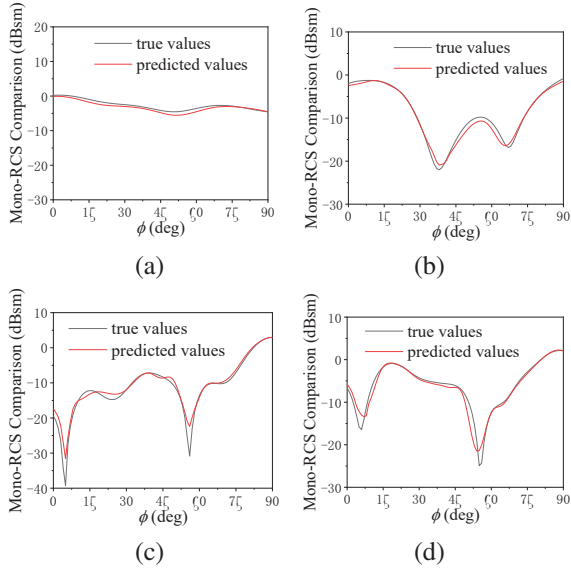


Fig. 8. Comparison of the predicted mono-RCS of the SLICY model and the true values under different incident angles at various frequencies: (a) $\theta = 45^\circ$, $f = 0.65$ GHz, (b) $\theta = 51^\circ$, $f = 0.95$ GHz, (c) $\theta = 81^\circ$, $f = 1.15$ GHz, and (d) $\theta = 66^\circ$, $f = 1.35$ GHz.

Table 3: RMSE and cost time comparison of proposed method with POI-SVR for SLICY model in 1 GHz

Model	RMSE (dBsm)	Cost Time (s)
SVR-GWO	0.59	373.8
POI-SVR	0.72	1240.5

frequency point, the proposed method achieves higher accuracy while reducing the training time compared to POI-SVR.

IV. CONCLUSION

In this paper, a method based on the SVR model and GWO algorithm is proposed to predict monostatic RCS with high accuracy and efficiency. Unlike the existing SVR models, the proposed SVR-GWO method can predict the monostatic RCS of complex targets simultaneously in a wide range of incident angles and within wide frequency bands. In addition, the new method needs relatively small training datasets and less training time, which is very important to realize real-time RCS prediction for computationally expensive complex targets.

ACKNOWLEDGEMENT

This project is supported by the Natural Science Foundation of China, No. 62171026.

REFERENCES

- [1] D. K. Barton, *Modern Radar System Analysis*. Norwood, 1988.
- [2] Z. Ma, K. Xu, R. Song, C. F. Wang, and X. Chen, "Learning-based fast electromagnetic scattering solver through generative adversarial network," *IEEE Trans. Antennas Propagat.*, vol. 69, no. 4, pp. 2194-2208, Apr. 2021.
- [3] H. J. Hu, L. Y. Xiao, J. N. Yi, and Q. H. Liu, "Non-linear electromagnetic inversion of damaged experimental data by a receiver approximation machine learning method," *IEEE Antennas Wireless Propagat. Lett.*, vol. 20, no. 7, pp. 1185-1189, July 2021.
- [4] S. Koziel and M. Abdullah, "Machine-learning-powered EM-based framework for efficient and reliable design of low scattering metasurfaces," *IEEE Trans. Microw. Theory Tech.*, vol. 69, no. 4, pp. 2028-2041, Apr. 2021.
- [5] J. Guo, Y. Li, S. Cai, and D. Su, "Fast prediction of electromagnetic scattering characteristics of targets based on deep learning," *IEEE/ACES Int. Conf. Wireless Commun. Appl. Comput. Electromagn.*, pp. 1-2, 2021.
- [6] P. Zhang, W. Liu, L. Guo, and J. She, "Efficient RCS prediction of composite scene based on deep BP neural networks," *2021 Photonics & Electromagnetics Research Symposium (PIERS)*, pp. 1319-1325, 2021.
- [7] Y. Zhao, J. Jiang, and L. Miao, "RCS prediction of polygonal metal plate based on machine learning," *IEEE/ACES Int. Conf. Wireless Commun. Appl. Comput. Electromagn.*, pp. 1-2, 2021.
- [8] D. Xiao, L. Guo, W. Liu, and M. Hou, "Improved Gaussian process regression inspired by physical optics for the conducting target's RCS prediction," *IEEE Antennas Wireless Propagat. Lett.*, vol. 19, no. 12, pp. 2403-2407, Dec. 2020.
- [9] D. Xiao, L. Guo, W. Liu, and M. Hou, "Efficient RCS prediction of the conducting target based on physics-inspired machine learning and experimental design," *IEEE Trans. Antennas Propagat.*, vol. 69, no. 4, pp. 2274-2289, Apr. 2021.
- [10] T. Yan, D. Li, and W. Yu, "A surrogate modeling technique based on space mapping for radar cross section," *IEEE Antennas Wireless Propagat. Lett.*, vol. 21, no. 8, pp. 1630-1633, Aug. 2022.
- [11] S. Mirjalili, S. M. Mirjalili, and A. Lewis, "Grey wolf optimizer," *Adv. Eng. Softw.*, vol. 69, pp. 46-61, Mar. 2014.
- [12] S. R. Gunn, "Support vector machines for classification and regression," *ISIS Technical Report*, vol. 14, no. 1, pp. 5-16, 1998.

- [13] F. Pedregosa, G. Varoquaux, A. Gramfort, V. Michel, B. Thirion, O. Grisel, M. Blondel, P. Prettenhofer, R. Weiss, V. Dubourg, and J. Vanderplas, "Scikit-learn: machine learning in Python," *J. Mach. Learn. Res.*, vol. 12, pp. 2825-2830, 2011.
- [14] D. Zhang, "A coefficient of determination for generalized linear models," *Am. Stat.*, vol. 71, no. 4, pp. 310-316, Oct. 2017.
- [15] W. Q. Liu and M. He, "Accelerating solution of volume-surface integral equations with multiple right-hand sides by improved skeletonization techniques," *IEEE Antennas Wireless Propagat. Lett.*, vol. 18, no. 10, pp. 2006-2010, Oct. 2019.
- [16] T. Chai and R. R. Draxler, "Root mean square error (RMSE) or mean absolute error (MAE)? - arguments against avoiding RMSE in the literature," *Geosci. Model Dev.*, vol. 7, no. 3, pp. 1247-1250, June 2014.
- [17] G. J. K. Tomy and K. J. Vinoy, "A fast polynomial chaos expansion for uncertainty quantification in stochastic electromagnetic problems," *IEEE Antennas Wireless Propagat. Lett.*, vol. 18, no. 10, pp. 2120-2124, 2019.
- [18] K. Konakli, C. Mylonas, S. Marelli, and B. Sudret, "Uqlab user manual-canonical low-rank approximations," *Report UQLab-VI*, pp. 1-108, 2019.
- [19] L. M. Yuan, Y. G. Xu, W. Ga, F. Dai, and Q. L. Wu, "Design of scale model of plate-shaped absorber in a wide frequency range," *Chin. Phys. B*, vol. 27, no. 4, p. 044101, 2018.



Zhourui Zhang received the B.S. degree in electrical engineering from Beijing Institute of Technology, Beijing, China, in July 2018, and the M.S. degree in electrical engineering from University of California, San Diego, US, in March 2021. He is currently pursuing the Ph.D. degree in electronic science and technology at the Beijing Institute of Technology, Beijing, China. His current research interest is yield and sensitivity analysis of antenna-radome systems.



Pengyuan Wang received the B.S. degree in communication engineering from North China Electric Power University, Baoding, China, in 2019. She is currently pursuing the Ph.D. degree in electromagnetics and microwave technology at the Beijing Institute of Technology, Beijing. Her current research interests include computational electromagnetics and parallel computation.



Mang He (Senior Member, IEEE) received the B.S. and Ph.D. degrees from the Department of Electrical Engineering, Beijing Institute of Technology, Beijing, China, in 1998 and 2003, respectively. From 2003 to 2004, he was a research associate with the Department of Electronic Engineering, City University of Hong Kong, Hong Kong. From 2008 to 2009, he was a post-doctoral research fellow with the Department of Electrical and Communication Engineering, Tohoku University, Sendai, Japan. He is currently a professor at the Beijing Institute of Technology. His current research interests include computational electromagnetics and its applications, antenna theory and design, radome, and frequency-selective surface design.

High-precision Solution of Monostatic Radar Cross Section based on Compressive Sensing and QR Decomposition Techniques

Chaofan Shi¹, Yufa Sun^{1*}, Mingrui Ou¹, Pan Wang¹, and Zhonggen Wang²

¹School of Electronic and Information Engineering
Anhui University, Hefei, 230601, China

1186621445@qq.com, yfsun_ahu@sina.com, 15838288570@163.com, pwangsunny@foxmail.com

*Corresponding Author

²School of Electrical and Information Engineering
Anhui University of Science and Technology, Huainan, 232001, China
zgwang@ahu.edu.cn

Abstract – In solving the monostatic electromagnetic scattering problem, the traditional improved primary characteristic basis function method (IPCBFM) often encounters difficulties in constructing the reduced matrix due to the long computation time and low accuracy. Therefore, a new method combining the compressed sensing (CS) technique with IPCBFM is proposed and applied to solve the monostatic electromagnetic scattering problem. The proposed method utilizes the characteristic basis functions (CBFs) generated by the IPCBFM to achieve a sparse transformation of the surface-induced currents. Several rows in the impedance matrix and excitation vector are selected as the observation matrix and observation vector. The QR decomposition is adopted as the recovery algorithm to realize the recovery of surface-induced currents. Numerical simulations are performed for cylinder, cube, and almond models, and the results show that the new method has higher solution accuracy, shorter computation time, and stronger solution stability than the traditional IPCBFM. It is worth mentioning that the new method reduces the recovery matrix size and the number of CBFs quantitatively, and provides a novel solution for solving monostatic RCS of complex targets.

Index Terms – compressing sensing, characteristic basis functions, monostatic electromagnetic scattering.

I. INTRODUCTION

The method of moments (MOM) [1] has been a powerful numerical technique widely used for solving electromagnetic scattering problems. However, as the electrical size of the computed target increases, the computational cost becomes unacceptably high. To address this issue, several improved methods have been proposed, including the fast multipole method (FMM) [2],

the characteristic basis function method (CBFM) [3–4], the adaptive integration method (AIM) [5], and the adaptive cross approximation (ACA) algorithm [6]. Recently, compressive sensing (CS) technology has been applied to MOM, offering a new solution method. The CS technique in the analysis of electromagnetic scattering problems contains two traditional computational models. The first model is used to decrease the number of incident angles, compressing only the excitation sources [7–8]. The second model involves transforming the dense matrix equation into an underdetermined equation that satisfies the CS framework [9–10]. An underdetermined equation is a system of linear equations with more unknowns than equations. For example, Wang proposed two methods to efficiently analyze the three-dimensional bistatic scattering problem [11–12]. The conventional underdetermined equation [13] computation model is not suited for analyzing monostatic electromagnetic scattering problems. The core problem is that traditional recovery algorithms, such as generalized orthogonal matching pursuit (GOMP) [14] and orthogonal matching pursuit (OMP) [15], are not suitable for the analysis of such problems. When using GOMP or OMP as the recovery algorithm to analyze the monostatic scattering problem, it is necessary to repeat the solution for each incident angle, which increases the computation time. If we can find a suitable recovery algorithm to overcome the repeated solution at each angle, we can fully utilize the advantages of constructing an underdetermined equation computational model, reduce the complexity of the algorithm, and reduce the computation time by compressing the impedance matrix.

The CBFM [4] is an effective method for solving monostatic electromagnetic scattering problems. In [16], the ACA-SVD has been adapted to efficiently generate the characteristic basis functions (CBFs), which

reduces both the time of generating the initial CBFs and the singular value decomposition (SVD) time of initial CBFs. In [17], high-level CBFs have been proposed to improve the iterative solution efficiency of CBFM. In [18], a new method of constructing reduced matrix equations is proposed to reduce the time of constructing CBFs. In [19], an improved primary CBFM (IPCBFM) has been proposed to reduce the amount of memory used for the reduced matrix by combining the secondary CBFs with the primary CBFs. While these methods aim to address the monostatic electromagnetic scattering problem by constructing a reduced matrix, the solution often encounters difficulties in solving monostatic electromagnetic scattering problems due to the long computation time and low accuracy.

To overcome the aforementioned issues, a new method called CS-IPCBFM is proposed in this paper. The proposed approach utilizes IPCBFM to generate fewer CBFs that serve as a sparse transformation matrix [10], thereby reducing the dimension of the recovery matrix and accelerating the solution process. Using the QR decomposition [20] algorithm instead of the traditional GOMP algorithm, the recovery matrix equation can be decomposed once, and other incident angles can be solved directly. Therefore, the problem that too many incident angles cause too long solving time can be solved. Several numerical experiments of differently shaped targets are conducted to verify the better computation accuracy and shorter computation time of the CS-IPCBFM.

II. COMPRESSIVE SENSING THEORY

In signal processing and numerous other application domains, signal recovery plays a pivotal role. Successful signal recovery not only effectively suppresses noise but also simplifies the data processing and transmission workflow, and helps to extract the original information, which has a high value in various fields.

If a signal exhibits sparsity in the transform domain, it can be represented using an observation matrix that is uncorrelated with the sparse transformation basis [10]. The signal recovery process primarily consists of the following three parts:

A. Sparse representation

Sparse representation means that the signal has very few non-zero elements in a certain representation, which makes it possible to accurately recover the signal with much less data than traditional sampling, thus achieving efficient signal acquisition and transmission.

Consider a signal X of dimension $N \times 1$. If X is inherently sparse, we can proceed directly to the next phase. For non-sparse signals, it's crucial to find an optimal sparse transformation matrix, denoted as Ψ to

represent X in its sparse form:

$$X_{N \times 1} = \Psi_{N \times N} \alpha_{N \times 1}, \quad (1)$$

where, Ψ represents the sparse transformation matrix, and α represents the coefficient vector.

B. Measurement matrix design

If the signal $X_{N \times 1}$ is sparse, it can be directly observed using the measurement matrix $\Phi \in R^{M \times N}$ ($M < N$) to obtain a low-dimensional measurement vector $Y_{M \times 1}$, which can be expressed as

$$Y_{M \times 1} = \Phi_{M \times N} X_{N \times 1}. \quad (2)$$

If the signal $X_{N \times 1}$ is non-sparse, substituting equation (1) into equation (2), the following expression is obtained:

$$Y_{M \times 1} = \Phi_{M \times N} \Psi_{N \times N} \alpha_{N \times 1} = \Theta_{M \times N} \alpha_{N \times 1} \quad (3)$$

where $\Theta_{M \times N}$ is the recovery matrix.

C. Signal recovery

If the projection of the signal $X_{N \times 1}$ onto $\Psi_{N \times N}$ has only k non-zero elements, signal $X_{N \times 1}$ is referred to as k sparse. The high-dimensional original signal $X_{N \times 1}$ is reconstructed by utilizing a low-dimensional observation vector $Y_{M \times 1}$. when the restricted isometry property (RIP) [21] is satisfied and the value of M satisfies $M \geq O(k \log(N/k))$, α can be recovered with high probability by solving an l_1 -norm optimization problem denoted as

$$\hat{\alpha} = \arg \min \|\alpha\|_1 \text{ s.t } \Theta \alpha = Y, \quad (4)$$

where $\|\cdot\|_1$ denotes the l_1 norm [22]. In this paper, the QR decomposition is chosen as the recovery algorithm for solving $\hat{\alpha}$. Finally, the original signal X is obtained by substituting $\hat{\alpha}$ into equation (1).

A simple example is provided here for illustration. Consider a signal $x = [2, 3, 1, 4, 2]$. Upon applying the discrete cosine transform (DCT) to x , we obtain $s = DCT[x] = [12, -1.4, 0.6, -3.7, -1.5]$. Assuming that the threshold is 1.5, the coefficient whose absolute value is higher than the threshold is retained, thus $\hat{s} = [12, 0, 0, -3.7, 0]$. Applying the inverse DCT to these coefficients, we reconstruct the signal as $\hat{x} = [2.2, 2.9, 1.2, 3.8, 1.9]$.

III. THE APPLICATION OF CS IN THE CONSTRUCTION OF AN UNDERMINED EQUATION

The CBFM divides the target into M blocks, with each block discretized into N_i units. Using N_{pws} plane waves as excitations to generate primary characteristic basis functions (PCBFs). Let P_θ and P_φ represent the number of samples in the θ and φ directions, respectively. The total number of plane waves is $N_{pws} = 2P_\theta P_\varphi$. The PCBFs J_{ii}^P for the block i is defined as

follows:

$$Z_{ii}J_{ii}^P(\theta) = E_i^{N_{pws}}(\theta) (i = 1, 2, \dots, M), \quad (5)$$

where Z_{ii} is the $N_i \times N_i$ impedance matrix of self-interaction within the block i , $E_i^{N_{pws}}$ is the matrix containing excitation vectors with size $N_i \times N_{pws}$, θ is the incident angle, and J_{ii}^P is the $N_i \times N_{pws}$ matrix to be obtained. The secondary characteristic basis functions J_{ij}^S indicates the mutual interaction component between block i and j . The definition of J_{ij}^S for block i is as follows:

$$Z_{ii}J_{ij}^S(\theta) = -Z_{ij}J_{ij}^P(\theta) (j = 1, 2, \dots, M) \quad (6)$$

where, Z_{ij} is the $N_i \times N_j$ mutual impedance between the subdomains i and j , J_{ij}^S is the $N_i \times N_{pws}$ matrix. Combining equation (6) and equation (7), the IPCBFs J_i^{IP} can be obtained and represented as

$$\begin{aligned} & Z_{ii}J_{ii}^P(\theta) + \sum_{j=1(j \neq i)}^M Z_{ij}J_{ij}^S(\theta) \\ &= Z_{ii} \sum_{j=1}^M J_{ij}^{PS}(\theta) = Z_{ii}J_i^{IP}(\theta), \\ &= E_i^{N_{pws}}(\theta) - \sum_{j=1(j \neq i)}^M Z_{ij}J_{jj}^P(\theta) \end{aligned} \quad (7)$$

where J_i^{IP} is the $N_i \times N_{pws}$ matrix, J_{ij}^{PS} includes both J_{ii}^P and J_{ij}^S . In the IPCBFM [19], due to the selection of a large number of incident waves N_{pws} , the generated matrix J_i^{IP} contains redundant information. The singular value decomposition (SVD) technique is employed to decompose J_i^{IP} . After SVD processing, a set of \hat{J}_i^{IP} is generated that is independent of the incident angle. The J_i^{IP} can be represented as

$$J_i^{IP} = U \Sigma V^T, \quad (8)$$

where U and V are unitary matrices, Σ is a semi-positive definite diagonal matrix. SVD is performed on matrix J_i^{IP} using a threshold value $\varepsilon = \sigma_M / \sigma_1$. Singular values greater than ε are retained, while values less than that are discarded, resulting in the matrix \hat{J}_i^{IP} . Assuming there are K_i retained IPCBFs in the i -th subdomain, \hat{J}_i^{IP} can be denoted as

$$\hat{J}_i^{IP} = \sum_{k=1}^{K_i} \alpha_i^k J_i^k, (i = 1, 2, \dots, M), \quad (9)$$

where α_i^k is the undetermined coefficient of the IPCBFs. The surface-induced current of the entire target can be denoted as

$$\begin{aligned} J &= \begin{bmatrix} \hat{J}_1^{IP} \\ \hat{J}_2^{IP} \\ \vdots \\ \hat{J}_M^{IP} \end{bmatrix} = \sum_{k=1}^{K_1} \alpha_1^k \begin{bmatrix} J_1^k \\ [0] \\ \vdots \\ [0] \end{bmatrix} + \dots + \sum_{k=1}^{K_M} \alpha_M^k \begin{bmatrix} [0] \\ [0] \\ \vdots \\ J_M^k \end{bmatrix} \\ &= \begin{bmatrix} J_1^C & \dots & 0 & \dots & 0 \\ \vdots & \ddots & \vdots & \ddots & \vdots \\ [0] & \dots & J_i^C & \dots & [0] \\ \vdots & \ddots & \vdots & \ddots & \vdots \\ [0] & \dots & [0] & \dots & J_M^C \end{bmatrix} \begin{bmatrix} \alpha_1^C \\ \vdots \\ \alpha_i^C \\ \vdots \\ \alpha_M^C \end{bmatrix} = \hat{J}^C \alpha, \end{aligned} \quad (10)$$

where $\alpha_i^C = [\alpha_i^1 \ \alpha_i^2 \ \dots \ \alpha_i^{K_i}]$, $J_i^C = [J_i^1 \ J_i^2 \ \dots \ J_i^{K_i}]$.

In the MOM, the surface integral equation is discretized by the Rao-Wilton-Glisson (RWG) basis function into a matrix equation as follows:

$$Z_{N \times N} \cdot J_{N \times 1}(\theta) = E_{N \times 1}(\theta) \quad (11)$$

where $Z_{N \times N}$ is the impedance matrix, $J_{N \times 1}$ is the surface-induced currents, $E_{N \times 1}$ is an excitation vector, N represents the number of the RWG basis functions. The measurement matrix $\tilde{Z}_{L \times N}$ and measurement vector $\tilde{E}_{L \times 1}$ are created by randomly selecting L ($L < N$) rows from matrices $Z_{N \times N}$ and $E_{N \times 1}$, respectively. An under-determined equation is created as

$$\tilde{Z}_{L \times N} J_{N \times 1}(\theta) = \tilde{E}_{L \times 1}(\theta). \quad (12)$$

By substituting equation (10) into equation (12), an overdetermined system of equations is obtained:

$$\tilde{Z}_{L \times N} \hat{J}_{N \times K}^C \alpha_{K \times 1} = \Theta_{L \times K} \alpha_{K \times 1} = \tilde{E}_{L \times 1}(\theta), \quad (13)$$

where $\Theta_{L \times K}$ is the recovery matrix, $\hat{J}_{N \times K}^C$ is the sparse transformation matrix. K ($K < L$) represents the total number of retained IPCBFs across all subdomains.

Firstly, the conventional GOMP is employed as the recovery algorithm to solve equation (13), and this method is referred to as CS-IPCBFM-1 in this paper. Where the GOMP algorithm is as follows:

Algorithm 1 GOMP algorithm

Input:

incidence angles count	n
incidence angles	$\theta = 1, 2, \dots, n$
measurements matrix	$\tilde{E}(\theta) \in \mathbb{C}^{L \times 1}$
sensing matrix	$\Theta \in \mathbb{C}^{L \times K}$
sparsity	K
number of indices for each selection	$S = K/2$

Initialize:

iteration count	$k = 1$
residual vector	$r_0 = \tilde{E}$

estimated support set $A_0 = \emptyset$
undetermined coefficient α

Computation:
for $i = 1$ **to** n
 While $k < \min\{S, 4\}$ **do** $k = k + 1$
 (Identification) Select indices $\{\phi(i)\}_{i=1,2,\dots,S}$
 corresponding to S largest entries in $\Theta^T r_{k-1}$.
 (Augmentation) $A_0 = A_{k-1} \cup \{\phi(1), \dots, \phi(S)\}$.
 (Estimation of $\bar{\alpha}_{A_k}$)

$$\bar{\alpha}_{A_k} = \arg \min_u \|\bar{E}(\theta) - \Theta_{A_k} u\|_2$$

$$= (\Theta_{A_k}^T \Theta_{A_k})^{-1} \Theta_{A_k}^T \bar{E}(\theta)$$
 (Residual Update) $r_k = \bar{E}(\theta) - \Theta_{A_k} \bar{\alpha}_{A_k}$
End
 $\bar{\alpha}^\theta = \arg \min_{u: \text{supp}(u) = A_k} \|\bar{E}(\theta) - \Theta u\|_2$
End
Output $\alpha = \{\bar{\alpha}^1, \bar{\alpha}^2, \dots, \bar{\alpha}^n\}$

However, as depicted in Algorithm 1, this method requires repeated calculations at each incidence angle, making the computation time increase.

Next, the least squares fitting method is employed to solve equation (13) and this computation method is called CSIPCBFM-2 in this paper. Where the least squares fitting algorithm is as follows:

Algorithm 2 least squares fitting algorithm

Input:
incidence angles count n
incidence angles $\theta = 1, 2, \dots, n$
measurements matrix $\bar{E}(\theta) \in \mathbb{C}^{L \times 1}$
sensing matrix $\Theta \in \mathbb{C}^{L \times K}$
normal matrix $A \in \mathbb{C}^{K \times K}$

Initialize:
upper triangular matrix U
lower triangular matrix L
normal matrix $A = \Theta^T \Theta$
Excitation vector $b_\theta = \Theta^T \bar{E}(\theta)$
undetermined coefficient α

LU decomposition:
 $A\alpha = b_\theta$
After LU decomposition of A , the matrix is L and U
 $LU\bar{\alpha} = b_\theta$

Computation:
for $\theta = 1$ **to** n
 $Ly_\theta = b_\theta$
 $U\bar{\alpha}^\theta = y_\theta$
End
Output $\alpha = \{\bar{\alpha}^1, \bar{\alpha}^2, \dots, \bar{\alpha}^n\}$

As described in Algorithm 2, the method first performs the LU decomposition of A and then performs the solution process, avoiding repeated solutions at each incident angle.

Finally, the QR decomposition is used as the recovery algorithm to solve equation (13), and this method is called CS-IPCBFM in this paper. Where the QR decomposition algorithm is as follows:

Algorithm 3 QR decomposition algorithm

Input:
incidence angles count n
incidence angles $\theta = 1, 2, \dots, n$
measurements matrix $\bar{E}(\theta) \in \mathbb{C}^{L \times 1}$
sensing matrix $\Theta \in \mathbb{C}^{L \times K}$

Initialize:
upper triangular matrix R
orthogonal matrix Q

QR decomposition of Householder transform:
 $\Theta\alpha = \bar{E}(\theta)$
Householder transformation on Θ matrix.
 $QR\alpha = \bar{E}(\theta)$
 $(QR)^T(QR)\alpha = (QR)^T \bar{E}(\theta)$
 $R^T Q^T QR\alpha = R^T Q^T E(\theta)$
 $R\alpha = Q^T E(\theta)$

for $i = 1$ **to** n
 $\alpha^\theta = R^{-1} Q^T E(\theta)$
End
Output $\alpha = \{\bar{\alpha}^1, \bar{\alpha}^2, \dots, \bar{\alpha}^n\}$

As described in Algorithm 3, the QR decomposition method is used to decompose the recovery matrix θ and then solve it, avoiding repeated solutions at each incident angle.

IV. COMPLEXITY ANALYSIS

To provide a clear comparison of the complexity between IPCBFM and CS-IPCBFM, a focused analysis was conducted solely on these two methods. CS-IPCBFM-1 and CS-IPCBFM-2, on the other hand, were validated via numerical simulations. The calculation processes for IPCBFM and CS-IPCBFM consist of three steps: filling the impedance matrix, constructing IPCBFs, and solving the radar cross section (RCS).

Since both filling the impedance matrix and constructing IPCBFs are identical for IPCBFM and CS-IPCBFM, this section focuses solely on comparing the complexities of the RCS-solving steps.

The RCS solution process of IPCBFM involves constructing and solving the reduced matrix equation, whose combined complexity is $O(K^2 N_i^2 + K^3)$. In CS-IPCBFM, the RCS solution process includes the

construction of the recovery matrix and the solution of equation (13), whose combined complexity is $O(NLK + K^2 + LK)$. Since $NL < KN_i^2$, and $K + L < K^2$, the RCS calculation time of CS-IPCBFM will be shorter than that of IPCBFM.

V. NUMERICAL RESULTS

To validate the effectiveness of the proposed method, three models of cylinder, cube, and almond are simulated. Where, the cylinder model with fewer unknowns was used to compare IPCBFM, CS-IPCBFM-1, and CS-IPCBFM methods. While the cube and almond models with more unknowns were used to compare IPCBFM, CS-IPCBFM-2, and CS-IPCBFM methods. The results were computed using an AMD Ryzen 75800H with Radeon Graphics 3.20 GHz and 64.0 GB RAM, and the simulations were compiled using Visual Studio 2022RC. Additionally, all examples utilized a double-precision floating point. The root-meant-square error of the target monostatic RCS is defined as

$$Err(\%) = 100\% \times \sqrt{\frac{1}{N} \sum_{i=1}^N |RCS_i - RCS_i^{MOM}|^2 / |RCS_i^{MOM}|^2}. \quad (14)$$

Firstly, the monostatic RCS of a perfect electrical conductor (PEC) cylinder with a length of 2 m and radius of 0.3 m at 800MHz is calculated. The angle of incidence is set to $\theta = 0^\circ - 180^\circ$, $\phi = 0^\circ$. The geometry was divided into 5046 triangular patches, resulting in 14,161 unknowns. Subsequently, the cylinder was segmented into 12 blocks, with each block extending $\Delta = 0.15\lambda$ in all directions, which increased the number of unknowns to 25,966. When the threshold ϵ is set to 0.01, a total of 755 IPCBFs are obtained. The monostatic RCS values of MOM, IPCBFM, CSIPCBFM-1, and CS-IPCBFM are found to be highly consistent, as depicted in Fig. 1.

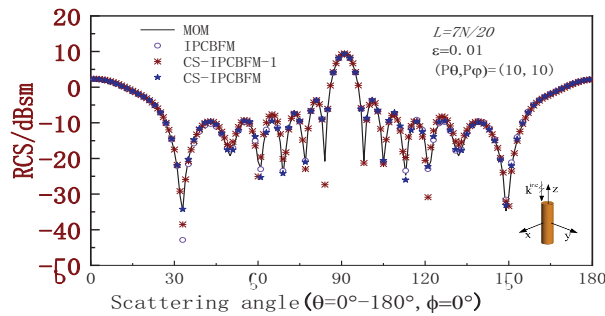


Fig. 1. HH polarization monostatic RCS of cylinder.

As the number of rows L increases, the computation time of CS-IPCBFM and CS-IPCBFM-1 is shown in Figs. 2 and 3, respectively. The computation time of IPCBFM is 18.481 s, as depicted in Fig. 2. As can be

seen from Figs. 2 and 3, when $20L/N$ is less than 11, CS-IPCBFM has the lowest computation time compared to IPCBFM and CSIPCBFM-1. The RCS error of the IPCBFM, CS-IPCBFM-1 and CS-IPCBFM is shown in Fig. 4. When $20L/N$ is greater than 6, the CS-IPCBFM has the highest accuracy compared to the IPCBFM and CS-IPCBFM-1.

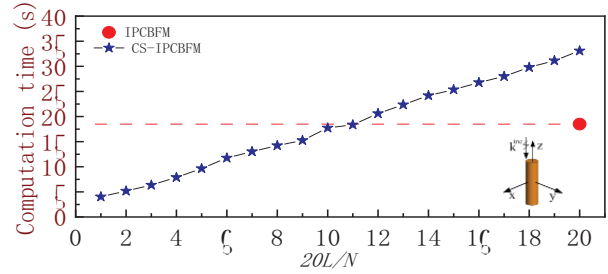


Fig. 2. Computation time of cylinder for different L .

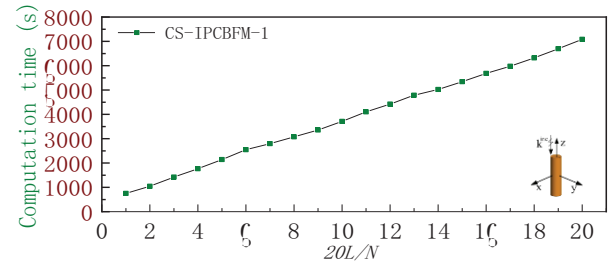


Fig. 3. Computation time of cylinder for different L .

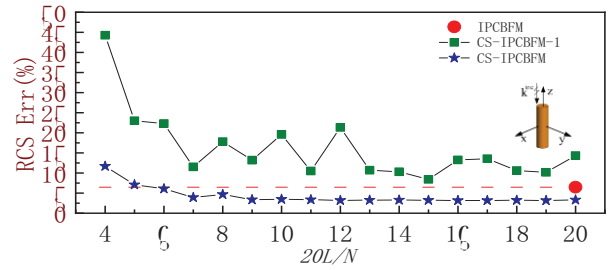


Fig. 4. RCS Err of the cylinder for different L .

Next, the monostatic RCS of a PEC cube with a length of 1 m at 800MHz is calculated. The angle of incidence is set to $\theta = 0^\circ - 180^\circ$, $\phi = 0^\circ$. The cube is discretized into 13,980 triangular patches producing 25,981 unknowns. When the target is divided into 8 blocks, with each block extending by $\Delta = 0.15\lambda$ in all directions, the number of unknowns increases to 46,951. Furthermore, a total of 789 IPCBFs are obtained when the SVD threshold is set to $\epsilon = 0.02$. The monostatic RCS values of MOM, IPCBFM, CS-IPCBFM-2, and CS-IPCBFM are

found to be highly consistent, as depicted in Fig. 5. As the SVD threshold ε increases, the RCS error and computation time of IPCBFM and CSIPCBFM is shown in Figs. 6 and 7. From these figures, it can be seen that CS-IPCBFM has a shorter computation time and lower RCS error compared to IPCBFM. As the number of rows L increases, the RCS error and computation time of the CS-IPCBFM and CS-IPCBFM-2 are shown in Figs. 8 and 9. While the RCS error and computation time of IPCBFM are 2.0632% and 189.657s, as depicted in Figs. 8 and 9, respectively. As can be seen from Figs. 8 and 9, when $20L/N$ is less than 15, the CS-IPCBFM has a shorter computation time compared to IPCBFM. When $20L/N$ is greater than 3, the accuracy of CS-IPCBFM is comparable to that of IPCBFM and better than that of CS-IPCBFM-2.

Finally, the monostatic RCS of a PEC almond with a length of 252.374 mm at a frequency of 7GHz is

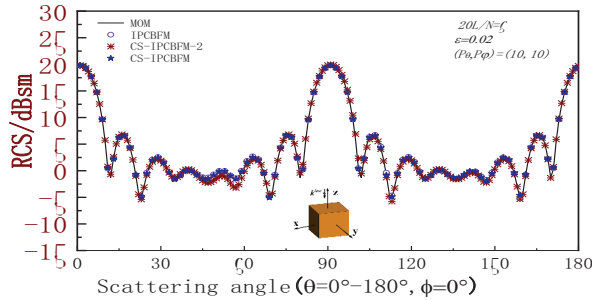


Fig. 5. HH polarization monostatic RCS of the cube.

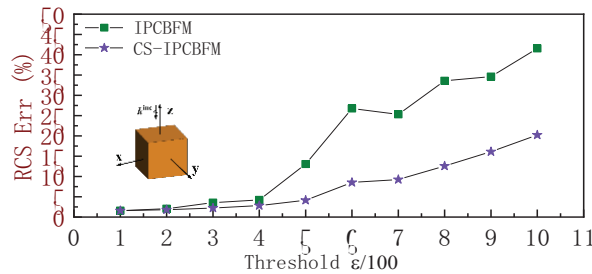


Fig. 6. RCS Err of the cube for different ε .

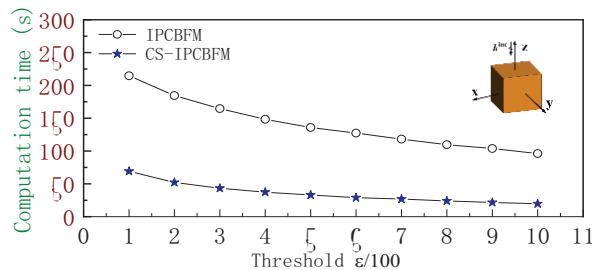


Fig. 7. Computation time of the cube for different ε .

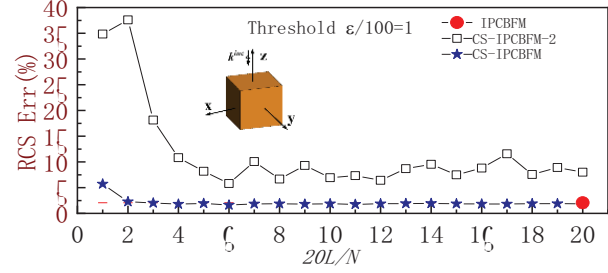


Fig. 8. RCS Err of the cube for different L .

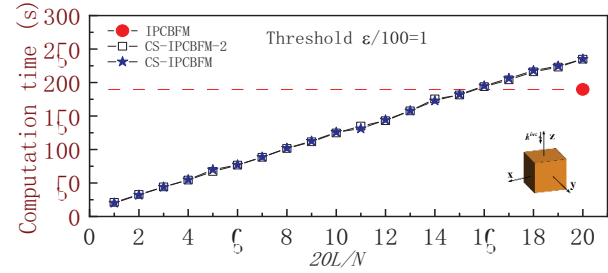


Fig. 9. Computation time of the cube for different L .

computed. The target is divided into 8 blocks, and each block is extended by $\Delta = 0.15\lambda$ in all directions, increasing the number of unknowns to 62,653. A total of 710 IPCBFMs are obtained when the threshold $\varepsilon = 0.01$. The monostatic RCS of MOM, IPCBFM, and CS-IPCBFM under horizontal polarizations are found to be highly consistent, and the monostatic RCS of CS-IPCBFM-2 is poor, as depicted in Fig. 10. Finally, the influence of different incident plane wave numbers on the stability of IPCBFM and CS-IPCBFM is investigated. The calculation time and RCS error for various numbers of incident waves are shown in Table 1.

Table 1: Calculation time and RCS error of the almond for various numbers of incident waves

Method	(P_θ, P_ϕ)	Computation Time (s)	RCS Err (%)
IPCBFM	(5,5)	95.439	47.8028
CS-IPCBFM	(5,5)	48.922	26.3877
IPCBFM	(6,6)	145.945	43.1824
CS-IPCBFM	(6,6)	67.16	24.8070
IPCBFM	(7,7)	200.084	31.4387
CS-IPCBFM	(7,7)	84.298	7.9510
IPCBFM	(8,8)	255.595	7.8126
CS-IPCBFM	(8,8)	99.567	4.9569
IPCBFM	(9,9)	265.909	6.9566
CS-IPCBFM	(9,9)	107.044	3.0830
IPCBFM	(10,10)	291.401	3.7763
CS-IPCBFM	(10,10)	114.989	2.1990

Table 2: Comparison of calculation time, RCS Err, and memory consumption

Model	Method	Impedance Matrix Filling Time (s)	IPCBFs Generation (s)	Solving Time (s)	Total Time (s)	RCS Err (%)	Memory (GB)
Cylinder	IPCBFM			18.481	304.899	6.4736	4.876
	CS-IPCBFM-1	23.194	263.224	2794.45	3080.868	11.5301	4.978
	CS-IPCBFM			13.013	299.431	3.9032	4.473
Cube	IPCBFM			164.685	2367.29	6.6891	17.3826
	CS-IPCBFM-2	72.884	2129.621	42.182	2244.33	36.0286	15.341
	CS-IPCBFM			43.322	2245.93	4.7641	15.324
Almond	IPCBFM			291.401	5540.687	3.7763	39.918
	CS-IPCBFM-2	153.876	5095.41	113.632	5362.918	14.8080	36.831
	CS-IPCBFM			114.989	5364.275	2.1990	39.561

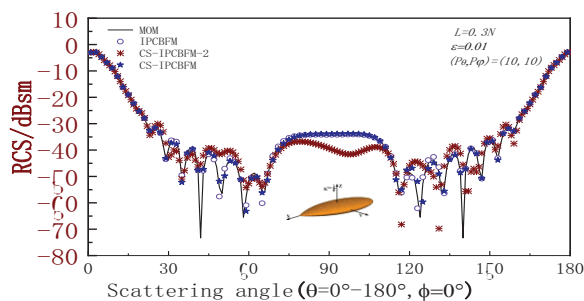


Fig. 10. HH polarization monostatic RCS of the almond.

It can be seen from Table 1 that the accuracy stability of the method proposed in this paper is better than that of IPCBFM. The computation time and RCS error of the simulation examples in Figs. 1, 5, and 10 are shown in Table 2. The results show that CS-IPCBFM has a shorter computation time and the highest accuracy in calculating the monostatic RCS.

VI. CONCLUSION

To improve the efficiency and accuracy of IPCBFM, we integrated CS with IPCBFM and refined the conventional CS recovery algorithm. In comparison to IPCBFM, CS-IPCBFM-1 with traditional recovery algorithm has some lag in speed and accuracy, CS-IPCBFM-2 with the least square fitting achieves faster calculation, but the accuracy is compromised, CS-IPCBFM with QR decomposition not only excels in both speed and precision but also offers superior stability.

ACKNOWLEDGMENT

This work was supported in part by the National Natural Science Foundation of China under Grant 62071004 and the Project of Anhui Provincial Natural Science Foundation under Grant no. 2108085MF200.

REFERENCES

[1] R. F. Harrington, *Field Computation by Moment Methods*, Malabar, Fla.: R. E. Krieger, 1968.

[2] R. Coifman, V. Rokhlin, and S. Wandzura, "The fast multipole method for the wave equation: A pedestrian prescription," *IEEE Antennas and Propagation Magazine*, vol. 53, no. 3, pp. 7-12, 1993.

[3] V. A. Prakash and R. Mittra, "Characteristic basis function method: A new technique for efficient solution of method of moments matrix equations," *Microwave and Optical Technology Letters*, vol. 36, pp. 95-100, 2002.

[4] E. Lucente, A. Monorchio, and R. Mittra, "An iteration-free MoM approach based on excitation independent characteristic basis functions for solving large multiscale electromagnetic scattering problems," *IEEE Transactions on Antennas and Propagation*, vol. 56, pp. 999-1007, 2008.

[5] E. Bleszynski, M. Bleszynski, and T. Jaroszewicz, "Adaptive integral method for solving large-scale electromagnetic scattering and radiation problems," *Radio Science*, vol. 31, pp. 1225-1251, 1996.

[6] Z. Liu, R. Chen, J. Chen, and Z. Fan, "Using adaptive cross approximation for efficient calculation of monostatic scattering with multiple incident angles," *Applied Computational Electromagnetics Society (ACES) Journal*, vol. 26, pp. 325-333, 2011.

[7] M. S. Chen, F. L. Liu, H. M. Du, and X. L. Wu, "Compressive sensing for fast analysis of wide-angle monostatic scattering problems," *IEEE Antennas and Wireless Propagation Letters*, pp. 1243-1246, 2011.

[8] S. R. Chai and L. X. Guo, "A new method based on compressive sensing for monostatic scattering analysis," *Microwave and Optical Technology Letters*, vol. 10, pp. 2457-2461, 2015.

[9] E. J. Candes, T. Tao, "Near-optimal signal recovery from random projections: Universal encoding strategies," *IEEE Transactions on Information Theory*, vol. 52, pp. 5406-5425, 2006.

- [10] D. L. Donoho, "Compressed sensing," *IEEE Trans. Inf. Theory*, vol. 52, no. 4, pp. 1289-1306, 2006.
- [11] Z. G. Wang, W. Y. Nie, and H. Lin. "Characteristic basis functions enhanced compressive sensing for solving the bistatic scattering problems of three-dimensional targets," *Microwave and Optical Technology Letters*, vol. 62, pp. 3132-3138, 2020.
- [12] Z. G. Wang, P. Wang, Y. Sun, and W. Nie, "Fast analysis of bistatic scattering problems for three-dimensional objects using compressive sensing and characteristic modes," *IEEE Antennas and Wireless Propagation Letters*, vol. 21, pp. 1817-1821, 2022.
- [13] A. M. Bruckstein, D. L. Donoho, and M. Elad, "From sparse solutions of systems of equations to sparse modeling of signals and images," *SIAM Review*, vol. 51, pp. 34-81, 2009.
- [14] J. Wang, S. Kwon, and B. Shim, "Generalized orthogonal matching pursuit," *IEEE Transactions on Signal Processing*, vol. 60, pp. 6202-6216, 2012.
- [15] J. A. Tropp and A. C. Gilbert, "Signal recovery from random measurements via orthogonal matching pursuit," *IEEE Trans. Inf. Theory*, vol. 53, pp. 4655-4666, Dec. 2007.
- [16] X. Chen, C. Gu, Z. Niu, Y. Niu, and Z. Li, "Efficient iterative solution of electromagnetic scattering using adaptive cross approximation enhanced characteristic basis function method," *IET Microwaves, Antennas & Propagation*, vol. 9, pp. 217-223, 2015.
- [17] E. García, C. Delgado, and F. Cátedra, "A novel and efficient technique based on the characteristic basis functions method for solving scattering problems," *IEEE Trans. Antennas Propag.*, vol. 67, pp. 3241-3248, 2019.
- [18] Z. G. Wang, C. Qing, and W. Y. Nie, "Novel reduced matrix equation constructing method accelerates iterative solution of characteristic basis function method," *Applied Computational Electromagnetics Society (ACES) Journal*, vol. 34, pp. 1814-1820, Dec. 2019.
- [19] T. Tanaka, Y. Inasawa, and Y. Nishioka, "Improved primary characteristic basis function method for monostatic radar cross section analysis of specific coordinate plane," *IEICE Transactions on Electronics*, vol. E99-C, pp. 2835, 2016.
- [20] C. R. Goodall. "Computation using the QR decomposition," *Handbook of Statistics*, vol. 9, pp. 467-508, 1993.
- [21] E. J. Candes. "The restricted isometry property and its implications for compressed sensing," *Comptes Rendus Mathématique*, vol. 346, pp. 589-592, 2008.
- [22] R. Baraniuk, "A lecture on compressive sensing," *IEEE Signal Processing Magazine*, vol. 24, pp. 181-121, 2006.



Chaofan Shi was born in Xinxiang Henan, China in 1996. He received his B.S. degree from Anyang Institute of Technology in 2020. He is currently pursuing a master's degree in the School of Electronic and Information Engineering at Anhui University. His research interests mainly focus on electromagnetic scattering.



Yufa Sun was born in 1966. He received the B.S. and M.S. degrees in radio physics from Shandong University, in 1988 and 1991, respectively, and the Ph.D. degree in electromagnetic field and microwave technology from the University of Science and Technology of China, in 2001. Since 1991, he has been a faculty member with Anhui University, Anhui, China, where he is currently a full professor with the School of Electronic and Information Engineering. He was a visiting scholar with the City University of Hong Kong, from 2002 to 2003, and a postdoctoral researcher with the University of Science and Technology of China, from 2003 to 2006. His research interests include electromagnetic scattering and target recognition, computational electromagnetics, and antenna theory and technology.



Mingrui Ou was born in Bengbu, Anhui, China in 1991. He received his B.S. degree from Zhengzhou University of Light Industry in 2013. He is currently pursuing a master's degree in the School of Electronic and Information Engineering at Anhui University. His research interests mainly focus on electromagnetic scattering.



Pan Wang was born in Huaibei, Anhui, China, in 1989. He received his master's degree from Anhui University of Science and Technology in 2023. He is currently pursuing a Ph.D. degree in the School of Electronic and Information Engineering at Anhui University. His research interests mainly focus on computational electromagnetics.



Zhonggen Wang received the Ph.D. degree in electromagnetic field and microwave technique from the Anhui University of China (AHU), Hefei, P. R. China, in 2014. Since 2014, he has been with the School of Electrical and Information Engineering, Anhui University of Science and Technology. His research interests include computational electromagnetics, array antennas, and reflect arrays.

Analytical Solution of Eddy Current in Parallel Conducting Strips for Low-frequency Shielding Purposes

Hamzeh M. Jaradat¹, Qasem M. Qananwah², Ahmad M. Dagamseh³,
and Qasem M. Al-Zoubi³

¹Department of Telecommunications Engineering, Hijjawi Faculty for Engineering Technology
Yarmouk University, Irbid, P.O. Box 21163, Jordan
*hamzehjaradat@yu.edu.jo

²Department of Biomedical Systems and Informatics Engineering, Hijjawi Faculty for Engineering Technology
Yarmouk University, Irbid, P.O. Box 21163, Jordan
qasem.qananwah@yu.edu.jo

³Department of Electronics Engineering, Hijjawi Faculty for Engineering Technology
Yarmouk University, Irbid, P.O. Box 21163, Jordan
a.m.k.dagamseh@yu.edu.jo, qzabi50@yu.edu.jo

Abstract – In instrumentation systems, shielding is the main issue that judges the performance of the system. The electromagnetic (EM) noise may affect the performance of the instrumentation system if inadequate protection is reached. It is considered the main source of unprotectable interference that may affect these systems in many cases. In this paper, shielding is attained by wrapping the source carrying signal with periodic thin conductive strips separated by slots or openings. This arrangement will protect the sources from the outside EM fields. Shielding factor and shielding efficiency are studied by extracting magnetic fields. For this purpose, an analytical solution based on solving Laplace's equation for the magnetic vector potential in the region of interest is presented. A closed form of the induced eddy current in the conductive strips is calculated based on Fourier series expansion. Furthermore, numerical simulation using the commercial software MWS CST is employed to validate the analytical solution. The performance of the proposed shielding structure is studied and analyzed in terms of shielding factor and shielding efficiency. The outcomes of both methods are showing very good agreement.

Index Terms – Eddy current, electromagnetic (EM) shielding, quasistatic, shielding efficiency, shielding factor.

I. INTRODUCTION

Electromagnetic Interference (EMI) resulting from EM fields is the most effective interference that may deviate the instrumentation system performance. The

evolved system requirements to overcome the inaccuracy and measurement errors through reducing EMI and producing free-of-noise signals have all been thoroughly considered. EMI has been handled to make the electronic system immune to measurement inaccuracy and errors. Electromagnetic shielding (EMS) is typically used to block or minimize either the emitted or reflected electromagnetic fields, which is the most effective way to reduce EMI. Shielding can ensure better isolation depending on the shielding structure or shape. The performance of magnetic shielding was proposed by Kim et al. [1]. An excellent shielding factor was obtained when double-layer shielding using inner silicon steel layer and mu-metal outer layer. Various shielding strategies have been investigated in the literature. Multilayer shielding was proposed in [2] and [3], where numerical analysis for shielding efficiency was calculated. The effect of material properties on the magnetic shielding was further investigated in [4] using different electrical steel panels. Park et al. [5] proposed a shielding structure that comprises a periodic metal strip inserted on a conventional ferrite plate. The model was studied by exploring the effect of metal strips on shielding properties. This shielding technique with strips has found many real-life applications [6]. Magnetic shielding of cylindrical geometry was studied and analyzed [7], [8]. The analysis deduced an inherent relationship between shielding efficiency and shielding parameters involved.

Due to the presence of a time-varying magnetic field, the mechanism of shielding arises from the fields' cancellation, which is determined by the induced eddy

current in the shield material. Several methods have been reported to find a general solution of eddy current in conductors analytically and numerically. The solution method depends on the geometry and excitation type. Closed-form expressions for eddy current in cylindrical shielding structures are obtained using second-order vector potentials [9]. The modified Bessel and exponential functions [10] are exploited to calculate the eddy current field excited by a probe coil near a conductive pipe [11]. Eddy current in conducting plates was found through solving the vector potential as a series of eigenfunctions [12]. Reduced vector potential combined with Dirichlet-to-Neumann boundary conditions, was proposed to predict the induced current density distribution in nondestructive testing applications [13]. Computational numerical techniques such as finite element method (FEM) [14] and finite difference method (FTD) [15] were utilized to calculate the induced eddy currents in thin metal sheets. These methods are complicated and require a dense system matrix. The quasi-static approximation is applied to Ampere's law, where the total magnetic field is characterized by excited and induced fields. The resulting Laplace equation was solved analytically for many practical geometries [16]. In this paper, a model of periodic coplanar conductive strips is developed. Eddy current is obtained analytically by solving the Laplace equation combined with Fourier series expansion. The effect of the strip's shielding parameters is investigated analytically and numerically.

II. EDDY CURRENT ANALYTICAL SOLUTION

The geometry comprises very thin, infinitely long parallel conductive strips of width $2b$ and thickness d that are extending along the z -axis. The strips are placed periodically along the x -direction on the xz -plane (i.e., parallel conductive strips). The slit width between the adjacent strips is $2c$. The source of the exciting field is created using an infinite number of conductive lines separated by a distance a that are arranged periodically at $y=h$ plane in parallel with the strips. The currents are distributed in an alternating fashion such that every two lines with different polarities are positioned on the top of each strip. Such configuration creates an alternating magnetic field. The arrangement of the geometry is illustrated in Fig. 1.

According to Faraday's law of induction, the time-varying magnetic fields generate an induced conduction eddy current in the conductive strips. As a response, this current creates a magnetic field that opposes the change in the excitation field. To find the eddy currents, the general solution for the vector potential A should be determined. Because the system is periodic in the x -direction with a period of $2a$, the exciting vector potential due to

line currents can be presented as the sum of solutions of the two-dimensional Laplace equation for quasistatic fields [17].

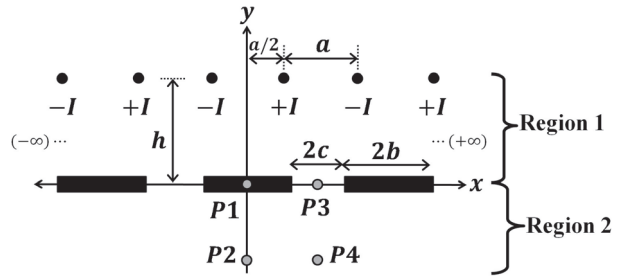


Fig. 1. Geometry of the proposed shielding system.

$$\frac{\partial^2 A_z(x, y)}{\partial x^2} + \frac{\partial^2 A_z(x, y)}{\partial y^2} = 0. \quad (1)$$

The general solution for (1) is performed using the separation of variables technique, i.e., $A_z(x, y) = X(x)Y(y)$. It is noted that the magnetic vector potential has only the z -component. Therefore, the vector potential of the known currents in the lines can be written as

$$\begin{cases} A_{e1} = \frac{\mu I}{\pi} \sum_{n=1}^{\infty} \frac{1}{n} \sin n \frac{\pi}{2} e^{-n \frac{\pi}{a}(y-h)} \sin \frac{n\pi x}{a}, & y \geq h \\ A_{e2} = \frac{\mu I}{\pi} \sum_{n=1}^{\infty} \frac{1}{n} \sin n \frac{\pi}{2} e^{n \frac{\pi}{a}(y-h)} \sin \frac{n\pi x}{a}, & y \leq h \end{cases}, \quad (2)$$

where A_{e1} and A_{e2} are the magnetic vector potentials in the regions above and below the lines, respectively, μ is the magnetic permeability of the medium, and n is a positive integer. Similarly, the vector potential due to the eddy currents in the conducting strips can be determined by solving the Laplace equation under symmetry conditions. The vector potential solution due to the unknown eddy currents becomes

$$\begin{cases} A_{s1} = \frac{\mu I}{\pi} \sum_{n=1}^{\infty} C_n e^{-n\pi(y/a)} \sin \frac{n\pi x}{a}, & y \geq 0 \\ A_{s2} = \frac{\mu I}{\pi} \sum_{n=1}^{\infty} C_n e^{n\pi(y/a)} \sin \frac{n\pi x}{a}, & y \leq 0 \end{cases}, \quad (3)$$

where A_{s1} and A_{s2} are the magnetic vector potentials in the regions above and below the conductive strips respectively, C_n are unknown coefficients that are yet to be determined. The solution is required in the two regions: region 1, $0 \leq y \leq h$, and region 2, $y \leq 0$ as depicted in Fig. 1. The complete solution is formulated by combining (2) and (3) [16]:

$$\begin{aligned} A_1 &= A_{s1} + A_{e1}, & 0 \leq y \leq h \\ A_2 &= A_{s2} + A_{e2}, & y \leq 0 \end{aligned} \quad (4)$$

Boundary conditions should be applied at both regions with,

$$A_1(x, 0) = A_2(x, 0), \quad (5)$$

$$(H_{t1} - H_{t2}) = K, \quad (6)$$

where A_1 , A_2 , H_{t1} , and H_{t2} are the magnetic vector potentials and tangential magnetic fields above and

below the shielding surface, respectively. The magnetic field intensity is related to the vector potential by the formula $H = 1/\mu \nabla \times A$. From (6), the surface current density can be written as:

$$K = \frac{2I}{a} \sum_{n=1}^{\infty} n C_n \sin n\pi \frac{x}{a}. \quad (7)$$

The eddy current flows only inside the strips such that the surface current density K at $y = 0$ can be determined using the law of induction inside the lateral conducting strips:

$$K = \begin{cases} -j\omega d \sigma(x) A_1(x, 0), & |x| \leq b \\ 0, & b < |x| \leq a \end{cases}, \quad (8-a)$$

$$A_1(x, 0) = \frac{\mu I}{\pi} \sum_{n=1}^{\infty} \left(\frac{1}{n} \sin \frac{n\pi}{2} e^{-\frac{n\pi h}{a}} + C_n \right) \sin \frac{n\pi x}{a}, \quad (8-b)$$

$$\sigma(x) = \begin{cases} \sigma_o, & |x| \leq b \\ 0, & b < |x| \leq a \end{cases}, \quad (8-c)$$

where $\sigma(x)$ is the conductivity function of the strips, which is considered as a periodic function with a constant magnitude σ_o and a period of $2a$. Consequently, it can be rewritten in terms of a Fourier series expansion:

$$\sigma(x) = \sigma_o \left(\frac{b}{a} + \frac{2}{\pi} \sum_{m=1}^{\infty} \frac{1}{m} \sin m\pi \frac{b}{a} \cos m\pi \frac{x}{a} \right). \quad (9)$$

Equating the current density expression in (7) with (8) and conducting some mathematical manipulations, will end up with a system of an infinite number of linear equations as in (10-a). The unknown coefficients C_n can be calculated by constructing the matrix elements in (10-b) and (10-c).

$$a_{mn} \cdot C_n = b_m, \quad (10-a)$$

$$a_{mn} = \begin{cases} \frac{\sin \pi (m+n) (\frac{b}{a})}{(m+n)} - \frac{\sin \pi (m-n) (\frac{b}{a})}{(m-n)}, & m \neq n \\ -\pi \frac{b}{a} + \frac{\sin 2 m \pi (\frac{b}{a})}{2m} + \frac{j m \pi^2 \delta^2}{ad}, & m = n \end{cases}, \quad (10-b)$$

$$b_m = \frac{1}{m} \cdot \sin \frac{m\pi}{2} \cdot e^{-m\pi (\frac{h}{a})} \left(\pi \frac{b}{a} - \frac{\sin 2 m \pi (\frac{b}{a})}{2m} \right) + \sum_{\substack{k=1 \\ k \neq m}}^{\infty} \frac{1}{k} \sin \frac{k\pi}{2} \cdot e^{-k\pi (\frac{h}{a})} \times \left(\frac{\sin \pi (m-k) (\frac{b}{a})}{(m-k)} - \frac{\sin \pi (m+k) (\frac{b}{a})}{(m+k)} \right), \quad (10-c)$$

where $\delta = 1/\sqrt{\pi \mu \sigma f}$ is the skin depth. For the numerical solution, the maximum value of the magnetic field is observed at specific points labeled $P1$, $P2$, $P3$, and $P4$. The positions of $P1(0,0)$, and $P3(a,0)$, are in the same plane of the strips, while $P2(0,-h)$, and $P4(a,-h)$ are located underneath the strips as indicated in Fig. 1. Only the y -component of the magnetic field is exited at

these points, which can be calculated from (4) using the relation $B_y = -\partial A / \partial x$. For instance, the flux density at $P2$ and $P4$ can be written as

$$B_2 = B_y|_{P2} = -\frac{\mu I}{a} \left(\frac{\sum_{k=0}^{\infty} (-1)^k \cdot e^{-(2k+1)2\pi (\frac{h}{a})}}{-\sum_{n=1}^{\infty} n e^{-n\pi (\frac{h}{a})} \cdot C_n} \right), \quad (11-a)$$

$$B_4 = B_y|_{P4} = \frac{\mu I}{a} \left(\frac{\sum_{k=0}^{\infty} (-1)^k \cdot e^{-(2k+1)2\pi (\frac{h}{a})}}{-\sum_{n=1}^{\infty} (-1)^n \cdot n e^{-n\pi (\frac{h}{a})} \cdot C_n} \right). \quad (11-b)$$

The magnetic flux without shielding strips, which is only due to the source currents, can be found from (2) in all regions. At points $P2$ and $P4$, the fields become

$$B_{2,0} = B_y|_{P2} = -\frac{\mu I}{a} \sum_{k=0}^{\infty} (-1)^k \cdot e^{-(2k+1)2\pi (h/a)}, \quad (12-a)$$

$$B_{4,0} = B_y|_{P4} = -B_{2,0}. \quad (12-b)$$

Based on the previous analysis, the shielding factor S can be defined as the ratio of the induced magnetic field without conductive strips to the induced magnetic field in the presence of conductive strips [18]. At points $P2$ and $P4$ the shielding factor in dB becomes

$$S_2 = 20 \log \left(\frac{|B_{2,0}|}{|B_2|} \right), \quad S_4 = 20 \log \left(\frac{|B_{4,0}|}{|B_4|} \right). \quad (13)$$

The maximum shielding occurs when there is no gap between the strips, which means a continuous conductive plane. The induced magnetic fields in the presence of the plane at the two observation points $P2$ and $P4$ become

$$B_{2,pl} = -\frac{\mu I}{a} \sum_{k=0}^{\infty} (-1)^k \cdot e^{-(2k+1)2\pi (\frac{h}{a})} \times \left(1 + j \frac{1}{\pi (2k+1)} \cdot \frac{ad}{\delta^2} \right) = -B_{4,pl}. \quad (14)$$

The performance of the field's isolation is characterized by the shielding efficiency (T). It can be defined as the ratio of the induced magnetic field with conductive strips to the induced magnetic field in the presence of a continuous conductive plane.

$$T_2 = 20 \log \left(\frac{|B_2|}{|B_{2,pl}|} \right), \quad T_4 = 20 \log \left(\frac{|B_4|}{|B_{4,pl}|} \right). \quad (15)$$

III. RESULTS AND DISCUSSION

The theoretical analysis conducted in the previous section will be applied to obtain the shielding factor and efficiency at some predefined points ($P1$, $P2$, $P3$, and $P4$, see Fig. 1). The shielding effectiveness has been considered through the shielding factor. The effect of various design parameters has been investigated. These design parameters include the position of the excitation current source relative to the width of the strip (i.e., b/a), slot size, and excitation frequency. Moreover, the presented analytical results are verified using numerical simulations with the aid of the commercial simulation package MWS CST [19]. The simulation setup is carried

out through a low-frequency solver. This solver is a 3D solver used for simulating the time-harmonic behavior in low-frequency systems. The simulated structure is composed of two parallel cylindrical lines, each of which has a diameter of 0.2 cm and a separation distance $a = 10$ cm. The two lines are excited using path current sources with equal currents and 180° out of phase. The conductive shielding strip is placed beneath and in parallel with the line currents at a distance of h . The strip has a width of b and thickness of $d = 0.2$ cm. The length of both current lines and the strip is $L = 40$ cm. All conductors are modeled by copper with a conductivity of $\sigma = 5.8 \times 10^7$ S/m. This structure has infinite periodicity along the x -direction and infinite extent along the z -direction. Therefore, to simulate this type of structure, a unit cell of finite length $2a$ could be simulated by choosing proper boundary conditions. Due to the symmetrical geometry along the x -direction, periodic boundary condition is chosen to mimic infinite copies of the unit cell (i.e., $E_t = 0$ at $x = \pm a$). On the other hand, the structure has infinite extent in the z -direction, which yields $E_t = 0$ at $z = \pm L/2$. Open boundaries are defined along $\pm y$ -directions. Tetrahedral meshing technique is utilized to perform the computational simulation in the frequency range of 10 Hz to 3 kHz, which is chosen as an illustration example to validate the presented analytical solution. All simulation data are calculated with the aid of field monitors combined with a post-processing template to process the obtained data.

In Fig. 2, the shielding factor S in dB is plotted versus the ratio ad/δ^2 at four observation points, where this ratio maps to the operating frequency. Both analytical solutions using (13) and simulated responses are plotted

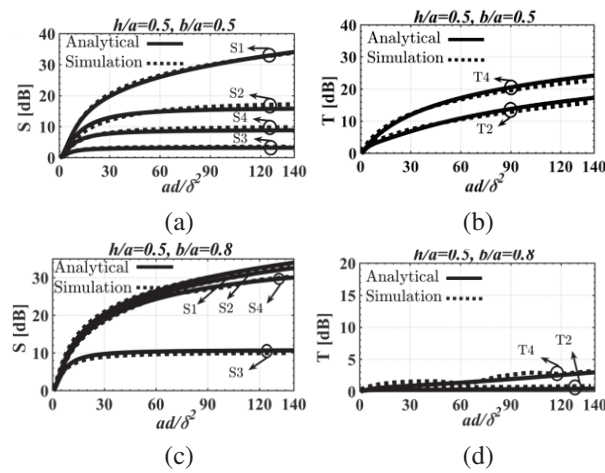


Fig. 2. Shielding factor “S” at (a) $b/a = 0.5$, (c) $b/a = 0.8$, and shielding efficiency “T” at (b) $b/a = 0.5$ and (d) $b/a = 0.8$ for different observations points as a function of ad/δ^2 .

together in Fig. 2 (a) for height $h = 0.5a$ and strip width $b = 0.5a$. The improvement of the shielding factor is noticed as the frequency increases, and it reaches a steady level at high-frequency values. This trend is noted at all observation points. The highest shielding level occurs at the center of the shield directly underneath the conducting strip at the conductor-air interface. The thickness of the shielding strip is insignificant compared to wavelength ($d \ll \lambda$). Therefore, the magnetic field’s strength at this position is approximately equal to the field’s strength at the center of the strip indicated by point P1. At low frequencies, the magnetic field can penetrate the shielding strip, where its thickness is smaller than the skin depth δ . Therefore, the shielding factor $S1$ shows low values. This phenomenon is observed from the 2D magnetic field vector maps shown in Fig. 3 (a) for $ad/\delta^2 = 5$. The magnetic field is transmitted through the conductive strips, since the induced eddy current is small. Increasing the excitation frequency, the shielding factor improves drastically (see Fig. 3 (b) for $ad/\delta^2 = 20$). This is due to the effect of surface-induced eddy current, which cancels out the magnetic field at the strip surface. Therefore, the magnetic field penetration in the vicinity of the strips decreases significantly. From (7), the real and imaginary parts of the normalized induced current density $K(x)/K_o$ on the strips at $t = 0$ can be evaluated using (16-a) and (16-b), which are plotted in Fig. 4 (a):

$$\text{Re} \left(\frac{K(x)}{K_o} \right) = 2 \sum_{n=1}^{\infty} n \cdot \text{Re}(C_n) \sin \left[n\pi \frac{x}{a} \right], \quad (16-a)$$

$$\text{Im} \left(\frac{K(x)}{K_o} \right) = 2 \sum_{n=1}^{\infty} n \cdot \text{Im}(C_n) \sin \left[n\pi \frac{x}{a} \right], \quad (16-b)$$

where the constant $K_o = I/a$. It can be seen from this figure that the current density has a comparable imaginary part with the real part. Therefore, the induced

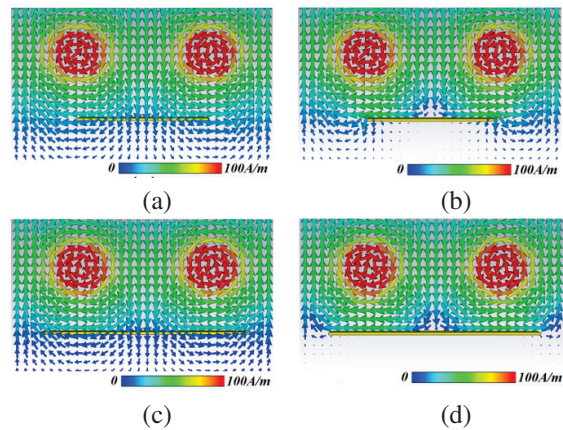


Fig. 3. 2D H-field maps for $b/a = 0.5$ at (a) $ad/\delta^2 = 5$, (b) $ad/\delta^2 = 20$, and for $b/a = 0.8$ at (c) $ad/\delta^2 = 5$ and (d) $ad/\delta^2 = 20$.

magnetic field due to eddy current is not enough to cancel out the source's field. When increasing the frequency, the shielding factor S improves. It is maintained above 30 dB at higher frequencies; i.e., $ad/\delta^2 > 90$.

Less shielding is observed of 15 dB at a distance h below the strip at point $P2$, which is indicated by the curve $S2$. As expected, poor shielding performance is observed in the slot and the region below the slot, as can be deduced from $S3$ and $S4$ curves at $P3$ and $P4$, respectively. The steady-state shielding factor at these two points is 3 and 9 dB, respectively. The 2D H-field map shown in Fig. 3 (b) illustrates the major reduction of the field's strength in the region below the strip. Whereas the field's strength is maintained high in the slot region, the field's cancelation is due to the increase in an eddy current field manifested by the increase in the current density's real part, as depicted in Fig. 4 (b). The shielding efficiency T is also compared, where the analytical solution using (15) and the simulated response are both plotted in Fig. 2 (b) for height $h = 0.5a$ and strip width $b = 0.5a$. Higher shielding efficiency is realized in the region directly below the conductive strips compared with the region below the slots, where 0 dB reference resembles the ideal value. This can be deduced from the curves labeled T2 and T4, which correspond to the fields observed at positions $P2$ and $P4$, respectively.

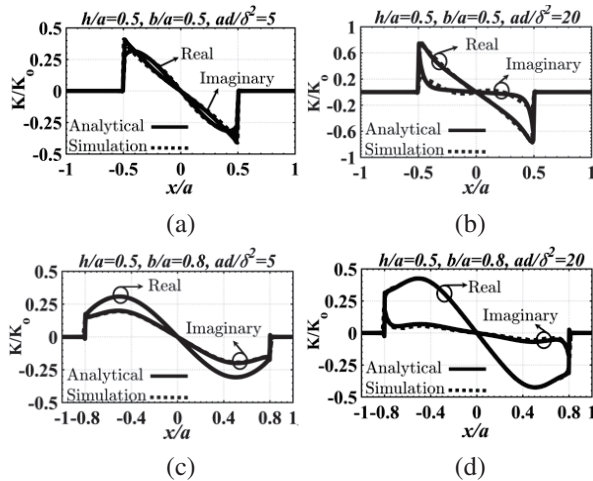


Fig. 4. Normalized surface current density " $K(x,t)/K_o$ " at $t = 0$ for strip width $b/a = 0.5$ at (a) $ad/\delta^2 = 5$, (b) $ad/\delta^2 = 20$ and $b/a = 0.8$ at (c) $ad/\delta^2 = 5$ and (d) $ad/\delta^2 = 20$ as a function of normalized position x/a .

As expected, shielding factor S improves drastically by increasing the strip's width b (i.e., reducing the slot's size), especially at positions $P2$ and $P4$. The shielding factor has enhanced to 26 dB and 28 dB respectively at $ad/\delta^2 = 90$ (see Fig. 2 (c), which shows the responses at all observation points for strip's width $b = 0.8a$

and fixed height $h = 0.5a$). Similarly, the shielding efficiency T also improves as illustrated in Fig. 2 (d). The response approaches the 0 dB level and gets closer to the shielding performance of the continuous sheet. The 2D map of magnetic field vector at low frequency is shown in Fig. 3 (c), while the field map at a higher frequency is depicted in Fig. 3 (d). The field's reduction in the region under the strips is obvious due to the induced field originating from an increasing eddy current that counterparts the original field. The current density is plotted in Figs. 4 (c) and (d) at low and high frequencies, respectively. Again, the real part of the surface current density is reduced significantly with respect to the real part at higher frequencies compared with the case of low frequencies. Further inspection is conducted by studying the effect of the strip's width b on the shielding factor and efficiency at fixed height $h = 0.5a$. Figure 5 shows the calculated and simulated responses of S and T at different observation positions for $ad/\delta^2 = 20$ and $ad/\delta^2 = 5$ respectively. The shielding factor at high frequency shown in Fig. 5 (a) reveals the behavior of increasing the normalized strip's width from 0 to 1.

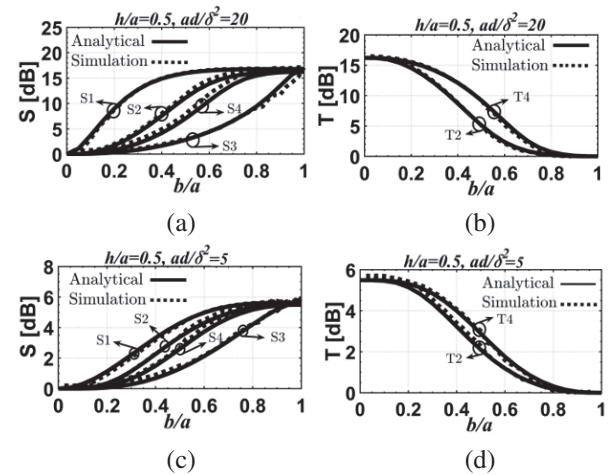


Fig. 5. Shielding factor " S " at (a) $ad/\delta^2 = 20$, (c) $ad/\delta^2 = 5$ and shielding efficiency " T " at (b) $ad/\delta^2 = 20$ and (d) $ad/\delta^2 = 5$ for different observation points as a function of normalized strip width b/a .

The zero-width corresponds to no shielding and the unity value corresponds to continuous plane shielding. The shielding factor approaches the maximum value of 15 dB when b/a exceeds 0.8. Therefore, the performance of the shielding system behaves similarly to the continuous plane, especially in the region below and away from the conductive strips as indicated in the curves $S1$, $S2$, and $S4$. Poor shielding is expected at the gap between the strips as indicated in the $S3$ curve. This is also seen from the T curves in Fig. 5 (b), where the

efficiency is approaching the 0 dB level for $b/a > 0.8$. The low-frequency performance is depicted in Figs. 5 (c) and (d) for S and T, respectively. The trend of increasing b is very similar to the case of high frequency but with a less efficient shielding level.

The excitation source of the parallel current lines has an insignificant impact on shielding performance, as revealed from studying the variation of the parameter h/a , which is swept in the range 0.1-2. The strip's width is kept fixed at $b/a= 0.5$. Figure 6 (a) shows the response of S at the four observations points for $ad/\delta^2= 20$. The shielding factor is almost constant with the height variation. Since the excitation source position with respect to the strips only determines the magnetic field's strength, the shielding factor is not affected by increasing the source's height. The change of the H-field with the absence of the strips is equal to the change of the field with the exitance of the shielding strips. Therefore, the ratio of the fields remains steady. This can be observed also even with different operating frequencies, as seen in Fig. 5 (c), where the value of ad/δ^2 is 5. The flat response of the shielding efficiency T is also attained in Figs. 6 (b) and (d) at high and low frequencies, respectively.

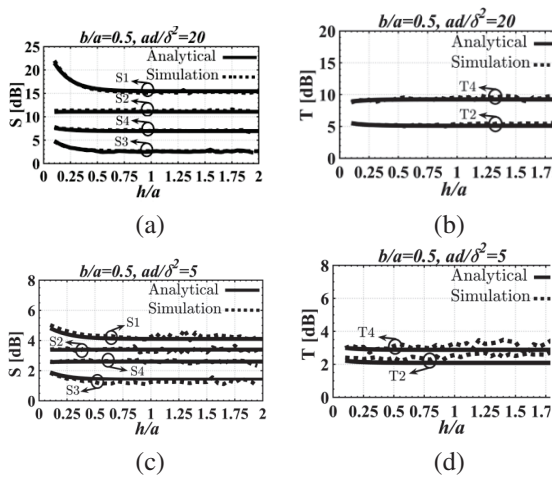


Fig. 6. Shielding factor “S” at (a) $ad/\delta^2=20$, (c) $ad/\delta^2= 5$ and shielding efficiency “T” at (b) $ad/\delta^2= 20$ and (d) $ad/\delta^2= 5$ for different observation points as a function of normalized height h/a .

IV. ELECTRIC FIELD SHIELDING

In general, EM waves propagate from one region to another, where their associated electric and magnetic fields are coupled in time and space as described by Maxwell's equations. This coupling between E and H is produced by the magnetic induction in Faraday's law ($\nabla \times E = -\partial B/\partial t$), and the displacement current density in Ampere's law ($\nabla \times H = J + \partial D/\partial t$). In the case

where EM waves possess slow time varying fields (low frequency) or small dimensions, quasistatic approximations can be considered such that fields become static [20]. The quasistatic laws are attained by neglecting either electric displacement current ($\partial D/\partial t \approx 0$) in magnetoquasistatic (MQS) approximation or the magnetic induction ($\partial B/\partial t \approx 0$) in electroquasistatic (EQS) approximation. In the case of current source, MQS approximations is applied, where time derivative of electric field vanishes. According to Faraday's law, the slowly varying magnetic field would induce a relatively weak electric field, which is approximately static in nature and almost independent of frequency. This is clearly observed from the 2D E-field maps that are illustrated in Fig. 7. The electric field at lower and higher frequencies are depicted in Figs. 7 (a) and (b), respectively for strip width $b = 0.5a$. Both electric field maps are nearly identical at the two frequencies, which reveal the accumulation of opposite signs of charge at the strip's sides. Very weak E-fields exist in the region below the shielding strips, which are mainly confined in the slit between the adjacent strips. A smaller gap (i.e., strip's width $b = 0.8a$) yields significant reduction in the E-fields, as seen in Figs. 7 (c) and (d) at both low and high frequencies. As a result, E-field shielding can be attained using this configuration.

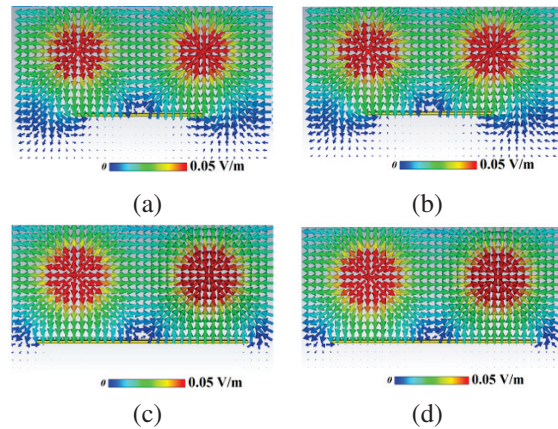


Fig. 7. 2D E-field maps for $b/a= 0.5$ at (a) $ad/\delta^2= 5$, (b) $ad/\delta^2= 20$, and for $b/a= 0.8$ at (c) $ad/\delta^2= 5$ and (d) $ad/\delta^2= 20$.

V. CONCLUSION

In this work, an analytical solution of the Laplace equation was presented using Fourier series expansion. This method was used to study the shielding behavior of a system comprising parallel conductive strips separated by small slits. The performance was characterized by evaluating the shielding factor in the region below the shield. Moreover, the performance of the presented shielding system is compared with a continuous

conductive sheet, which is manifested by the shielding efficiency. The effect of system parameters was studied in terms of shielding performance. The results have concluded that the proposed system behaves as a full plane when the normalized strip width is at least 0.8. This arrangement of conductive strips with slits adds an extra degree of flexibility compared to a continuous conductive plane shield, which could find some future application in magnetic shielding technology. The analytical results were also confirmed using computer simulation. The performance of the mathematical model was in very good agreement with the numerical simulation.

REFERENCES

- [1] S. B. Kim, J. Y. Soh, K. Y. Shin, J. H. Jeong, and S. H. Myung, "Magnetic shielding performance of thin metal sheets near power cables," *IEEE Transactions on Magnetics*, vol. 46, no. 2, pp. 682-685, 2010.
- [2] O. Bottauscio, M. Chiampi, and A. Manzin, "Numerical analysis of magnetic shielding efficiency of multilayered screens," *IEEE Transactions on Magnetics*, vol. 40, no. 2, pp. 726-729, Mar. 2004.
- [3] L. Sandrolini, A. Massarini, and U. Reggiani, "Transform method for calculating low-frequency shielding effectiveness of planar linear multilayered shields," *IEEE Transactions on Magnetics*, vol. 36, no. 6, pp. 3910-3919, Nov. 2000.
- [4] X. Di, "Magnetic shielding using electrical steel panels at extremely low frequencies" (doctoral dissertation, Cardiff University, UK), ProQuest Dissertations and Theses Global, 2008
- [5] H. H. Park, J. H. Kwon, S. I. Kwak, and S. Ahn, "Magnetic shielding analysis of a ferrite plate with a periodic metal strip," *IEEE Transactions on Magnetics*, vol. 51, no. 8, pp. 1-8, Aug. 2015.
- [6] T. Saito and T. Shinnoh, "Applications using open-type magnetic shielding method," *Journal of the Magnetics Society of Japan*, vol. 34, no. 3, pp. 422-427, 2010.
- [7] Y. Du and J. Burnett, "Magnetic shielding principles of linear cylindrical shield at power-frequency," *Proceedings of Symposium on Electromagnetic Compatibility*, pp. 488-493, 1996.
- [8] A. M. Dagamseh, Q. M. Al-Zoubi, Q. M. Qanawah, H. M. Jaradat, "Modelling of electromagnetic fields for shielding purposes," *Applied Computation Electromagnetics Society (ACES) Journal*, vol. 36, no. 8, pp. 1075-1082, Aug. 2021.
- [9] S. K. Burke and T. P. Theodoulidis, "Impedance of a horizontal coil in a borehole: a model for eddy-current borehole probes," *J. Phys. D: Appl. Phys.*, vol. 37, no. 3, pp. 485-494, Jan. 2004.
- [10] Y. Zhilichev, "Analytical solutions of eddy-current problems in a finite length cylinder," *Advanced Electromagnetics*, vol.7, no. 4, pp. 1-11, Aug. 2018.
- [11] X. Mao and Y. Lei, "Analytical solutions to eddy current field excited by a probe coil near a conductive pipe," *NDT & E International*, vol. 54, pp. 69-74, Mar. 2013.
- [12] V. L. Boaz, "Eddy current losses due to alternating current strips," *IEEE Transactions on Power Apparatus and Systems*, vol. 94, no. 1, pp. 1-9, Jan. 1975.
- [13] A. Efremov, S. Ventre, L. Udpa, and A. Tamburino, "Application of Dirichlet-to-Neumann map boundary condition for low-frequency electromagnetic problems," *IEEE Transactions on Magnetics*, vol. 56, no. 11, pp. 1-8, Nov. 2020.
- [14] Z. Zeng, L. Udpa, S. S. Udpa, and M. S. C. Chan, "Reduced magnetic vector potential formulation in the finite element analysis of eddy current nondestructive testing," *IEEE Transactions on Magnetics*, vol. 45, no. 3, pp. 964-967, Mar. 2009.
- [15] J. R. Nagel, "Finite-difference simulation of eddy currents in nonmagnetic sheets via electric vector potential," *IEEE Transactions on Magnetics*, vol. 55, no. 12, pp. 1-8, Dec. 2019.
- [16] J. R. Nagel, "Induced eddy currents in simple conductive geometries: Mathematical formalism describes the excitation of electrical eddy currents in a time-varying magnetic field," *IEEE Antennas and Propagation Magazine*, vol. 60, no. 1, pp. 81-88, Feb. 2018.
- [17] B. de Halleux, O. Lesage, C. Mertes, and A. Ptchelintsev, "Analytical solutions to the problem of eddy current probes consisting of long parallel conductors," in D. O. Thompson and D. E. Chimenti, eds, *Review of Progress in Quantitative Nondestructive Evaluation*, vol. 15, pp. 369-375, 1996.
- [18] S. Celozzi, R. Araneo, and G. Lovat, *Electromagnetic Shielding*, Wiley, Hoboken, NJ, USA, 2008.
- [19] CST Microwave Studio, ver. 2014, Computer Simulation Technology, Framingham, MA, 2014.
- [20] H. A. Haus and J. R. Melcher, *Electromagnetic Fields and Energy*, Prentice Hall, Englewood Cliffs, NJ, USA, 1989.



Hamzeh M. Jaradat received the Ph.D. degree in electrical and computer engineering from the University of Massachusetts Lowell (UML), USA. His current research includes electromagnetics modeling.



Qasem M. Qananwah received the Ph.D. degree in biomedical engineering from Karlsruhe Institute of Technology, Karlsruhe, Germany. His research interest focuses on instrumentation systems, design, and modeling.



Qasem M. Al-Zobi received his Ph.D. degree from the Technische Universitaet Berlin, Germany in 1990. His research interests include industrial electronics and external magnetic field screening.



Ahmad M. Dagamseh received his Ph.D. degree from the University of Twente in the Netherlands in 2011 in MEMS. His research interests include sensors, instrumentation systems, and modeling.